TAMPEREEN TEKNILLINEN YLIOPISTO
TAMPERE UNIVERSITY OF TECHNOLOGY

Toni Björninen

Advances in Antennas, Design Methods and Analysis Tools for Passive UHF RFID Tags

Julkaisu 1041 • Publication 1041

Tampere 2012

Tampereen teknillinen yliopisto. Julkaisu 1041
Tampere University of Technology. Publication 1041

Toni Björninen

Advances in Antennas, Design Methods and Analysis Tools for Passive UHF RFID Tags

Thesis for the degree of Doctor of Science in Technology to be presented with due permission for public examination and criticism in Tietotalo Building, Auditorium TB109, at Tampere University of Technology, on the 1st of June 2012, at 12 noon.

Tampereen teknillinen yliopisto - Tampere University of Technology
Tampere 2012

ISBN 978-952-15-2822-4 (printed)
ISBN 978-952-15-3068-5 (PDF)
ISSN 1459-2045

ABSTRACT

Radio-frequency identification (RFID) makes use radio waves to track objects equipped with electronic transponders, commonly known as tags. In passive RFID systems, the tags are remotely powered and they are composed of only two components: an antenna and an application specific integrated circuit (tag IC). At ultra high frequencies (UHF) this technology enables the rapid identification of a large quantity of tags at the distances of several meters, also in the absence of line-of-sight connection with the tag. While the passive UHF RFID is currently used e.g. in supply chain management and access control, in the future the passive tags capable of ultra-low-power data transmission are envisioned to provide platforms for wireless sensor nodes.

The maintenance-free and fully integrated on-tag electronics holds the promise to small, cheap, and inconspicuous tags, but achieving this in practice requires completely new design methods and analysis tools for antennas. Unlike conventional antennas, tag antennas need to be directly interfaced with an active load (tag IC) and seamlessly integrated with objects of various sizes and material contents. Here, especially the materials having adverse effect on the operation of conventional antennas present a major challenge, while at the same time the fundamental limitations on the performance of small antennas need to be considered.

This work addresses the above-mentioned challenges in the design of antennas for passive tags. Based on the new analysis tools and modern computational electromagnetics, a framework specifically tailored for the development of tag antennas is established. Combined with novel electronics materials and new fabrication methods this is shown to provide compelling means for tag antenna development. In particular, it is shown that tags with antennas produced using printable electronics, which has great potential to enable fabrication antennas directly on various unconventional platforms, can achieve competitive performance against the copper-based references. Furthermore, novel high-permittivity materials can be exploited to develop miniature antennas for metal mountable tags. Finally, three case studies, where antennas for tags in challenging applications are developed using the proposed design framework, are presented. The prototype tags achieve performance exceeding state of the art and exhibit excellent structural properties for the seamless integration with the considered objects.

AKNOWLEDGEMENTS

This research work has been conducted at Tampere University of Technology, Department of Electronics, Rauma Research Unit during the years 2008-2011. The research was funded by the Finnish Funding Agency for Technology and Innovation (TEKES), Academy of Finland, Centennial Foundation of Finnish Technology Industries, Tampere Doctoral Programme in Information Science and Engineering (TISE), Ulla Tuominen Foundation, HPY Research Foundation, and Nokia Foundation. The financial support is gratefully acknowledged.

I wish to express my gratitude to my advisor Adj. Prof. Leena Ukkonen and Head of Rauma Research Unit Prof. Lauri Sydänheimo for providing the superb environment for the doctoral studies at Rauma Research Unit and for the invaluable guidance and encouragement during my studies. My sincerest appreciation goes also to Prof. Atef Elsherbeni from the University of Mississippi for the enlightening and inspiring discussions.

I am indebted also to numerous co-workers and colleagues for their support and contributions. Special thanks are reserved for Sari Merilampi for the excellent collaboration in the research on printable antennas, Mikko Lauri for the great joint-research on wireless impedance measurement, and Abdul Ali Babar and Karina Espejo Delzo for sharing your ideas and expertise on antennas for metal mountable tags. For the inspiring lectures on antennas and modeling of electromagnetics, I wish to thank Tiiti Kellomäki, Jouko Heikkinen and Saku Suuriniemi. Finally, I would like to extend my gratitude to the whole RFID group for the invariably enthusiastic and pleasant work atmosphere.

During my doctoral studies, I also had the fantastic opportunity to work five months at Berkeley Wireless Research Center (BWRC) as a visiting scholar. This truly broadened my world view. Special thanks for the enjoyable visit are reserved for my studies advisor Prof. Jan Rabaey and the wonderful group of students at BWRC. Especially I wish to thank my close colleagues Michael Mark and Rikky Muller for guiding me into the wonders of neural interfaces and all the good times we shared.

Still, most of all, I am grateful to Zhang Jie and my family for the loving support, patience and encouragement.

Tampere, May 2012

Toni Björninen

LIST OF PUBLICATIONS

I. T. Björninen, S. Merilampi, L. Ukkonen, P. Ruuskanen, L. Sydänheimo, "Performance comparison of silver ink and copper conductors for microwave applications," *IET Microw. Antennas Propag.*, vol. 4, no. 9, pp. 1224-1231, Sept. 2010.

II. T. Björninen, S. Merilampi, L. Ukkonen, L. Sydänheimo, P. Ruuskanen, "The effect of fabrication method on passive UHF RFID tag performance," *Intl J. Antennas Propag.*, vol. 2009, Article ID 920947, 8 pages, May 2009.

III. T. Björninen, M. Lauri, L. Ukkonen, R. Ritala, A. Z. Elsherbeni, L. Sydänheimo, "Wireless measurement of RFID IC impedance," *IEEE Trans. Instrum. Meas.*, vol. 60, no. 9, pp. 3194-3206, Sept. 2011.

IV. T. Björninen, A. Z. Elsherbeni, L. Ukkonen, "Performance of single and double T-matched short dipole tag antennas for UHF RFID systems," *J. Appl. Computational Electromagn. Soc.*, vol. 26, no. 12, pp. 953-962, Dec. 2011.

V. T. Björninen, A. Z. Elsherbeni, L. Ukkonen, "Low-profile conformal UHF RFID tag antenna for integration with water bottles," *IEEE Antennas Wireless Propag. Lett.*, vol. 10, no. 1, pp. 1147-1150, Dec. 2011.

VI. T. Björninen, K. Espejo Delzo, L. Ukkonen, A. Z. Elsherbeni, L. Sydänheimo, "Long range metal mountable tag antenna for passive UHF RFID systems," *Proc. IEEE RFID-TA Int. Conf.*, pp. 194-198, 15-16 Sept. 2011, Sitges, Spain.

VII. T. Björninen, A. A. Babar. A. Z. Elsherbeni, L. Ukkonen, L. Sydänheimo, J. Kallioinen, "Compact metal mountable UHF RFID tag on a Barium Titanate based substrate," *Prog. Electromagn. Res. C*, vol. 26, pp. 43-57, 2012.

AUTHOR'S CONTRIBUTION

I. The author designed the studied transmission line components and conducted the simulations and measurements. The measured samples were fabricated by Sari Merilampi. The publication text was prepared together with the co-authors.

II. The author designed the studied antennas and conducted the antenna simulations. The studied antennas were fabricated by Sari Merilampi. The tag measurements were conducted by the author and Sari Merilampi. The publication text was prepared together with the co-authors.

III. The author has proposed the wireless measurement technique and is responsible for the presented deterministic analysis as well as antenna simulations. Mikko Lauri has implemented the Monte Carlo simulation. The experimental work has been conducted by the author and Mikko Lauri. The publication text was prepared together with the co-authors.

IV. The author has contributed the publication contents and is the main contributor of the publication text.

V. The author has contributed the publication contents and is the main contributor of the publication text.

VI. The proposed antenna is a joint-design by the author and Karina Espejo Delzo. The author has fabricated the prototype antenna, is responsible for the presented simulation and measurement results, and is the main contributor of the publication text.

VII. The author has designed the proposed antenna and is responsible for the presented simulation and measurement results. Abdul Ali Babar has fabricated the prototype antenna. The author is the main contributor of the publication text.

CONTENTS

1 INTRODUCTION

For the reader's convenience, road map to the contents of this work provided in Fig. 1. The text consists of five sections discussing the research results in publications [I-VII].

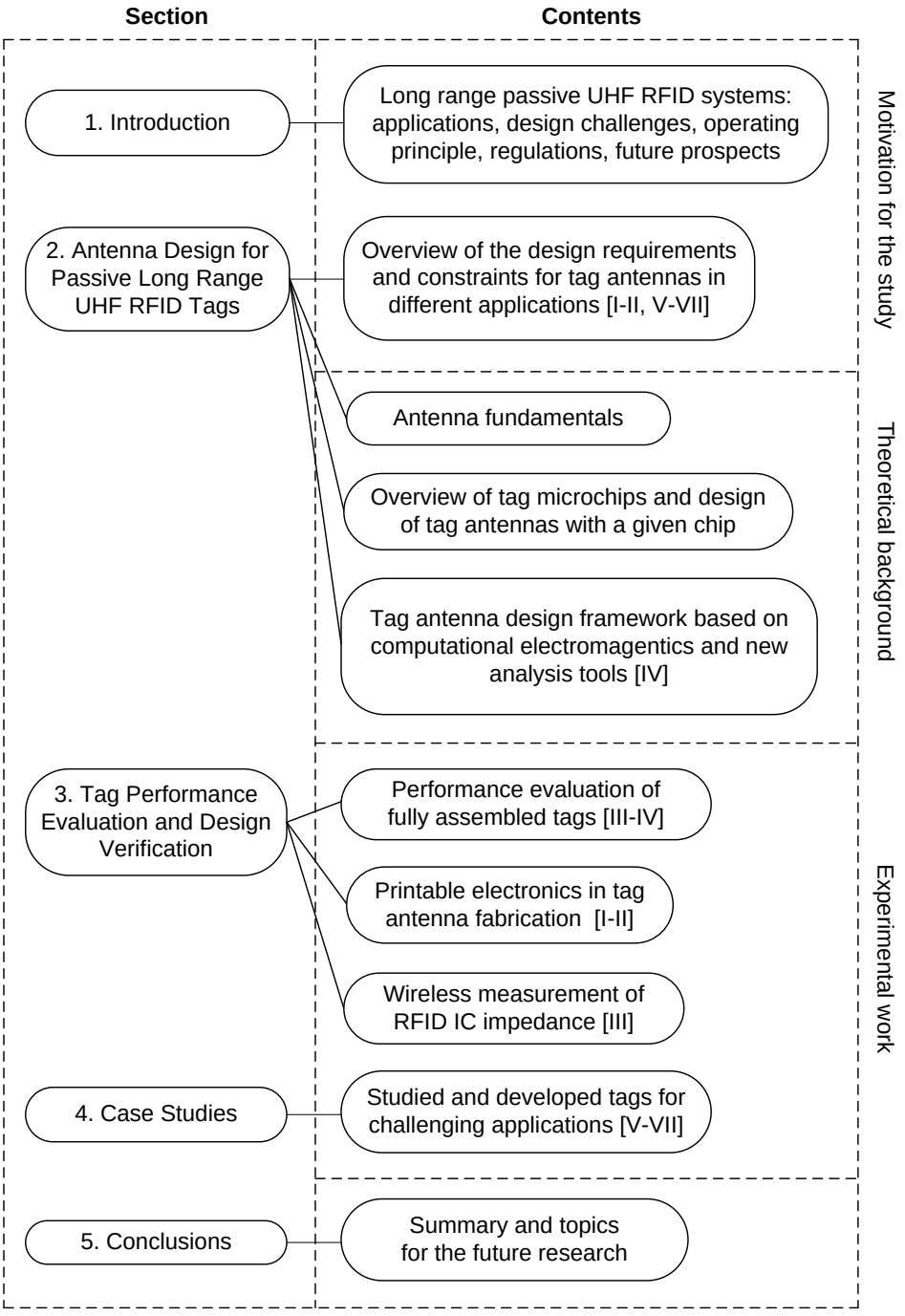

Figure 1. Structure and contents of the dissertation.

1.1 Radio-Frequency Identification Technology

Radio-frequency identification (RFID) technology provides the wireless automatic identification of assets tagged with electronic transponders, which are more commonly known as tags. In any RFID system, the identification is based on electromagnetic interaction between the tags and dedicated readers, conveyed by antennas on both sides. According to the mechanism of the interaction, RFID systems can be divided into near field and far field systems, where electromagnetic coupling and wave propagation are used for communication, respectively. Due to link physics, the operation range in near field systems is short, whereas substantially longer ranges are achieved in far field systems. For this reason, the far field RFID systems are also referred to as long range RFID systems.

The use of propagating electromagnetic waves at ultra high frequencies (UHF) for powering and communicating with the tags enables the rapid identification of a large amount of objects through various media from the distances of several meters with maintenance-free tags. These are the main advantages that initially sparked the interest on passive long range RFID. Currently, it has applications in access control, supply chain management, and in item-level asset tracking, while new applications are emerging. Recently, e.g. the use of tag antennas as sensing elements has gained much attention and efforts on the use of RFID for indoor positioning has been made. Miniature, ultra-low-power and maintenance-free tags are also envisioned to provide platforms for wireless sensor nodes in the next generation internet – the internet of things. Tracking of people with wearable tags, as well as bio-medical applications from body movement monitoring tags to miniature cortical implants utilizing wireless communication techniques similar to RFID are also being investigated. [1]-[10]

Despite the relatively straightforward basic functionality of RFID, the holistic design and optimization of RFID tags is demanding because of the stringent tag size, cost and integration requirements. While these requirements bring the tag antenna design in the frontiers of the current antenna engineering and electronics manufacturing, the conventional antenna design techniques also need to be adapted to interface the antenna and the ultra-low-power RFID microchip optimally. Here the impedance matching of the antenna to a complex and non-linear load is a major issue. Finally, thorough knowledge on the electromagnetic theory of scattering is required for understanding the non-conventional wireless communication scheme based on the modulation of antenna scattering.

Currently a major challenge that need be overcome in order to make RFID ubiquitous and enable its large-scale implementation for item-level identification is the development of new antennas for inconspicuous tags with an optimal cost-performance ratio for the considered application. While the printable electronics holds the promise to the seamless integration of antennas with various unconventional platforms, given that sufficient performance is achieved with the printed antennas, the reliable identification of objects containing or consisting of materials, which have adverse effects on the functioning of traditional antennas, is a key challenge. [11]-[14]

The focus of this work is on exploring new design methods and analysis tools for the development of novel antennas for passive long range UHF RFID tags in challenging applications and thereby to improve the overall system performance from the tag side. To meet this challenge, the following steps have been taken: a new method for the characterization of RFID microchips is developed [III], analytical methods combined with modern computational electromagnetics simulations are used to create a design framework for holistic tag performance optimization [IV], the use of novel electronics materials and new fabrication methods [I-II] to create tag antennas for challenging applications [V-VII] is investigated.

1.2 Operation Principle of Passive Long Range UHF RFID System

The core components in any RFID system are tags, readers, and a system for data management. The focus of this work is on passive long range UHF RFID systems, where the tags are remotely powered by the reader and the tag-to-reader data link is based modulated antenna scattering. This communication scheme provides superior power efficiency on the tag side [9] and it is therefore fit for passive RFID. Figure 2 shows the core components and functional blocks of the system and illustrates its operation principle.

The passive tags consist of only two separate entities: the tag antenna and the RFID tag microchip (tag IC). The antenna is responsible for capturing energy from the continuous wave emitted by the reader. Once there is sufficient voltage across at the antenna terminals to activate the semiconductor devices in the on-chip rectifier circuitry, it starts to supply power to the rest of the circuit. With the tag IC fully activated, the on-chip radio will listen in for commands from the reader, but the tag never responds to the reader spontaneously. The reader may also request new data to be recorded in the on-chip memory, but in the most common operation cycle, the reader polls for the identification code of the tag stored in the on-chip memory. The tag responds by modulating the requested information in the scattering from the tag antenna using the impedance switching scheme and. Once the response is detected by the reader, it will be distributed over to the data management system.

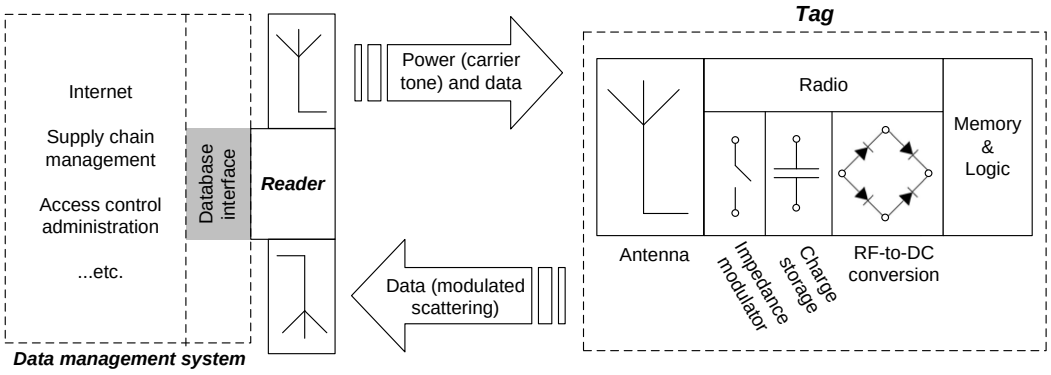

Figure 2. Key components and operation principle of a passive RFID system

1.3 Overview of Regulations for UHF RFID

Due to the abundance of the wireless systems, the radio spectrum has been divided into sub-bands with regulated emission limits to keep the inter-system interference at a tolerable level. In practice, the emission limit is imposed as the equivalent isotropically radiated power (EIRP), defined as the product of the power accepted by the transmit antenna and its maximum gain over all the spatial angles within the regulated frequency band. This enforces the same maximum radiated power density for any transmit antenna. [1]

The readable range of a passive RFID tag is strongly dependent on the transmitted power. Thus, in the research and development of passive tags, it is important to always refer the achieved read range to a specific EIRP value. This enables the judicious performance comparison between designs reported by the researchers worldwide. Table 1 lists the current EIRP regulations for UHF RFID systems in different regions. Communication protocols for RFID are also being standardized and currently there is ISO 18000-6 standard [15] defining the air interface protocol for RFID. In addition, the most widely used tags follow EPCglobal UHF Class 1 Generation 2 standard [16], which defines the physical and logical requirements of the tags.

Table 1. EIRP regulations for UHF RFID systems in different regions [16].

Region	Frequency band [MHz]	EIRP [W]
Europe	865.6 – 867.6	3.28
China	840.5 – 844.5 920.5 – 924.5	3.28
Republic of Korea	917 – 920.8 917 – 923.5	4 0.2
Japan	952 – 956.4	4
Canada United States	902 – 928	4
Australia	920 – 926 918 – 926	4 1

2 ANTENNA DESIGN FOR PASSIVE LONG RANGE UHF RFID TAGS

Antennas are passive structures designed to convey the electromagnetic interactions efficiently. Heinrich Hertz was the first one to study these structures and in his famous experiment in 1888, he demonstrated for the first time the transmission of energy between two antennas. This was also the first experimental verification of the existence of electromagnetic waves and it sparked the broad interest on the field of antennas and wireless communication that still carries on. [17]

In the development of any wireless systems, an important task is to adapt the general knowledge on antennas for the needs of the specific application. A well-known example is the mobile phones, where a multi-resonant antenna needs to be fitted in the sub-wavelength-sized device. Antennas for RFID tags have similar size constraints. In addition, tag antennas need to be seamlessly integrated with objects of various size, shape and material contents, and impedance matched with a strongly frequency- and power-dependent tag IC. These are some of the unique features of antenna design for RFID tags, which are covered in this section along with the antenna fundamentals. In particular, achieving the proper impedance matching between the tag antenna and IC under design uncertainties is a pronounced aspect in tag design. For the judicious evaluation of the impact of these uncertainties, the author has developed a new numerically efficient framework for the evaluation of the sensitivity of the impedance matching towards impedance variations [IV]. This topic is discussed in Section 2.4.

2.1 Design Requirements and Constraints

The maximum distance at which a tag can be detected by the reader is an important practical tag performance indicator, which can be understood by both antenna and application engineers. For this reason, the achievable tag read range with a given tag IC is often considered as the starting point for tag antenna design. The possible choices for the antenna structure are then narrowed down based the application specific requirements, such as the acceptable tag size and cost, and the properties of the platform where the tag is to be mounted on.

Especially in the item-level identification of a large asset base, low manufacturing costs per tag is a key-requirement. In the development of tag antennas, this puts the focus on small and simple structures. Although clever antenna size-reduction and impedance matching techniques are available [18]-[23];[IV], there are fundamental physical limitations for the achievable performance of an antenna with a given size [24]-[25]. In RFID context, this makes it a challenge to create aggressively miniaturized antennas capable of powering the tag IC from usable distances for identification. Thus, an appropriate antenna

size-performance ratio, given the application specific constraints is often a major design choice.

Commonly, the tags also need to be inconspicuous. This means that the antennas need to be low-profile and conform to the objects' surface. A compelling means to achieve this is the use of printable electronics processes, such as screen printing, gravure printing, pad printing or inkjet printing in antenna fabrication. With these methods, conductive ink can be deposited on a wide variety of platforms. This provides new means of integrating antennas e.g. with paper-based and textile platforms, as well as other platforms, which do not tolerate the chemicals used in the conventional etching process. In this way, potential cost-savings can be achieved since a separate antenna platform is no longer required. [11][26]-[33];[I-II]

However, another issue arises when tag is mounted on objects with various unknown material contents: the interaction between the electromagnetic fields of the tag antenna and the matter may significantly affect the antenna performance. While tag antennas with reduced antenna-matter interaction (platform-tolerant or general purpose tags) have been reported [34]-[37], it is difficult to achieve this without increasing the structural complexity of the antennas. On the other hand, for application specific tags, a co-design approach where the particular antenna platform is treated as a part of the antenna, has been found useful [38][39];[V-VII].

For metal mountable tags, the antenna-matter interaction is a particularly pronounced issue. This is because of the strong image current induced on the nearby metal surface. With the antenna distance much less than a quarter wavelength from the metal, the elec-

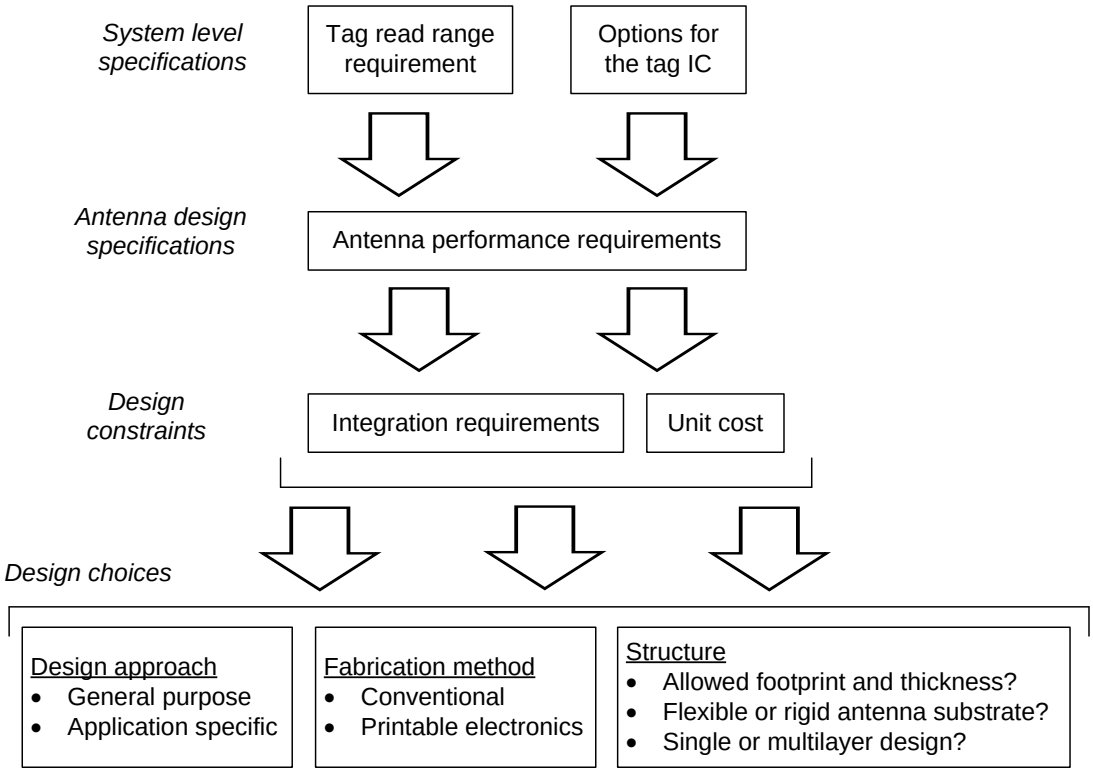

Figure 3. Tag antenna design flow.

tromagnetic fields radiated by the image current and the antenna sum up with approximately 180^o phase difference and cancel each other largely [40]-[42]. Consequently, the antenna radiation efficiency is low and the tag read range limited. Further, the proximity of the metal surface (even a small one compared with the antenna) can greatly affect the antenna impedance and radiation pattern compared with the properties of an isolated antenna [40][43]. Antennas with a ground plane, such as microstrip patch antennas and planar inverted-F antennas, do not suffer from this phenomenon as severely [44][45], but compared with dipole and slot antennas they have more complex structure and higher unit cost. In applications, such as the identification of cargo containers, industrial machinery, or similar high-value assets, tags with higher unit cost are an acceptable option [46]-[49];[VI], but e.g. in item-level identification of small metallic objects, more cost effective solutions are required. Some small and low-profile antennas for metal mountable tags have been proposed [50]-[53], while achieving this with a simple antenna structure based on only a single conductor layer remains a topic of ongoing research [54][55];[VII].

The design flow diagram presented in Fig. 3 summarises the tag antenna design process and clarifies the various design choices that need to be made in accordance with the requirements and constraints of the intended application.

2.2 Antenna Impedance and Radiation

Impedance

In a typical design scenario, the tag antenna is designed as an isolated device. In this case it can be analyzed as a single-port passive device and the antenna impedance (Z_a) is defined simply as the ratio of the driving point voltage and current phasors. Nevertheless, the physical nature of the antenna impedance is quite different from lumped passive circuit elements. This is because antennas radiate energy and the power leaving the antenna may contribute a major part in the antenna resistance (R_a). This part of the resistance is the antenna radiation resistance (R_{rad}) and the remainder is the loss resistance (R_{loss}) related to the power loss: $P_{loss}=P_{acc}-P_{rad}$, where P_{rad} is the total power that could be extracted from the radiated fields of the antenna and P_{acc} is the power accepted by the antenna from the generator. The antenna reactance (X_a) is related to the reactive power of the antenna near fields, similar to the reactance of an inductor or a capacitor.

As will become clear from the analysis presented below, the formation of electromagnetic radiation from the antenna current is a strongly frequency-dependent process and thus the antenna impedance exhibits similar characteristics. The electromagnetic energy dissipated in the materials surrounding the antenna conductor may have dispersive characteristics as well. Finally, the energy dissipation in the antenna conductor starts to increase rapidly in conductors with thickness below the so-called skin depth (δ). For materials with high electrical conductivity (σ), this thickness is approximately [42][56][57]

$$\delta \approx \frac{1}{\sqrt{\pi f \mu_0 \sigma}}. \qquad (1)$$

Thus, the accurate prediction of the antenna impedance is extremely difficult by purely analytic means. Fortunately, towards the end of the 20th century, many efficient computational electromagnetics (CEM) tools have become widely available for microwave engineers, and at present, a regular work station computer can be used for simulation of microwave devices, including antennas.

While CEM tools facilitate the design greatly, as a starting point for a practical tag antenna design, knowledge on the frequency response of certain canonical antenna types is indispensible. Based on this knowledge the canonical antennas can be further modified with the help of CEM tools for achieving the desired antenna impedance and radiation properties. The tag antennas [V-VII] studied and developed in this work (details discussed in Section 4) are modifications of three different well-known antenna types: dipole, slot, and microstrip patch antenna illustrated in Fig. 4. Common to these structures is that for efficient radiation, the parameter L should be in the order of $\lambda/2$ with λ being the wavelength of operation although smaller size can be achieved with special design techniques [18]-[23]. For the microstrip patch antenna, the thickness h of dielectric material layer is typically in the range from 0.003λ to 0.05λ [58].

The fundamental antenna resonance frequency (f_0) is the lowest frequency where the antenna reactance crosses zero. In practice, the larger the antenna structure, the lower the achievable f_0, but the realized f_0 depends on the specific design choices. Especially the arrangement of the antenna conductor plays a major role here. Due to their stringent size

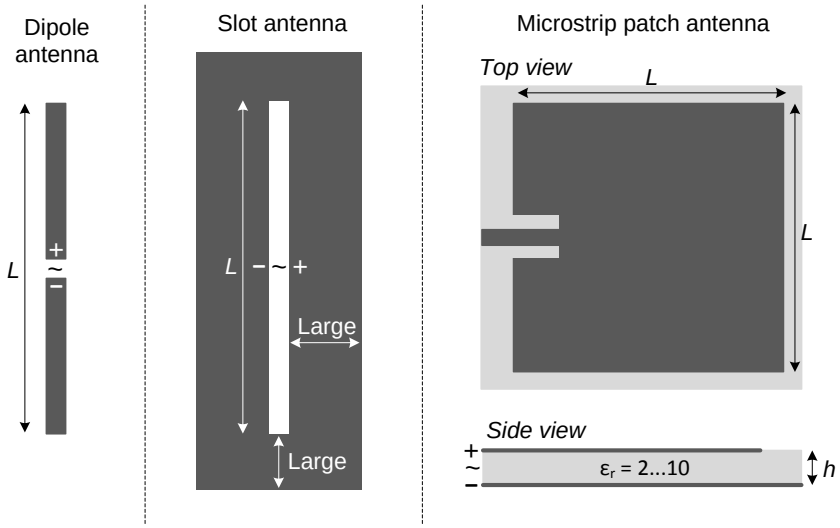

Figure 4. Examples of canonical antenna structures.
The antenna terminals are indicated with + and −.

Table 2. Input impedance of the canonical antenna structures shown in Fig. 4.

Frequency	$f < f_0$	$f \to 0$
Dipole [40][41]	$\mathrm{Im}(Z_a) < 0$, $\mathrm{Re}(Z_a)$ = small	$\mathrm{Im}(Z_a) \to -\infty$
Slot [40][41]	$\mathrm{Im}(Z_a) > 0$, $\mathrm{Re}(Z_a)$ = small	$\mathrm{Im}(Z_a) \to 0$
Microstrip patch (typical) [58]	$\mathrm{Im}(Z_a) > 0$, $\mathrm{Re}(Z_a)$ = small	

requirements, tag antennas typically have the maximum dimension less than or around quarter wave length and they operate below or near f_0 of the given structure. For the canonical antenna types illustrated in Fig. 4, the properties of the antenna impedance below f_0 are predetermined by the electromagnetic theory (see Table 2). As discussed in Section 2.4, this has important implications for the implementation of tag antenna impedance matching.

Antenna Radiation

Perhaps the most important information on any antenna is its radiation characteristics. This includes the spatial distribution of the power density in the radiated fields, efficiency of the transformation of energy from the antenna input to the radiated fields, and the polarization properties of the radiated fields. In Section 2.4 it will also be seen that antenna radiation and scattering properties are closely related.

As known from the fundamentals of electromagnetic theory, time-varying current creates electromagnetic fields which transport energy away from the source. This is the process of electromagnetic radiation. A major goal in antenna design is to adapt the antenna structure, so that the impressed current flow in it produces radiation with the desired spatial distribution. In order to achieve this in a well-founded manner, one must be able to compute the power density of the radiated field at an arbitrary point.

Let (θ,φ,ρ) be a spherical coordinate system where the radiated fields are observed and (x,y,x) the corresponding Cartesian coordinates. Suppose the time-harmonic antenna current density **J** is represented in another Cartesian coordinate system (u,v,w) and further that the antenna is enclosed in a volume V which contains the origin of (x,y,z). Then the antenna *power pattern* $F(\theta,\varphi)$, which is the normalized power density of the radiated field on a spherical shell around the antenna, is approximated with [40]

$$F(\theta,\phi)=\frac{|Q(\theta,\phi)|^2}{\max|Q(\theta,\phi)|^2}, \tag{2a}$$

where
$$Q(\theta,\phi)=\int_V \mathbf{J}(u,v,w)e^{j\frac{2\pi f}{c}\upsilon(\theta,\phi)}\,du\,dv\,dw, \tag{2b}$$

$$\upsilon(\theta,\phi)=u\sin\theta\cos\phi+v\sin\theta\sin\phi+w\cos\theta, \tag{2c}$$

and
$$(x-u)^2+(y-v)^2+(z-w)^2 >> \max_{(u,v,w)\in V}\left(u^2+v^2+w^2\right). \tag{2d}$$

Here the condition (2d) limits the analysis to such remote points where the radiated electromagnetic fields can be treated locally as plane waves to a good approximation. The directional weighting function $Q(\theta,\varphi)$ contains the relevant physical information of the source current and the electric and magnetic field components

$$\mathbf{E}(\theta,\phi,\rho)=\mathrm{E}(\theta,\phi,\rho)\mathbf{1}_{ant} \quad \text{and} \quad \mathbf{H}(\theta,\phi,\rho)=\frac{1}{\eta}\mathrm{E}(\theta,\phi,\rho)\mathbf{1}_{\rho}\times\mathbf{1}_{ant}, \tag{3}$$

respectively, can be derived directly from it [40]. Here the unit vectors $\mathbf{1}_{\mathrm{ant}}$ and $\mathbf{1}_{\rho}$ are the antenna polarization vector and the radial unit vector, respectively, and the constant η is the wave impedance in vacuum: $\eta \approx 377\ \Omega$.

Since $F(\theta,\varphi)$ is a normalized quantity with the maximum of unity, a more suitable quantity for comparison of different antennas is the *antenna directivity* $D(\theta,\varphi)$, defined as the ratio of the radiated power density in direction (θ,φ) to the radiated power density averaged over all spatial directions. Following this definition, the well-known expression [40][41]

$$D(\theta,\phi)=\frac{F(\theta,\phi)}{\frac{1}{4\pi}\int_0^{2\pi}\int_0^{\pi}F(\theta,\phi)\sin\theta\,d\theta\,d\phi} \tag{4}$$

is obtained.

To evaluate the practical performance of antennas, neither the power pattern nor directivity alone is sufficient, since they provide no information on the amount of energy absorbed into the antenna structure and its surroundings. This information is carried by the antenna *radiation efficiency* (e_{rad}). It is defined as the ratio of the power accepted by the antenna (P_{acc}) to the total power radiated by the antenna (P_{rad}) [40]:

$$e_{rad}=\frac{P_{rad}}{P_{acc}}; \quad P_{rad}=\frac{\eta}{8\lambda^2}\int_0^{2\pi}\int_0^{\pi}|Q(\theta,\phi)|^2\sin\theta\,d\theta\,d\phi. \tag{5}$$

Directivity multiplied with the efficiency yields the *antenna gain* $G(\theta,\varphi)$. It tells how large a power density the radiated field contains, compared with a hypothetical isotropic antenna with radiation properties: e_{rad}=1 and $D(\theta,\varphi)$=1 accepting the same power. Finally, it needs to be stressed here that e_{rad} defined in equation (5) excludes the effects of possible impedance mismatch between the generator and the antenna input. This loss source is discussed in Section 2.4.

To summarize the physical meaning of the antenna parameters introduced above, suppose that an antenna accepts power P_{acc} from the generator. At an observation point (θ,φ,ρ), the time-average power density of the radiated field is then approximated with

$$S(\theta,\phi,\rho)=\frac{P_{acc}G(\theta,\phi)}{4\pi\rho^2}. \tag{6}$$

Importantly, according to the reciprocity theorem [40], the same set of parameters determine the power available from an antenna ($P_{av.ant}$), when an incident wave with time-average power density S_{inc} impinges on it from direction (θ,φ) [40]:

$$P_{av.ant}=A_{eff}(\theta,\phi)\chi_{pol}S_{inc}, \tag{7a}$$

$$\text{with} \qquad A_{eff}(\theta,\phi) = \frac{\lambda^2}{4\pi} G(\theta,\phi), \tag{7b}$$

$$\text{and} \qquad \chi_{pol} = \left| \mathbf{1}_{ant} \cdot \mathbf{1}_{inc} \right|^2. \tag{7c}$$

Here A_{eff} is the antenna effective aperture and χ_{pol} is the polarization loss factor determined by the mutual alignment of the receiving antenna and the incident wave polarization vectors $\mathbf{1}_{\text{ant}}$ and $\mathbf{1}_{\text{inc}}$, respectively. Thus, radiation efficiency, directivity, and gain are the fundamental performance parameters also for receiving antennas. Tag antennas in particular are receiving antennas harvesting power for the tag IC.

2.3 Overview of Tag Microchips

The use of modulated antenna scattering as a means for wireless communication was introduced as early as 1948 [59]. Possibly the first completely passive RFID tag was reported in 1975 [60], but it was not until the successful fabrication of Schottky diodes on a regular CMOS integrated circuit in 1990's that the passive RFID tags started to assume their present shape without off-chip components. With this development, the design of fully integrated RFID ICs got into full speed. The functional blocks common to essentially all present day RFID ICs for passive tags are illustrated in Fig. 5. [61]

Since the ICs on passive tags are remotely powered, an important chip performance parameter is the wake-up power (P_{ic0}). Different operations on chip require different power, but most commonly the IC wake-up power is defined with respect to the query command, to which the tag responds with its identification code stored in the on-chip memory. One of the earliest fully integrated RFID ICs fabricated in CMOS process with additional Schottky diodes was reported in 2003 [62]. The circuit achieved the wake-up power of −17.7 dBm (16.7 μW). Presently, the wake-up powers of commercially available tag ICs fabricated in standard CMOS process are reaching −18 dBm (15.8 μW) [63]-[65], while alternative processes [66] and novel rectifier designs in CMOS [67] may provide further improvement in the future.

Based on the analysis in Section 2.2, for passive tags the power available for the IC is

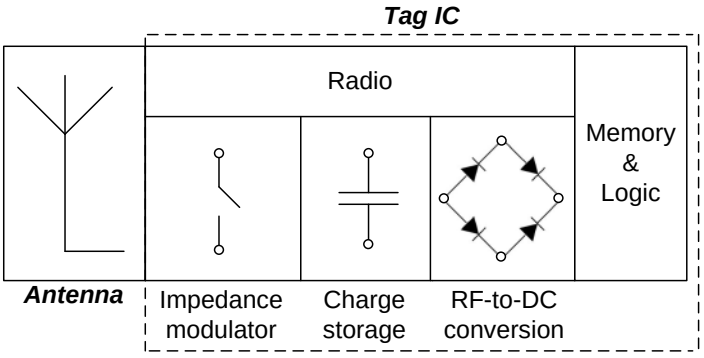

Figure 5. Functional blocks of an RFID IC.

determined by the tag antenna gain. However, even if the antenna impedance has been designed to be exactly the conjugate of the chip impedance for lossless power transfer between the two, additional power loss will occur in the on-chip RF-to-DC conversion. Indeed, at low input voltages below 0.3 V, the RF-to-DC conversion loss grows rapidly. This feature is shared by virtually all low-power rectifier architectures [9] and as seen from above review of the development of the IC wake-up powers during the recent years, it is a challenge to get around this limitation.

The non-linearity of the rectifier also accentuates the fundamental difference between impedance matching of conventional antennas and tag antennas: in contrast to passive loads, the IC impedance varies with the input power. Therefore, it is crucial to match the antenna impedance to the complex conjugate of the tag IC impedance at the wake-up power the chip: $Z_{ic}(P_{ic0})$. While the IC impedance at higher power levels may differ from $Z_{ic}(P_{ic0})$, the margin for the mismatch loss increases as well, so that the additional impedance mismatch at high power levels is not expected to limit the operation [68][69].

Unfortunately, the measurement of $Z_{ic}(P_{ic0})$ is challenging and with conventional approaches advanced equipment are required [70][71]. This is because the measurement instrument needs to communicate with the IC, while ramping down the transmitted power to determine the appropriate output power corresponding to the IC wake-up power. To provide an alternative approach, a wireless technique to measure $Z_{ic}(P_{ic0})$ including the IC mounting parasitic has been developed by the author [III]. The details of the measurement technique are discussed in Section 3.3.

2.4 Impedance Matching and Antenna Scattering

Impedance matching

While the tag antenna gain determines the power available from the antenna when an incident field impinges on it (equation (7)), the antenna-IC power transfer efficiency (τ) is determined by impedances of the two components. For the purpose of tag antenna design, the power transfer efficiency can be analyzed based on a series equivalent circuit shown in Fig. 6, where the antenna and IC are joined with a transmission line of a negligible electrical length. In this setting, the antenna acts as a generator with internal impedance $Z_a=R_a+jX_a$ and source voltage amplitude V_a (antenna open circuit voltage) and delivers power to the IC represented as impedance $Z_{ic}=R_{ic}+jX_{ic}$. From here on it is assumed that this is the impedance at the wake-up power of the circuit. Letting V_{ic} and I_{ic} be the tag IC voltage and current amplitudes, respectively, the standard complex phasor calculus provides the time-average power delivered to the IC:

$$P_{ic}=\frac{1}{2}\mathrm{Re}\left(\tilde{V}_{ic}\tilde{I}_{ic}^{*}\right)=\frac{1}{2}\mathrm{Re}\left(\frac{Z_{ic}}{Z_a+Z_{ic}}\tilde{V}_a\left(\frac{\tilde{V}_a}{Z_a+Z_{ic}}\right)^{*}\right)=\frac{1}{2}\frac{R_{ic}}{\left|Z_a+Z_{ic}\right|^2}\left|V_a\right|^2. \qquad (8)$$

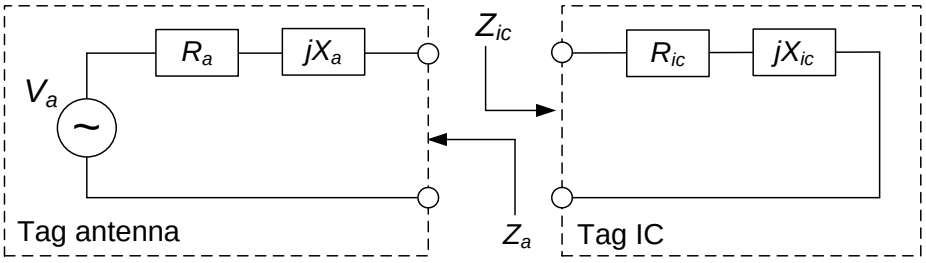

Figure 6. Thévenin equivalent circuit of a receiving tag antenna loaded with a tag IC.

Here ($\tilde{}$) identifies the complex voltage and current phasors and $(\cdot)^*$ denotes the complex conjugate. According to the well-known conjugate matching principle, the power delivered to the IC is maximized with $Z_a = Z_{ic}^*$. Therefore, from equation (8), one obtains the antenna-IC power transfer efficiency:

$$\tau = \frac{P_{ic}}{P_{ic}\big|_{Z_a = Z_{ic}^*}} = \frac{4R_a R_{ic}}{\left|Z_a + Z_{ic}\right|^2}. \tag{9}$$

Alternatively, the power reflection coefficient

$$\Gamma = \frac{P_{ic}\big|_{Z_a = Z_{ic}^*} - P_{ic}}{P_{ic}\big|_{Z_a = Z_{ic}^*}} = 1 - \tau = \left|\frac{Z_{ic} - Z_a^*}{Z_{ic} + Z_a}\right|^2 \tag{10}$$

can be used to as measure of how much of the available power from the antenna is not delivered to the IC due to impedance mismatch.

To gain further insight on how the deviation of Z_a from the optimum value $Z_a = Z_{ic}^*$ affects the power transfer, it is useful to notice that for a given IC impedance and τ, equation (9) defines a circle in the antenna impedance plane with the center point and radius given by

$$P(\tau) = \left(R_{ic}\frac{2-\tau}{\tau}, -X_{ic}\right) \quad \text{and} \quad r(\tau) = 2R_{ic}\frac{\sqrt{1-\tau}}{\tau}, \tag{11}$$

respectively. As an example, constant τ circles for Z_{ic}=15−j150 Ω are visualized in Fig. 7.

In conventional radio communication systems, antennas are typically designed to deliver power efficiently to a constant 50 Ω load. In contrast, tag ICs have a strongly frequency dependent and inherently capacitive input impedance, which also varies with input power. Moreover, due to the cost and integration requirements, lumped components are rarely used in impedance matching of tag antennas, but instead self-matching approaches based on adapting the antenna structure appropriately, are preferred [21]. While the amount of power absorbed by the matching network is an important aspect in the design of radio-frequency devices, for the self-matched antennas this information is carried by the antenna radiation efficiency.

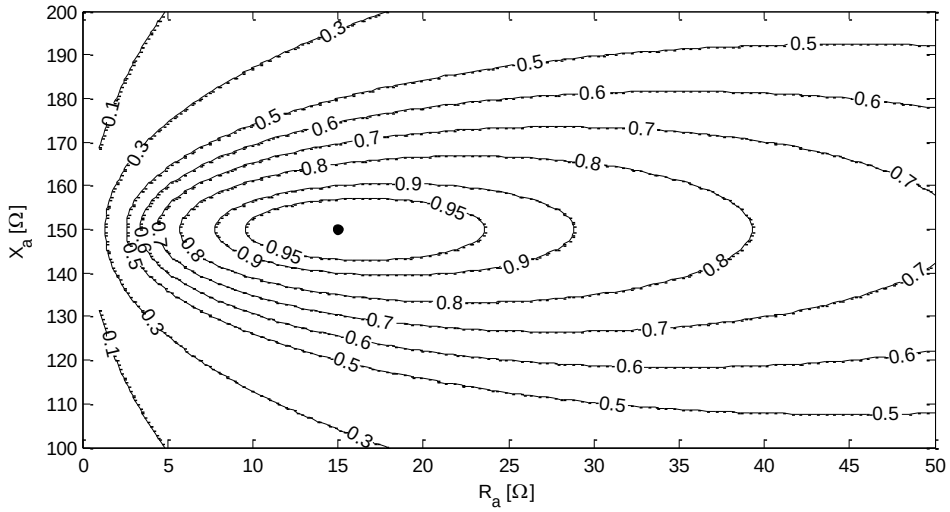

Figure 7. Contours of τ with tag IC impedance $Z_{ic}=15-j150\ \Omega$. The solid dot marks the point $Z_a=Z_{ic}^*$, where τ attains its unique maximum: $\tau = 1$.

Self-matching techniques for small dipole tag antennas, include single and double-T matching, proximity-coupled loop-feed, and meander line arrangements. They transform the inherently capacitive antenna impedance (Table 2) to inductive for conjugate matching with the tag IC [21][38][72];[IV-V]. On the other hand, the impedance of small slot antennas is inherently inductive (Table 2) so that it suffices to control the length of the radiating current path around the slot [21][73];[VII]. In a typical configuration, also the microstrip patch has inductive feed point reactance below the fundamental resonance (Table 2) and e.g. proximity-coupled loop-feed and inductive shorting strips [54][55];[VI] have been used in impedance matching of patch type tag antennas.

As seen in Section 2.2, the antenna impedance and radiation properties have a complicated relation to the antenna current distribution and for an arbitrary antenna shape closed form expressions for the current distribution do not exist. Therefore, modern CEM tools are indispensible in tag antenna design, but even so, the lack of accurate knowledge of the IC impedance may keep the designer from getting the full benefit out of the design techniques and simulation tools. Moreover, even with known IC impedance, the IC mounting parasitics vary with the chip attachment method [74]-[76], so that overall it may be extremely difficult to achieve the perfect complex conjugate impedance matching. While the new IC impedance method presented in [III] accounts also for the IC mounting parasitic, for the purposes of tag design validation, it is still extremely important to understand how the possible impedance variations affect the antenna-IC power transfer efficiency. To enable the judicious evaluation of the impact of these uncertainties, the author has developed a new numerically efficient framework to relate given impedance tolerances to the corresponding tolerance in antenna-IC power transfer efficiency [IV].

Suppose that the antenna and chip impedances lie in the neighbourhood of their nominal values $Z_{a0}=R_{a0}+jX_{a0}$ and $Z_{ic0}=R_{ic0}+jX_{ic0}$, respectively. Typically, percentage tolerances are considered and in this case these neighbourhoods are rectangles in the IC and antenna impedance planes. Let $0<p,r<\infty$, $0<q,s<\infty$, and $0<\varepsilon<\min(p,r)$ and consider sets defined as

$$D_\varepsilon = \left\{ (x, y) \in R^2 : x \geq \varepsilon,\ y \in R \right\}, \tag{12a}$$

$$\Lambda_{pq} = \left\{ (x, y) \in R^2 : \left| R_{ic0} - x \right| \leq pR_{ic0}, \left| X_{ic0} - y \right| \leq q \left| X_{ic0} \right| \right\} \bigcap D_\varepsilon, \tag{12b}$$

$$\Lambda_{rs} = \left\{ (x, y) \in R^2 : \left| R_{a0} - x \right| \leq rR_{a0},\ \left| X_{a0} - y \right| \leq s \left| X_{a0} \right| \right\} \bigcap D_\varepsilon. \tag{12c}$$

Under these definitions, Λ_{pq} and Λ_{rs} are rectangles centered at the nominal IC and antenna impedances, respectively, and restricted in the half-plane containing the positive resistances. The size of these rectangles is determined by the parameter pairs (p,q) and (r,s) with r and p defining the percentage tolerance in R_a and R_{ic}, respectively, and the parameters s and q defining percentage tolerance in X_a and X_{ic}, respectively. As shown in [IV], the minimum antenna-IC power transfer efficiency (τ) within the 4-dimensional uncertainty rectangle $\Lambda_{pq} \times \Lambda_{rs}$ is given by

$$\tau_{min} = \min_{+/-} \frac{4\chi_\varepsilon(1 \pm r)\chi_\varepsilon(1 \pm p)R_{a0}R_{ic0}}{\left(\chi_\varepsilon(1 \pm r)R_{a0} + \chi_\varepsilon(1 \pm p)R_{ic0}\right)^2 + \left(X_{a0} \pm s\left|X_{a0}\right| + X_{ic0} \pm q\left|X_{ic0}\right|\right)^2}, \tag{13a}$$

$$\text{with} \quad \chi_\varepsilon(x) = \begin{cases} \varepsilon, & x \leq 0 \\ x, & x > 0, \end{cases} \tag{13b}$$

where the minimum is considered for all the possible +/− sign combinations. Compared with a direct numerical search through a 4-dimensional search grid, equation (13) greatly expedites the evaluation of the worst-case antenna-IC power transfer efficiency under given impedance uncertainties. Moreover, as shown in [IV], the maximum value of τ within the 4-dimensional uncertainty rectangle $\Lambda_{pq} \times \Lambda_{rs}$, is attained in the Cartesian product of the boundaries of the sets Λ_{pq} and Λ_{rs}. This observation provides significant speed-up for the numerical search of the best-case antenna-IC power efficiency under given impedance uncertainties.

Overall, the analysis presented in [IV] provides a numerically efficient framework for evaluation of the sensitivity of the tag antenna impedance matching towards impedance variations. Combined with the measured IC impedance [III] and the related limits of uncertainty, this provides a new approach for judicious tag design validation [IV-VI]. Practical demonstrations of this are provided in Sections 4.1 and 4.2.

Antenna Scattering

Scattering of electromagnetic wave from an object means the transformation of the incident wave into the scattered waves propagating in all directions from the object, including the non-specular directions [77]. The scattered waves originate from surface currents induced on the object and the structure of the field is therefore largely determined by the shape of the scattering object. For antennas, the load impedance affects the scattering as well [41]. This feature is being exploited in RFID systems, where the tag IC impedance (antenna load impedance) is switched between two values in order to modulate the scat-

tering from the tag, while it is illuminated by a continuous wave emitted by the reader.

As a measure of the scattering from an object, the *radar cross-section (RCS)* is commonly used [42]. It measures the visibility of the object to radar in terms of the power density (S_{scat}) it scatters to a remote observation point (θ,φ,ρ) relative to the power density (S_{inc}) of the field that impinges on it from direction ($\theta_{inc},\varphi_{inc}$):

$$RCS = 4\pi\rho^2 \cdot \frac{S_{scat}(\theta,\phi)}{S_{inc}(\theta_{inc},\phi_{inc})}. \tag{14}$$

However, the physical nature of the antenna scattering is perhaps better understood with the help of the antenna-scatterer theorem [78]. It states that the total scattered electric field from an antenna can be interpreted as the superposition of two components:

$$\mathbf{E}_{scat} = \mathbf{E}_{scat1} + \mathbf{E}_{scat2} \tag{15a}$$

$$\mathbf{E}_{scat1} = \mathbf{E}_0, \quad \mathbf{E}_{scat2} = -\frac{sZ_a I_{sc}}{2R_a I_{rerad}}\mathbf{E}_{rerad}, \quad s = \frac{Z_{ic} - Z_a^*}{Z_{ic} + Z_a}, \tag{15b}$$

where $\mathbf{E}_0$ the scattered electric field due to induced surface currents on a conjugate matched antenna, I_{sc} is the short circuit current at the antenna terminals, and I_{rerad} is the current flowing in the equivalent circuit shown in Fig. 6 with the corresponding radiated electric field $\mathbf{E}_{rerad}$. The parameter s is the power wave reflection coefficient [79], which is related to the antenna-IC power transfer efficiency through: $\tau = 1-|s|^2$.

There is a fundamental difference between the scattered fields $\mathbf{E}_{\text{scat1}}$ (structural mode scattering) and $\mathbf{E}_{\text{scat2}}$ (antenna mode scattering). Referring to the equivalent circuit representation of an RFID tag shown in Fig. 6, the antenna mode scattering originates from the power reflected at the antenna-IC interface due to impedance mismatch. The corresponding component of the scattered field is interpreted as the re-radiation of this power [80]. Therefore, the spatial distribution of the antenna mode scattering is predicted by using I_{rerad} as a source current in (2) and then (15b) to obtain the corresponding scattered electric field. As seen from (15b), $\mathbf{E}_{\text{scat2}}$ is a function of the antenna load and it vanishes under conjugate matching.

In contrast, the structural mode scattering originates from the surface currents, which are confined in isolated regions in the antenna and not flowing through the antenna terminals. Thus, the simple analysis based on the equivalent circuit shown in Fig. 6 cannot be used to predict its spatial distribution. Moreover, as $\mathbf{E}_{\text{scat1}}$ is unaffected by the antenna load (and its modulation), the structural mode scattering is fundamentally less interesting for the analysis of RFID systems. On the other hand, this implies that the spatial distribution of the information carrying modulated scattering from the tag is completely determined by the tag antenna radiation pattern.

Pursuing the idea of the antenna mode scattering as the re-radiation of the power not delivered to the antenna load, from equation (7) the total re-radiated power is

$$P_{rerad} = |s|^2 P_{av.ant} = \chi_{pol} \frac{\lambda^2}{4\pi} |s|^2 G(\theta_{inc}, \phi_{inc}) S_{inc}, \tag{16}$$

where S_{inc} is the power density of the field that impinges on the antenna from direction $(\theta_{inc},\varphi_{inc})$. Consequently, using this in equation (6), the power density of the antenna mode scattered field at an observation point (θ,φ,ρ) is

$$S_{scat} = \frac{G(\theta,\phi) P_{rerad.}}{4\pi\rho^2} = \chi_{pol} \frac{\lambda^2}{(4\pi\rho)^2} |s|^2 G(\theta,\phi) G(\theta_{inc}, \phi_{inc}) S_{inc}. \tag{17}$$

Thus, applying the definition of RCS given in equation (14) to the antenna mode scattering alone, yields the magnitude of the antenna mode RCS:

$$RCS_{ant} = \chi_{pol} \frac{\lambda^2}{4\pi} |s|^2 G(\theta,\phi) G(\theta_{inc}, \phi_{inc}). \tag{18}$$

Taking into account the modulation of the tag IC impedance in time-domain, which directly affects I_{rerad} in equation (15b), leads to the definition of modulated or differential RCS [81][82]:

$$RCS_{mod} = \chi_{pol} \frac{\lambda^2}{4\pi} G(\theta,\phi) G(\theta_{inc}, \phi_{inc}) L_{mod}, \tag{19a}$$

$$\text{with} \quad L_{mod} = \alpha |s_1 - s_2|^2. \tag{19b}$$

Here L_{mod} is the *tag modulation loss factor* determined by power wave reflection coefficients s_1 and s_2 corresponding to the two tag IC impedance states and parameter α is related to the details of the modulation scheme, such as the duty-cycle.

An important implication of the physical principles of the antenna scattering for the analysis of RFID systems is that the visibility of the tag to the reader is determined by the tag antenna directivity, radiation efficiency and the realization of the on-chip impedance modulator. In particular, the structural scattering is related to the surface currents on the antenna structure which are not flowing through the antenna terminals. Thus, this scattering component it is unaffected by the impedance modulation. Moreover, from equation (19b), it can be concluded that a trade-off between the antenna-IC power transfer efficiency (τ) and the modulation loss factor (L_{mod}) exists. However, the read range of passive tags is presently limited by the power delivery to the tag IC and thus it suffices to concentrate on maximizing τ. In systems with battery assisted tags, or in the future passive RFID systems with more sensitive ICs, the co-optimization of τ and L_{mod} may be needed to maximize the overall system performance.

2.5 Fundamental Tag Performance Parameters

The operation of passive long range UHF RFID tags is predominantly limited by the reader-to-tag power delivery, also in real application environments, because the power required for activating the tag IC is orders of magnitude larger than the weakest tag signal

that can be detected at the reader [1][3][82][83]. Thus, the *realized tag antenna gain* ($G_{r,tag}$), which tells how much more power the tag antenna delivers to the tag IC compared with a perfectly matched isotropic tag antenna, is a fundamental tag performance parameter. In terms of the antenna performance parameters introduced earlier, it has the expression

$$G_{r,tag} = \tau G_{tag} = \tau e_{rad,tag} D_{tag}. \tag{20}$$

The *tag antenna power pattern* $F_{tag}(\theta,\phi)$ is obtained by normalizing $G_{r,tag}$ with its maximum over the spatial angles of interest.

While the realized tag antenna gain is perhaps the most profound tag performance parameter, it may not be as intuitive as the *tag read range* (d_{tag}), the longest distance at which the reader is able to communicate with the tag with an EIRP-compliant generator power. This performance parameter is readily understood by both antenna and application engineers, but as the read range is obviously site-dependent due to scattering, it needs to be defined in reference conditions for judicious comparison. While the Friis' simple transmission formula [84] describing the power transmission between two isolated antennas in free space may not provide adequate prediction for the reader-to-tag power delivery in real application environments [82][83], it can be employed in tag antenna design verification in a controlled environment.

In free space, the maximum EIRP-compliant power density (S_{EIRP}) of the radiated electromagnetic wave at distance d from the radiation source is [84]

$$S_{EIRP} = \frac{EIRP}{4\pi d^2}, \tag{21}$$

where *EIRP* denotes the regulated EIRP value. When a tag is exposed to this field, the power delivered to the tag IC (P_{ic}) is obtained by applying equations (7) and (20). As a result,

$$P_{ic} = \tau \chi_{pol} \frac{\lambda^2 G_{tag}}{4\pi} S_{EIRP} = \chi_{pol} G_{r,tag} \left(\frac{\lambda}{4\pi d} \right)^2 EIRP. \tag{22}$$

As discussed earlier, normally the tag read range is limited by the power delivery to the tag IC. Therefore, the critical distance d from equation (22) at which the power delivered to the tag IC equals the wake-up power of the chip: $P_{ic} = P_{ic0}$, is defined as the tag read range. From equation (22) this is easily solved to be:

$$d_{tag} = \frac{\lambda}{4\pi} \sqrt{\frac{\chi_{pol} G_{r,tag} EIRP}{P_{ic0}}}. \tag{23}$$

For practical considerations, it is important to observe that since the maximum EIRP-compliant transmitted power is defined with respect to the maximum gain of the reader antenna, the tag read range given by equation (23) can only be achieved with the maximum gain of the reader antenna pointed at the tag.

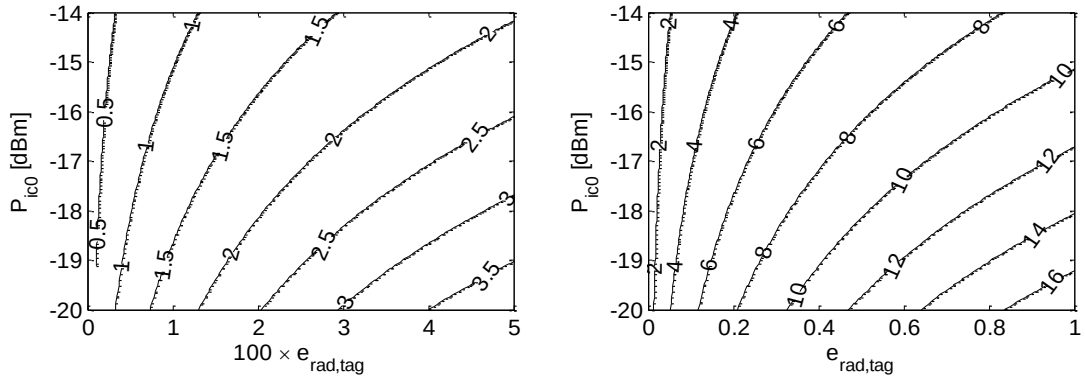

Figure 8. Tag read range (d_{tag}) obtained from equation (23) with χ_{pol} =1, τ=0.75, D_{tag}=2.15 dBi, and *EIRP*=3.28 W. Values on the contours are shown in meters.

Omnidirectional antennas, such as dipoles and slots, with relatively low directivities (in the order of 1-to-2 dBi) provide broad spatial coverage for reliable energy scavenging and are therefore popular tag antennas. However the radiation efficiencies of these antennas may vary much depending on the antenna size and surrounding materials. With this in mind, it is of practical interest to study the tag read range given in equation (23) as a function of the radiation efficiency and tag IC wake-up power. This provides valuable insight on the achievable read ranges of passive tags with different antenna-IC combinations.

Importantly, it can be seen from Fig. 8 that as the tag IC wake-up powers are currently reaching −18 dBm, high radiation efficiency is no longer an absolute requirement for achieving the read range of several meters, provided that the antenna-IC power transfer efficiency is reasonable. As one of the issues with small antennas and antennas in the proximity of dissipative materials is the difficulty of achieving high radiation efficiency, trading off a portion of the radiation efficiency for size-reduction purposes can be a feasible approach in design of antennas for aggressively miniaturized tags. This is one of the techniques exploited in the design of the water bottle tag [V] and the small metal mountable tag [VII] developed by the author. These antennas are discussed in more detail in Section 4.

3 TAG PERFORMANCE EVALUATION AND DESIGN VERIFICATION

The measurement of small antennas is problematic [85]-[88]. Therefore, the performance evaluation of fully assembled tags based on reader-to-tag communication threshold is a compelling approach. It avoids the separate antenna and IC measurements, correctly and automatically accounts for IC mounting parasitics, and requires few advanced equipment. Importantly, the fundamental tag performance parameters discussed in Section 2.5 can be obtained from the measurements on fully assembled tags based on the reader-to-tag communication threshold [III-VI]. The tag performance evaluation and design verification based on this method is discussed in Section 3.1.

Printable electronics provides exciting new possibilities for the fabrication of tag antennas directly on various platforms [11][26]-[33]. Presently, patterns created with conductive polymer thick film inks can achieve high conductivities and therefore it is of practical interest to compare the performance of tags with printed antennas against the references based on conventional conductors. This also reveals how the conventional design approaches work with the printed conductors. The related research results [I-II] are reviewed in Section 3.2.

Accurate knowledge on tag IC impedance is the key to successful tag antenna design. The IC impedance, however, differs significantly from the conventional 50 Ω system impedance of microwave measurement instruments and varies with the incident power. This makes the IC impedance measurement problematic [70]-[71]. The wireless impedance measurement technique [III] discussed in Section 3.3 provides the IC impedance corresponding to the wake-up power of the chip, including the IC mounting parasitics which may significantly contribute to the impedance seen from the antenna terminals toward the chip [74]-[76]. This is extremely valuable information for tag antenna designers.

3.1 Communication Threshold in Tag Measurements

Connecting the measurement instrument on small antennas may affect the measurement outcome. The mechanisms behind this are unwanted radiation from the measurement cables and electromagnetic interaction between the antenna and the connector, cables and possibly other measurement instruments near the antenna. Balun can be used reduce the radiation from the measurement cables [85], but the presence of connectors and cables in the antenna proximity may still be an issue. Therefore, contactless measurement techniques are being developed for the characterization of small antennas [86]-[88].

Evidently, the antenna performance is a decisive factor for the performance of fully assembled tags, but actually the fundamental tag performance parameters; realized gain, read range, and normalized power pattern, discussed in Section 2.5 can be obtained with-

out separate antenna measurements. A straightforward method of measuring the tag read range is to take the tag farther away from the reader antenna until its response stops. This method may be the best one to define the tag performance in a specific application environment, but otherwise the multipath propagation renders the results incomparable between different sites and with the simulations on an isolated tag. Conducting the measurement in an anechoic chamber avoids this problem, but since the chambers are often limited in size, an alternative method based on the ramping of the transmitted power is advantageous. It also provides improved repeatability and accuracy, since neither the tag nor the reader antenna needs to be moved during the measurement. The idea in the power ramping measurement is to decrease the power transmitted by the reader, while all the time communicating with the tag. The smallest power at which a response from the tag is detected is defined as the *threshold power* (P_{th}) of the tag.

Since the wake-up power is a key parameter to characterize tag ICs, an estimate for it is normally provided by the manufacturer. With this information, the realized tag antenna gain ($G_{r,tag}$) defined in equation (20) is estimated by solving it from the free space link equation, which describes the power delivery from the transmit port of the reader to the IC:

$$P_{ic0} = \chi_{pol} G_{r,tag} G_{r,tx} \left(\frac{\lambda}{4\pi d} \right)^2 P_{th} \Rightarrow G_{r,tag} = \frac{P_{ic0}}{\chi_{pol} G_{r,tx} \left(\frac{\lambda}{4\pi d} \right)^2 P_{th}}. \tag{24}$$

Here the distance d is the separation between the reader antenna and the tag, and $G_{r,tx}$ is the realized reader antenna gain including the cable loss between the transmit port of the reader and the input of the reader antenna. Moreover, the comparison of equations (23) and (24), yields the measured tag read range:

$$d_{tag} = d \sqrt{\frac{EIRP}{G_{r,tx} P_{th}}}, \tag{25}$$

Finally, the measured tag antenna power pattern $F_{tag}(\theta,\varphi)$ is obtained by measuring $G_{r,tag}$ over the spatial orientations of interest and normalizing the result:

$$F_{tag}(\theta,\phi) = \frac{G_{r,tag}(\theta,\phi)}{\max\limits_{\theta,\phi} G_{r,tag}} = \frac{\min\limits_{\theta,\phi} P_{th}}{P_{th}(\theta,\phi)}. \tag{26}$$

Thus, the fundamental tag performance parameters discussed in Section 2.5 are obtained from the threshold power of the tag measured in an anechoic environment.

The threshold power can be measured with an RFID reader with adjustable output power. RFID measurement instruments, such as the Voyantic Tagformance RFID measurement system [89] which has been used to characterize the prototype tags presented in [V-VII], may also provide the measurement channel characterization for the compensation of the possible multipath effects. In the Voyantic system, the link loss factor (L_{iso}) from the transmit port of the reader to the input port of a hypothetic isotropic antenna

placed at the tag's location can be measured. With this information, equation (24) is re-written as

$$P_{ic0} = \chi_{pol} G_{r,tag} L_{iso} P_{th} \Rightarrow G_{r,tag} = \frac{P_{ic0}}{\chi_{pol} L_{iso} P_{th}}, \tag{27}$$

which provides an alternative expression for the measured $G_{r,tag}$ with multipath compensation. Moreover, supposing that P_{th} in (24) was subjected to multipath effects, by multiplying it with a correction factor

$$K = \frac{L_{iso}}{G_{r,tx}\left(\frac{\lambda}{4\pi d}\right)^2}, \tag{28}$$

one obtains exactly the link equation (27) incorporating the multipath compensation. Thus, K maps the measured threshold power to its theoretical free space value. Employing this correction in equation (25), the tag read range with multipath compensation becomes

$$d_{tag} = \frac{\lambda}{4\pi}\sqrt{\frac{EIRP}{L_{iso} P_{th}}}. \tag{29}$$

The measured tag antenna power pattern $F_{tag}(\theta,\varphi)$ remains unaffected by the multipath compensation since K is independent of the tag orientation.

3.2 Printable Electronics in Tag Fabrication

Chemical etching is the most commonly used technique to fabricate conductive patterns. In the etching process, a thin conductive foil – typically copper or aluminum – on a substrate material is etched into the desired form by using corroding chemicals. This greatly limits the choices between the substrate material and in many cases an additional etching-tolerant antenna substrate is needed in the tag. Commonly used tag antenna substrates include Polyethelene Terephthalate (PET) film and various rigid circuit board materials.

Unlike etching, printable electronics processes [11][26]-[32] are additive: the conductive material is deposited only in the regions where it is needed. Conductive inks consist of a polymer matrix, conductive fillers, and solvents. Silver particles are commonly used as the conductive filler material, but progress has also been made in the development of copper based inks to lower the material costs [33]. Second step in the fabrication process is curing. At this stage, the solvent is evaporated and contact between conductive particles in the polymer matrix is formed. The outcome is a solid electrically conductive pattern. The thickness and resolution of the pattern depend on the fabrication technique used. The techniques studied in this work are outlined below and the properties of the conductive inks used are listed in Table 3.

Screen printing

In screen printing technique, mesh of threads forming a grid of pixels is stretched on a frame. The pixels outside the print pattern are blocked with a stencil. The conductive ink is pressed through the open pixels onto the substrate with a squeegee. The thickness of the ink layer is determined by the screen, stencil, ink composition, curing conditions, as well as the speed, pressure, and angle applied on the squeegee. For instance, screen printed microwave transmission lines with thicknesses of 40 µm [28] and 14.6 µm [I] have been investigated, while thinner structures could be produced as well [26]. The maximum printing resolutions is around 50 lines per centimeter. [26];[I-II]

Gravure printing

Gravure printing is a technique, which uses an engraved cylinder to transfer the print pattern to the substrate. The engraved pattern on the cylinder consists of the gravure cells which hold the ink while transferring the pattern. The thickness of the print pattern depends on the engravings on the gravure cylinder, but process parameters such as printing speed and pressure also have an effect. For instance 4-to-7 µm conductor layer was produced with 20-to-60 µm gravure cells [27] and 3.8 µm conductor with 60 µm cells [II]. With gravure process, the conductive patterns can only be created on a flexible substrate because of the pressure needed in the pattern transfer. The resolution that can be achieved depends on how the cylinder engraving has been done. With electromechanical engraving 100 lines per centimeter can be achieved while laser engraving increases the resolution. Compared with screen printing, gravure printing has high throughput and it is used for long runs. Gravure printing is a fast technique and enables mass production. [26];[II]

Screen Printed Microstrip Line Components at Microwave Frequencies

To evaluate the aptitude of the two printing techniques for tag fabrication, two sets of experiments were carried out. At first, screen printed microstrip transmission lines and coupled-line couplers were designed, fabricated and tested [I]. This experiment provides insight on the performance of the screen printed devices in a conventional microwave system, where their performance is compared in terms of insertion loss. The experiments

Table 3. Characteristics of the conductive inks in the experimentation.

Printing technique	Manufacturer's description	Recommended curing conditions	Viscosity	Conductivity
Screen printing	One component silver ink consisting of polyester resin and silver particles.	20 minutes in 120 °C	20...30 Pa·s	1.25 MS/m
Gravure printing	Silver pigment in a thermoplastic resin for flexographic or rotogravure printing techniques.	20 minutes in 120 °C	4 Pa·s	4 MS/m

were also readily conducted over a broader frequency band than it is possible to operate fully assembled tags.

For the experiment, 50 Ω microstrip transmission lines with the length of 10 cm were designed on a copper clad FR-board with the thickness of 1.5 mm. The conductor thicknesses of the screen printed and copper etched lines are 35 µm and 20 µm, respectively. For the screen printed lines also the ground plane was printed for fair comparison. The lines were compared in terms of insertion loss per centimetre which was both simulated and measured. The simulations were conducted with ANSYS high frequency structure simulator (HFSS), which is a full-wave electromagnetic field solver based on finite element method [90]. The conductivities of 58 MS/m and 1.25 MS/m (nominal value reported by the manufacturer) were used for the copper etched and screen printed lines, respectively, in the simulations. The FR-4 board was simulated using the dielectric constant of 4.5 and two different models for the dielectric loss: constant loss tangent of 0.02 and a frequency dependent loss tangent increasing directly proportional to the frequency from 0.016 at 100 MHz to 0.024 at 5 GHz. Both models are based on results reported in [91]. The measurements were conducted with the HP8722D vector network analyzer.

Considering the transmission line as a two-port network, the maximum obtainable transducer power gain ($G_{T,max}$), which is achieved under simultaneous conjugate match conditions [92], describes the minimum obtainable loss in the line. This is the electromagnetic isolation between the two ports [93]. In the absence of coupling to other devices and discontinuities in the line, any power loss is due to the dielectric and conductor losses only. Therefore, it is natural to interpret $G_{T,max}$ as the insertion loss of the line (IL). Moreover, since in the studied case both, the screen printed and copper etched lines, are fabricated on the same substrate material, any difference in the insertion loss of the lines can be contributed to the different conductivities of the conductor material.

In both, simulations and measurements, it was observed that the characteristic impedance of the studied transmission lines is very close to 50 Ω system impedance of the measurement instrument with $|S_{11}|^2$ and $|S_{22}|^2$ below −20 dB (less than 1% power loss at in/output ports due to impedance mismatch). This means that the input and output voltage reflection coefficients Γ_{in} and Γ_{out}, respectively, satisfy $\Gamma_{in} \approx S_{11}$ and $\Gamma_{out} \approx S_{22}$. As shown in [92], under these approximations,

$$G_{T,max} = IL \approx \frac{|S_{21}|^2}{(1-|S_{11}|^2)(1-|S_{22}|^2)}. \tag{30}$$

Toward larger values of $G_{T,max}$, the accuracy of the approximation in equation (30) is sensitive to errors [93], i.e. the accuracy in of the initial approximation: $\Gamma_{in} \approx S_{11}$ and $\Gamma_{out} \approx S_{22}$, becomes crucial. However, due to the good impedance matching of the studied lines, the simplified insertion loss analysis based on equation (30) was considered sufficient. Finally, the approximate insertion loss per centimetre was calculated by an appropriate scaling of the value given by equation (30) with the physical line length.

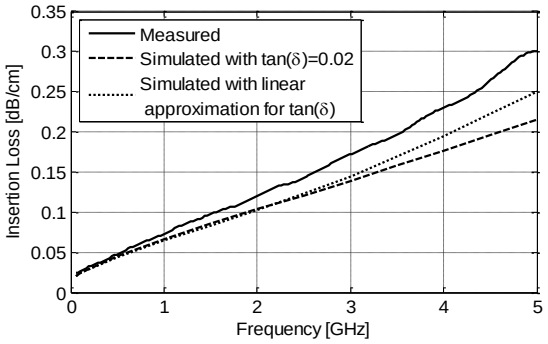

Fig. 9a. Measured and simulated insertion loss of the screen printed line.

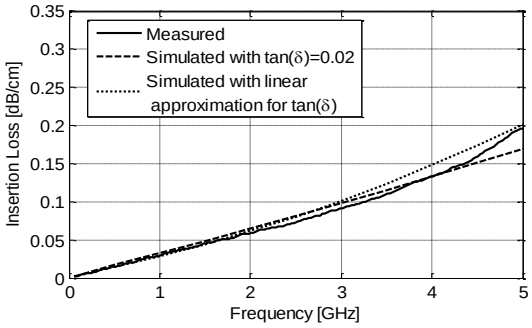

Fig. 9b. Measured and simulated insertion loss of the copper etched line.

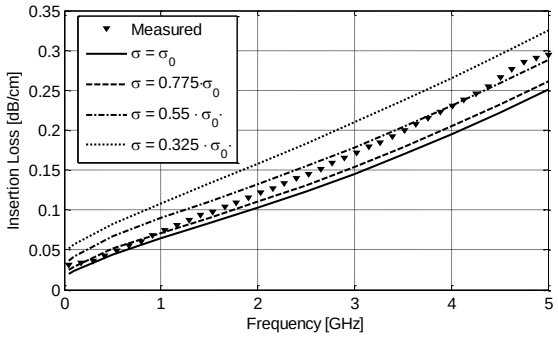

Fig. 10a. Simulated insertion loss of the screen printed line with various conductivities.

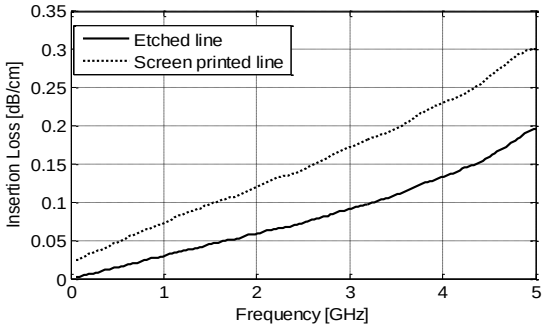

Fig. 10b. Measured insertion loss of the screen printed and copper etched lines.

The simulated and measured insertion loss of the screen printed and copper etched lines are shown in Figs. 9a and 9b, respectively. The results show good agreement between the simulation and measurement for the copper etched line. For the screen printed line, a noticeable discrepancy starts to emerge after 1 GHz. To find out if the physical mechanism behind this is lower than expected conductivity, another set of simulations, where the conductivity of the screen printed line was decreased down to 32.5% of the nominal conductivity (σ_0), while using the frequency dependent loss model for the FR-4 board, was conducted. The obtained results shown in Fig. 10a suggest that the conductivity of the screen printed line is in the range of 55% to 77.5% of the nominal value. Finally, the performance comparison of the screen printed and copper etched line is summarized in Fig 10b. Although the performance difference between the screen printed and copper etched line is seen to increase with frequency (up to 0.1 dB at 5 GHz), within the UHF RFID frequencies the difference is less than 0.05 dB to the advantage of the copper etched line. This is a very encouraging result for the use of printable electronics in tag

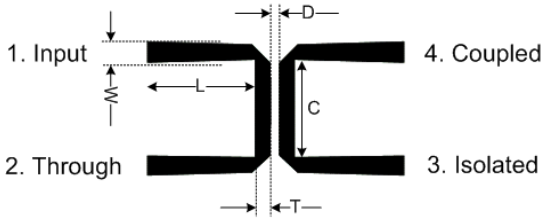

Geometrical parameters in millimeters

W	D	C	T	L
3.8	19.8	3.0	17.5	1.6

Figure 11. The studied microstrip coupled-line coupler.

fabrication.

As an example of a more complicated transmission line component, a coupled-line coupler shown in Fig. 11 was designed for the nominal operation frequency of 2.45 GHz with the specified −20 dB coupling between the input port (port 1) and the coupled port (port 4). Here, Agilent ADS high frequency circuit simulator [94] was the main design tool, while the final results were also verified using HFSS. The design optimization was done for the copper etched device only and one of the main goals was to determine whether the device which is optimized for copper etching could be screen printed instead without compromising its performance. In addition to input matching, coupling and port isolation, the insertion loss in the through path (from port 1 to port 2) based on equation (30), was evaluated.

The measured and simulated operation of the copper etched coupler is presented in Fig. 12a and the measured operation of the copper etched and screen printed couplers are compared in Fig. 12b. These results indicate that changing the fabrication process from copper etching to screen printing has actually little impact on operation of the coupler in

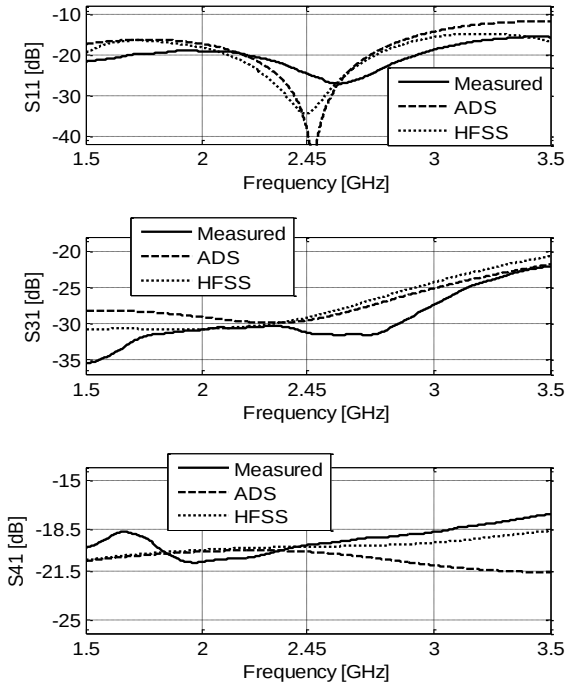

Fig. 12a. Simulated and measured S-parameters of the etched coupler.

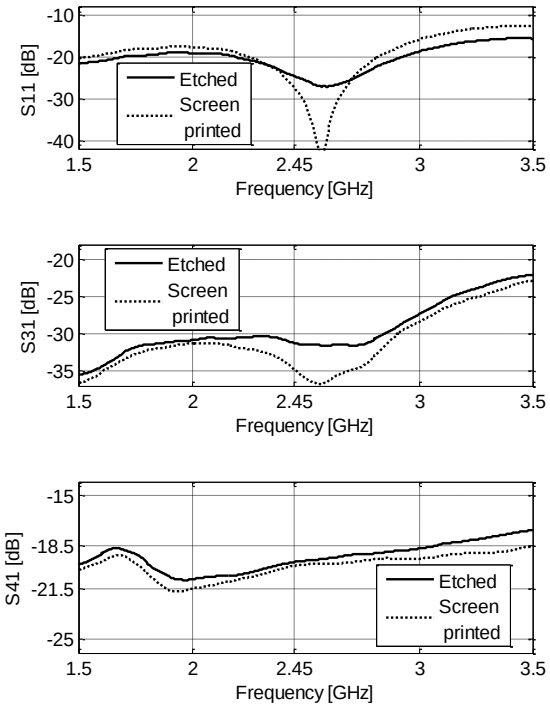

Fig. 12b. Measured S-parameters of the etched and screen printed couplers.

Fig. 13. Measured insertion loss in the through path (from port 1 to port 2) of the copper etched and screen printed coupler.

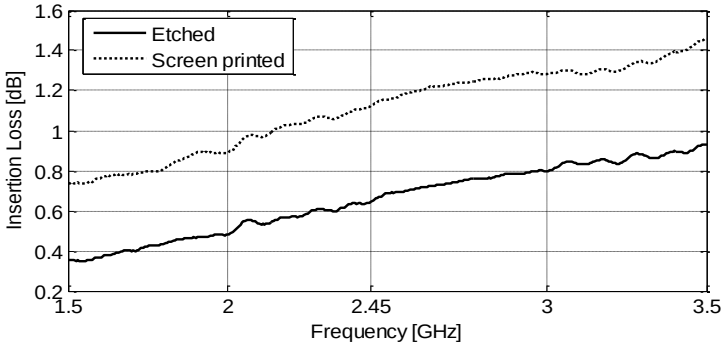

terms of the input matching, coupling, and port isolation. Notably, the difference in the through path insertion loss is only 0.2 dB to the advantage of the copper etched coupler (Fig. 13).

Overall, the results show that while the accurate modelling of the conductor loss in printed microwave devices is challenging, the operation of printed microstrip line components, such as the coupled-line coupler, are well predicted with conventional high frequency simulation procedures.

Screen and Gravure Printed Tags

The research on screen printed microstrip line components provided valuable insight on the design of printed microwave devices. Encouraged by the obtained results, the experimentation was continued with fully assembled tags with screen and gravure printed antennas. This provided new information on the tag design aspects related to the ink morphology typical to studied printing techniques [II].

For the experimentation, antenna patterns were designed using HFSS. Firstly, for copper etching, a quarter-wavelength dipole type tag antenna with an embedded T-matching network was created on PET film. The design goal was a well-performing tag equipped with Higgs-2 UHF RFID IC from Alien Technology [65]. Using the conductivities reported by the ink manufacturer (Table 3) and the measured thickness of 21.5 µm and 3.8 µm for the screen and gravure printed conductors, respectively, the copper antenna was modified in order to achieve the same simulated frequency of operation for the printed tags for fair comparison. The comparison of the antenna structures adapted for the screen and gravure printed conductors, however, showed that there is little difference between them. In fact, it was sufficient to use exactly the same antenna structure for both (Fig. 14).

Based on the simulated power reflection coefficient (Fig. 15), all tags are expected to exhibit similar frequency responses with the peak performance around 866 MHz. However, the measured realized gain of the gravure printed tag has somewhat different characteristics (Fig. 16). Further investigation with an optical microscope revealed that in the gravure printed tag, a narrow conductor in the antenna matching network carrying a high current density was printed imperfectly with a ragged edge (Fig. 17). In simulations, a similar frequency shift was reproduced by reducing the trace width (parameter *s* in Fig. 14) down to 30% of its nominal value. The corresponding simulated power reflection coefficient is designated as the “realized” curve in Fig. 15.

Despite the non-optimal gravure print outcome, the printed tag still achieves the measured read range of 4.3 m at 866 MHz (*EIRP*=3.28 W) [II]. The measured peak realized gain, however, occurs at 815 MHz with a 1.3 dB higher value. This corresponds to a 16% potential increase in the tag read range. Therefore, given that an appropriate operation frequency was achieved, the read range of 5 meters could be attained. The fabrication of the screen printed tag was more successful and the simulated and measured frequency of operation is in good agreement. The screen printed tag achieves the measured tag range of 7.9 m [II]. Finally, the measured read range of the copper etched reference and the commercially available Alien Squiggle tag (also equipped with Higgs-2 IC) both achieve

Geometrical parameters in millimeters.

Param.	W	L	t	s	u	v
Etched	9	10	15.6	0.5	2	6
Printed	8	97	17	0.5	2	6

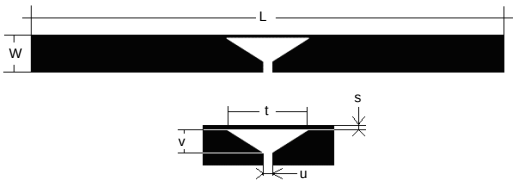

Fig. 14. Studied tag antenna structures.

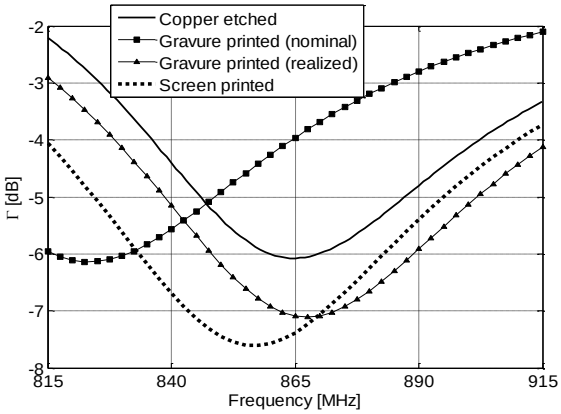

Fig. 15. Simulated power reflection coefficient.

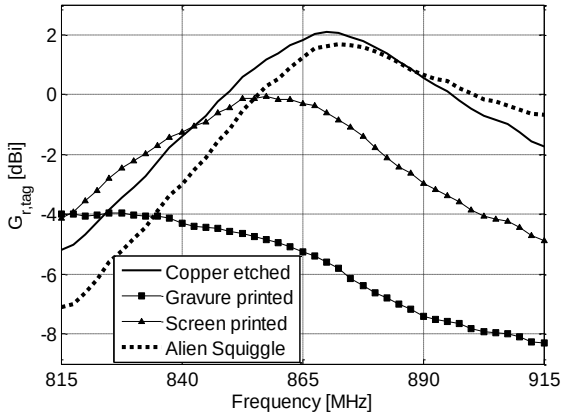

Fig. 16. Measured realized gain.

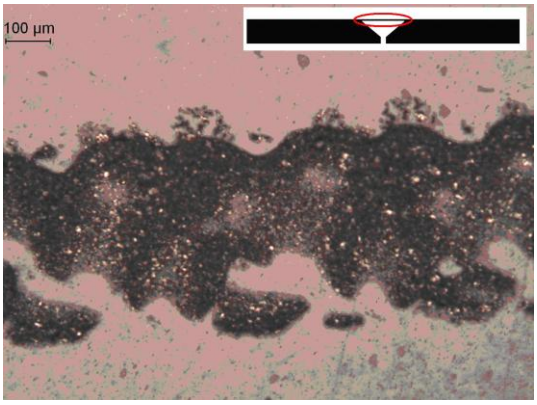

Fig. 17. Close-up of a narrow trace in the gravure printed antenna.

the read range of approximately 10 m [II] which shows that a tag based on the studied antenna structure can achieve similar performance as products available on the markets.

Since the etched and printed antennas are nearly identical, the performance differences at the peak performance frequencies are predominantly due to the properties of the antenna conductor material. However, it should be pointed out that while the conductor in the copper etched and screen printed antennas is thicker than the conductor skin depth defined in equation (1), the thickness of the conductor in the gravure printed antenna is only half the skin depth. Therefore, additional conductor loss due to the current crowding phenomenon may have reduced the performance of the gravure printed tag. Nevertheless, the printed layer thickness of 3.8 µm is a typical value for the technique and therefore the comparison between the screen and gravure printed tags is considered fair. In fact, printing sub-skin-depth layers to save ink may be advantageous from the cost-performance perspective, since the 4-to-5 meter read range predicted for the gravure printed tag is without a doubt sufficient in many applications.

Overall, the experimentation showed that, while tags with printed antennas can achieve competitive performance against copper tags, it is important to consider the aptitude of each fabrication technique for printing a specific antenna pattern. For instance, gravure printing enables rapid fabrication of large conductive areas, but e.g. the antenna

pattern studied in [II] should be re-adjusted for this fabrication technique so that narrow traces would not be included at least in the antenna matching network where the non-ideal print outcome may compromise the tag performance. On the other hand, inkjet printing is a prominent technique for producing fine-detail conductive patterns and antennas composed of narrow traces [31].

3.3 Wireless Measurement of RFID IC Impedance

The lack of accurate knowledge of the tag IC impedance may keep the tag designer from getting the full benefit out of the design techniques and simulation tools. To improve the reliability of the tag design process, a wireless technique to measure the IC impedance at the wake-up power of the chip, including the IC mounting parasitic, is presented in [III].

In wired measurement configurations that have been used to determine the IC impedance, an RFID tester is employed to determine the lowest output power of the vector network analyzer (VNA) at which the IC remains operational [70]. In this way, the impedance is measured at the wake-up power of the IC. The IC impedance is, however, capacitive and differs significantly from the conventional 50 Ω system impedance of microwave measurement instruments. This is problematic since the sensitivity of VNAs is best around the system impedance with a rapid performance decay for loads differing from it [95]. Static pre-matching with an impedance tuner improves the accuracy of the VNA measurement [71], but this also increases the system complexity. In contrast to the wired VNA measurement, publication [III] presents a wireless approach, where tag antennas with known properties are used as test beds for the IC and its impedance is obtained based on the measured threshold power of three test tags.

From the point of view of tag antenna design, the sole requirement for the test bed antennas is sufficient realized gain over the frequencies of interest to allow the threshold power measurement. To adapt the test bed antennas to provide adequate pre-matching, it suffices to have a rough initial guess for the IC impedance. Additionally, in the formulation presented below, it is assumed that the test bed antennas are non-identical. The structure of the test bed antennas used in [III] is illustrated in Fig. 18. The IC under test is Alien Higgs-3 RFID IC [65] provided by the manufacturer in a strap to facilitate the laboratory-scale chip attachment. Conductive epoxy was used to attach the strap fixture to the test bed antennas.

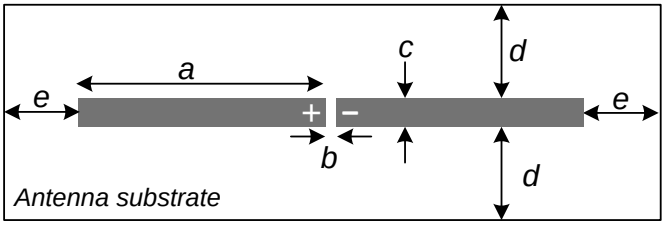

Geometrical parameters in millimeters.

	a	b	c	d	e
Tag 1	74.5	1	3	15	15
Tag 2	79.5	1	3	15	15
Tag 3	84.5	1	3	15	15

Figure 18. Structure of the test bed antennas. Tag IC terminals are connected to + and −.

To extract the IC impedance based on the measured threshold power of the test tags, the corresponding realized antenna gain is first computed for each of the three test bed antennas as explained in Section 3.1. The corresponding antenna-IC power transfer efficiencies (τ) are then solved from equation (20) using the simulated tag antenna impedance and gain, and the IC wake-up power of −18 dBm reported by the manufacturer. Two different solvers, based on FEM (HFSS) and a finite-difference time-domain (FDTD) code based on [96], were used to characterize the test bed antennas in [III]. The extremely good agreement between the results obtained with the two fundamentally different numerical techniques establishes a good level of confidence on the test bed antenna characterization.

According to equation (11), each of the obtained τ values defines a circle in the IC impedance plane. Therefore, the candidates for the IC impedance are the intersection points of the τ circles. Ideally, three of them would be the same point and this would be measurement result. However, due to the measurement uncertainty and slight deviations among the three samples of the IC under test, three intersection points are expected to lie close to each other. Therefore, the measured tag IC impedance is associated with the triplet of the τ circle intersection points, which spans a triangle with minimal circumference in the complex plane. This is illustrated in Fig. 19.

The measurement uncertainty is quantified with a Monte Carlo simulation combined with the circle intersection search. For this purpose, probability density functions (pdf) for the tag antenna resistance, reactance, and gain, as well as for the measured threshold power P_{th} were estimated. As shown by measurements in [70] and [71], the wake-up power of tag ICs remains fairly constant over the global UHF RFID frequencies from 860 MHz to 960 MHz and is therefore assumed as a constant in the simulation. The link loss factor defined in Section 3.1 is also a constant since the measurement configuration is identical for all tags.

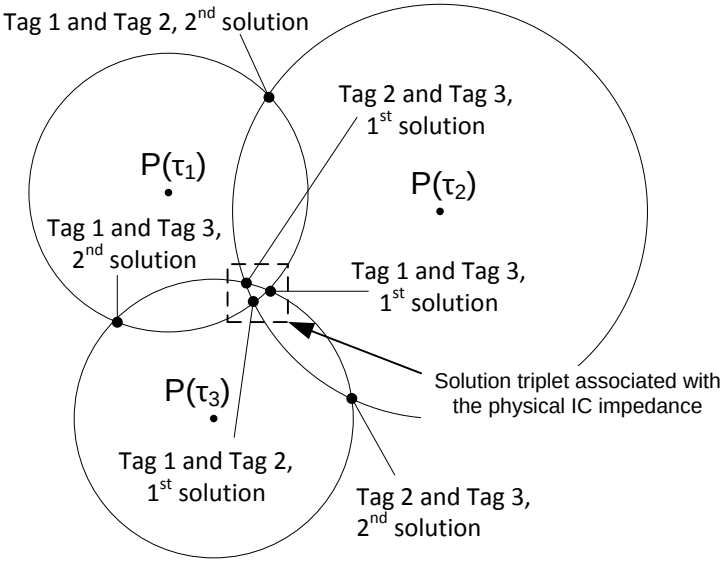

Figure 19. τ circles and the potential IC impedances. The centre points and radii of the circles are given by equation (11).

Based on the principle of maximum entropy, a vector valued random variable $\mathbf{x} = [R_a, X_a, G_{tag}, P_{th}]$, following a multivariate normal distribution $N(\mathbf{x}; \boldsymbol{\mu}, \boldsymbol{\Sigma})$ with mean vector $\boldsymbol{\mu}$ and covariance matrix $\boldsymbol{\Sigma}$, was formed for each test tag. On a given frequency, the mean vector is composed of the simulation results while the mean value for P_{th} is the arithmetic mean of several repeated measurements. The elements of the covariance matrix are

$$\Sigma_{ij} = \begin{cases} \sigma_i^2 & \text{when } i = j \\ \rho_{ij}\sigma_i\sigma_j & \text{when } i \neq j, \end{cases} \tag{31}$$

where σ_i is the standard deviations of variable i and ρ_{ij} is the correlation coefficient between variables i and j. While, the detailed discussion on the statistical properties of the simulated quantities is provided in [III], the standard deviation of the threshold power is simply the sample standard deviation from several repeated measurements. With these data, frequency dependent parametric pdf estimates $N(\mathbf{x}_k; \boldsymbol{\mu}_k(f), \boldsymbol{\Sigma}_k(f))$ for each of the measured tags (k=1,2,3) is obtained.

During the simulation, 30000 random samples are drawn from the pdf*s*. For each tag, call the set of all the sampled data Y_i, where i=1,2,3 is the tag index. Each of the three tag pairs (Tag i & Tag j; i<j and i,j=1,2,3) produces a maximum of two intersection points, so that in total there are six sets of intersection points:

$$\left\{Z_{12}^{(1)}\right\}, \quad \left\{Z_{12}^{(2)}\right\}, \quad \left\{Z_{13}^{(1)}\right\}, \quad \left\{Z_{13}^{(2)}\right\}, \quad \left\{Z_{23}^{(1)}\right\}, \quad \left\{Z_{23}^{(2)}\right\} \tag{32}$$

Supposing that each set contains normally distributed data, six conditional parametric pdf estimates

$$f_{ij}^{(1)}\left(Z \middle| (Y_i, Y_j); \boldsymbol{\mu}_{ij}^{(1)}, \boldsymbol{\Sigma}_{ij}^{(1)}\right), \quad f_{ij}^{(2)}\left(Z \middle| (Y_i, Y_j); \boldsymbol{\mu}_{ij}^{(2)}, \boldsymbol{\Sigma}_{ij}^{(2)}\right), \tag{33}$$

with i<j and i,j=1,2,3 are obtained for the τ circle intersection points. Here the mean vectors contain the real and imaginary parts of the most probable intersection points, given the statistical properties assigned for each of the measured and simulated the input quantities. Thus, the potential IC impedance is associated with the one of the eigth triplets

$$\left(\boldsymbol{\mu}_{12}^{(n_1)}, \boldsymbol{\mu}_{13}^{(n_2)}, \boldsymbol{\mu}_{23}^{(n_3)}\right); \quad n_1, n_2, n_3 \in \{1,2\}, \tag{34}$$

which has the minimal circumference in the complex plane. By approximating the corresponding conditional pdf*s* given in equation (33) as independent and applying Bayes' formula, one obtains an estimate for the normal distribution of the IC impedance given all the sampled data:

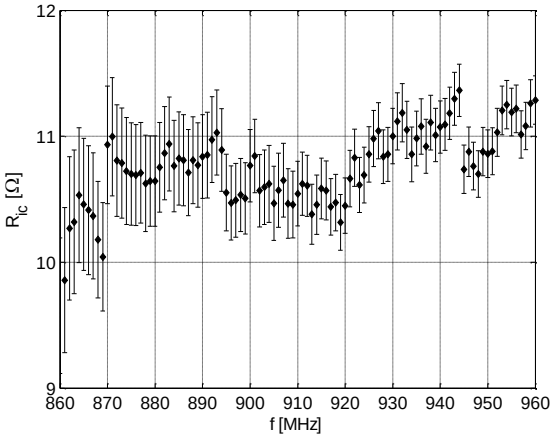

Figure 20a. Mean of the IC resistance with one standard deviation bars using FEM simulation data.

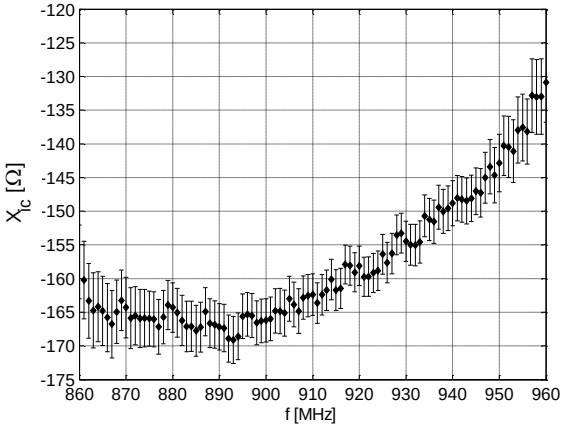

Figure 20b. Mean of the IC reactance with one standard deviation bars using FEM simulation data.

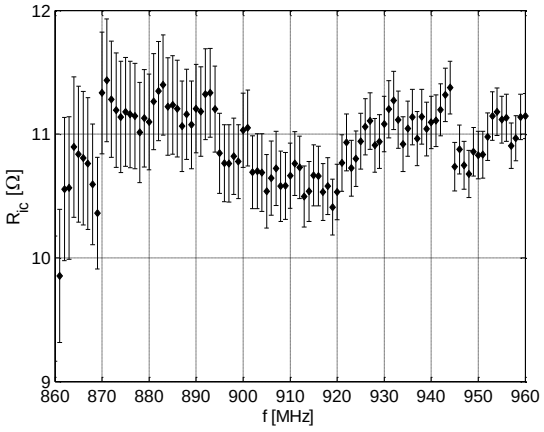

Figure 21a. Mean of the IC resistance with one standard deviation bars using FDTD simulation data.

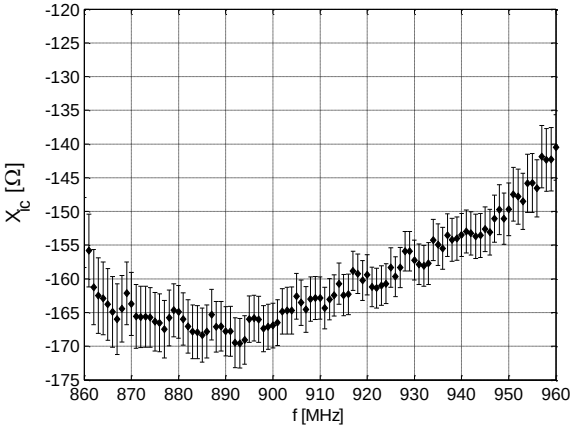

Figure 21b. Mean of the IC reactance with one standard deviation bars using FDTD simulation data.

$$g\left(Z_{ic}\middle|(Y_1,Y_2,Y_3);\boldsymbol{\mu}_t,\boldsymbol{\Sigma}_t\right)= f_{12}^{(n_1)}\left(Z\middle|\left(Y_1,Y_2\right);\boldsymbol{\mu}_{12}^{(n_1)},\boldsymbol{\Sigma}_{12}^{(n_1)}\right) \times f_{13}^{(n_2)}\left(Z\middle|\left(Y_1,Y_3\right);\boldsymbol{\mu}_{13}^{(n_2)},\boldsymbol{\Sigma}_{13}^{(n_2)}\right) \times f_{23}^{(n_3)}\left(Z\middle|\left(Y_2,Y_3\right);\boldsymbol{\mu}_{23}^{(n_3)},\boldsymbol{\Sigma}_{23}^{(n_3)}\right), \tag{35a}$$

$$\boldsymbol{\Sigma}_t=\left(\left(\boldsymbol{\Sigma}_{12}^{(n_1)}\right)^{-1}+\left(\boldsymbol{\Sigma}_{13}^{(n_2)}\right)^{-1}+\left(\boldsymbol{\Sigma}_{23}^{(n_3)}\right)^{-1}\right)^{-1}, \tag{35b}$$

$$\boldsymbol{\mu}_t=\boldsymbol{\Sigma}_t\left(\left(\boldsymbol{\Sigma}_{12}^{(n_1)}\right)^{-1}\boldsymbol{\mu}_{12}^{(n_1)}+\left(\boldsymbol{\Sigma}_{13}^{(n_2)}\right)^{-1}\boldsymbol{\mu}_{13}^{(n_2)}+\left(\boldsymbol{\Sigma}_{23}^{(n_3)}\right)^{-1}\boldsymbol{\mu}_{23}^{(n_3)}\right). \tag{35c}$$

The mean of the combined distribution given in equation (35c) is considered as the outcome of the measurement, while the variances in IC resistance and reactance form the diagonal of the combined covariance matrix given in (35b).

Figures 20-21 show the measured IC impedance with standard deviation limits for the IC resistance and reactance using both FEM and FDTD to characterize the test bed

antennas. Compared with the FDTD test bed characterization, the FEM-based result shows a steeper rise trend in the reactance after 920 MHz, but both methods predict the local reactance minimum at around 890 MHz. The standard deviations depict the uncertainty of the measured impedance and they are nearly equal using either simulation data. This suggests that the reliability of the proposed measurement method does not depend on the CEM tool used to characterize the test bed antennas, as long as the simulation model includes the essential physical details. The major practical value of the results presented in Figs. 20-21 is further highlighted in Section 4 presenting three novel prototype tags [V-VII] with the antennas optimized using the measured IC impedance.

In addition to the measurement of the IC impedance in its energy harvesting state, a simular procedure can be used to measure the IC impedance in its modulating state [III]. This is an interesting topic for future research, since eventually, as the IC wake-up powers are being improved, the co-optimization of antenna-IC power transfer efficiency and the tag modulation efficiency, may be needed to maximize the overall system performance. This cannot be done without the accurate knowledge on the IC impedance in both states.

4 CASE STUDIES

In Section 2, the adaptation of the general knowledge on antennas for the specific needs of the tag antenna design was discussed, a new numerically efficient framework to relate given impedance tolerances to the corresponding tolerance in antenna-IC power transfer efficiency was presented, and a set of fundamental tag performance parameters were introduced. Section 3.1 presented how these performance parameters are obtained from measurements on fully assembled tags. The experimental results discussed in Section 3.2 verified that compared with tags with copper antennas, antennas fabricated using printable electronics, which has great potential to enable the integration of antennas with various unconventional platforms, provide similar performance. Moreover, a new technique to measure the tag IC impedance was introduced in Section 3.3 to improve the reliability of the simulation based tag design. This section presents novel tag antennas created using the design framework introduced in the previous sections. The developed antennas provide improved performance in challenging applications and excellent structural properties for seamless integration with objects of different shapes, sizes, and material contents.

4.1 Water Bottle Tag

The proximity of water is problematic for the operation of microwave antennas. While this is a widely acknowledged tag performance bottle neck in item-level RFID [12]-[14], so far only general purpose platform tolerant antennas have been reported exhibiting adequate performance in the proximity of water or the aqueous human body [34]-[38]. To achieve sufficient performance on unfavorable antenna platforms, these structures include a separating material layer underneath the antenna, to alleviate the adverse effects arising from the platform properties. In contrast, the inconspicuous water bottle tag presented in [V] does not require an additional platform and is therefore well-suited for fabrication in the backside of an ordinary product label or directly onto the bottle using printable electronics.

As a system level specification, a sufficient read range for the water bottle identification tag is 1-to-2 meters, covering all the spatial angles in the plane perpendicular to the bottle axis. Moreover, considering the practical application, the sufficient read range has to be verified also in the scenario with multiple tagged bottles close to each other. Taking into account the tag IC wake-up power of −18 dBm, equation (3) implies that with $EIRP$ = 4W, the realized tag antenna gain of approximately −10 dBi is required to achieve the read range of 1-to-2 meters. Given that good impedance matching can be arranged ($\tau \approx 1$), this means that an omnidirectional antenna ($D_{tag} \approx 1.64$) with radiation efficiency above 0.05 could be used. However, water has considerable electrical conductivity and high permittivity at the microwave frequencies [97] and therefore a strong interaction between the antenna and the water is to be expected. Although high-permittivity materials can help in antenna miniaturization [22][23][98][99];[VII], the proximity of water cannot

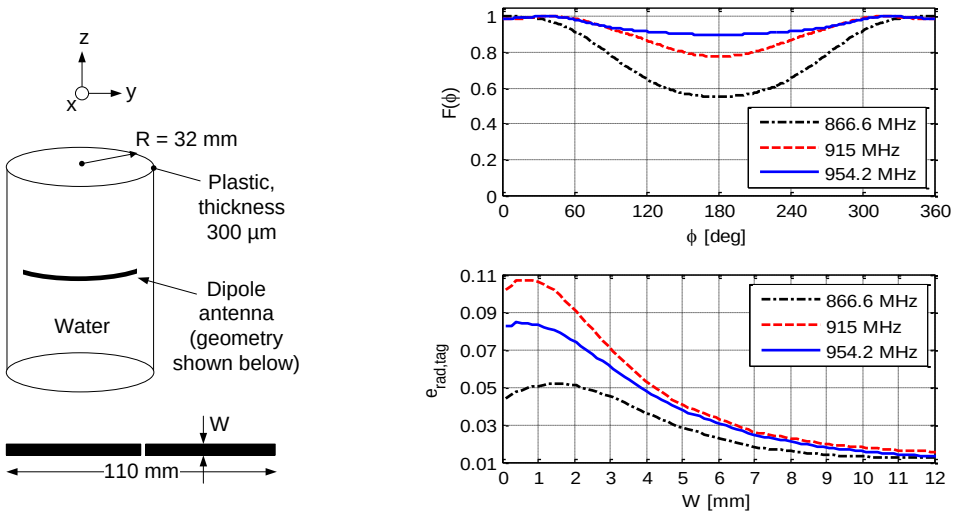

Figure 22. Top right: simulated normalized power pattern of a dipole with W=1 mm in the xy plane. Bottom right: simulated radiation efficiency of the dipole versus the dipole width.

be considered favorable for the present design due to its high dielectric loss. In fact, the proximity of water makes it challenging to attain the 1-to-2 meter read range with an antenna attached directly onto the bottle surface.

Another major challenge is to achieve the uniform radiation over the spatial angles in the plane perpendicular to the bottle axis. While an antenna array on a cylindrical surface could provide this [100], this may not be a feasible approach for the water bottle tag antenna. On the other hand, a dipole antenna bent on a cylindrical surface and on human arm have are reported exhibiting the desired uniform radiation property [36][38]. This motivated the development of an antenna based on a single radiating element for the water bottle tag.

Simulations with HFSS on a center-fed dipole antenna bent onto a water-filled cylinder made of plastic (Fig. 22), showed that the xy plane the power pattern $F(\varphi)$ does not exhibit deep nulls like the power pattern of an isolated straight dipole does. Interestingly, this was achieved with a dipole length less than half of the cylinder circumference. Another key observation was that with a fixed dipole length, the best radiation efficiency ($e_{rad,tag}$) is achieved with a relatively narrow dipole width in the order of 1 mm. These new findings on the radiation properties of the dipole antenna in the proximity of the water are exemplified in Fig. 22.

In the final design stage, an accurate model of a regular cylindrical 0.5 l water bottle was implemented in HFSS for more holistic antenna optimization. In this process, the measured tag IC impedance [III] was used to provide the antenna-IC power transfer efficiency required for the evaluation of the tag read range based on equation (23). Since the antenna radiation efficiency is severely limited by the presence of the water, the antenna tends to have low input resistance. Therefore a folded dipole antenna, which can potentially have high input impedance compared with that of a regular dipole of the same length [12][41], was considered advantageous.

Since the achievable radiation efficiency is proportional to the volume occupied by the

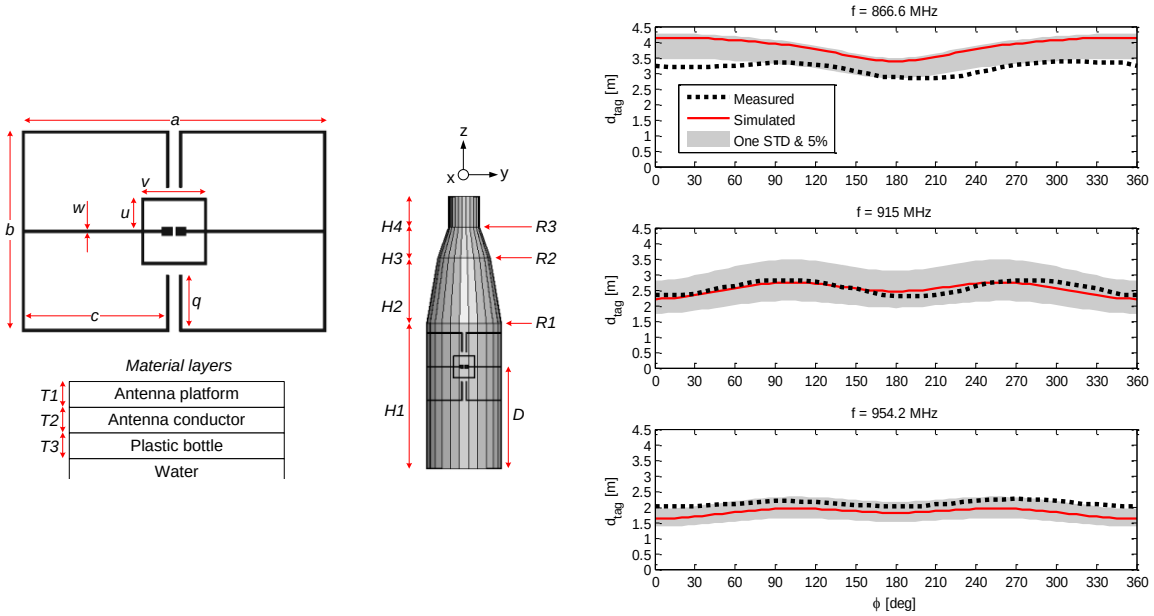

Figure 23. Left: simulation model and its defining parameters. Right: simulated and measured read range patterns of the tag in the xy-plane and the associated uncertainty envelopes.

antenna, it is best to try to make use of the available space as much as possible, while avoiding closely spaced traces with opposite currents [19][22][23]. Taking into account that increasing the width of a straight dipole beyond 1 mm was not beneficial in the initial study (Fig. 22), the selection of the prototype antenna geometry converged to a three-wire antenna with up to 3 mm trace width, occupying the area of an ordinary product label. Finally, open-circuiting the two folded dipole arms in the middle and bending them inward as shown in Fig. 23 was found beneficial for the radiation efficiency with minor effects on the other antenna properties. Thus the impedance matching and final tuning of the antenna shape was based on the antenna geometry shown in Fig. 23.

The built-in genetic optimizer in the HFSS version 12 was employed to maximize and uniformize the tag read range pattern in the xy plane of Fig. 23 at the European, U.S. and Japanese UHF RFID center frequencies (Table 1). The optimization was done first for parameters *a*, *b* and *w* to achieve the uniform radiation pattern with maximal radiation efficiency and afterwards for parameters *u* and *v* to arrange a good conjugate impedance matching with the tag IC. This is based on the T-matching approach [21], where an inductive loop is formed around the antenna feed point to achieve the desired inductive antenna impedance. As seen from Fig. 23, the T-matching loops were formed on both sides of the feed point in order to preserve the symmetry of the antenna structure.

The publication [V] lists the detailed antenna performance data and shows the optimized values of the geometrical parameters. Here it suffices to point out that footprint of the prototype antenna is 88×58 mm^2, which is approximately the size of an ordinary product label, while the achieved tag read range in the xy plane is shown in Fig. 23. The gray uncertainty envelopes enclosing the simulated graphs in Fig. 23 are obtained using the calculation of the minimum and maximum values for the antenna-IC power transfer efficiency with the numerical efficient formulation presented in [IV]. In this calculation,

the maximum variation of 5% in the simulated antenna resistance and reactance was assumed while the one standard deviation uncertainties for the measured IC resistance and reactance [III] were used. Additionally, the maximum variation of 5% was assumed independently for the simulated tag antenna gain. The measured read range is obtained with the power ramping method discussed in Section 3.1 using Voyantic Tagformance RFID measurement system. The read range results at different frequencies are referred to the regulated EIRP values listed in Table 1.

As seen from Fig. 23, the prototype tag achieves over 2 m read range over all the spatial angles in the plane perpendicular to the bottle axis, at all the measured frequencies. Importantly, for the majority of spatial angles, the measured result is also contained in the uncertainty envelope. This implies that the simulation-based design has been successful within the limits of the of expected design uncertainty.

Overall, the results are encouraging, but for more practical performance evaluation, the read range of the prototype tag was measured also in the two multi-bottle scenarios illustrated in Fig. 24. This experiment shows how the tag read range is affected by tag-to-tag coupling and nearby bottles shadowing the addressed tag. Due to the symmetry of the bottle arrangements, the measurement was conducted only on one tag in each scenario. Most importantly, in neither of the studied configurations, dead zones emerged in the tag read range patters. In particular, in configuration 2 of Fig. 24, where the measured tag is in physical contact with two other tags and shadowed by the water bottles from all sides, over 1 m tag read range is still achieved at all the spatial angles in the plane perpendicular to the bottle axis. Moreover, the read range covering 80% of the measured spatial angles

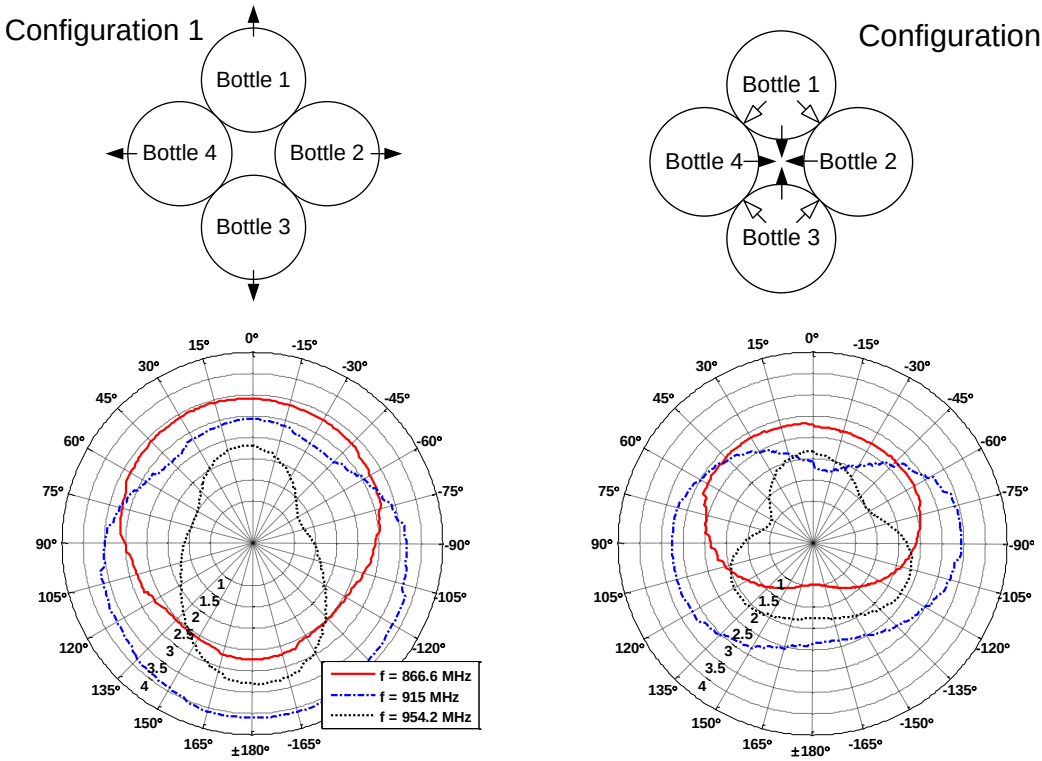

Figure. 24. Measured read range in multi-bottle configurations. Solid arrows show the direction where the tags are facing. Outlined arrows indicate where the tags are in physical contact.

is 1.3 m, 2.3 m, 1.4 m, at 866.6 MHz, 915 MHz, and 954.2 MHz, respectively. This gives perhaps better understanding on the overall read range coverage of tag than a single minimum value.

As emphasized throughout the above design summary, the antenna for the water bottle identification was designed so that it does not require a separating material layer in between the antenna and bottle surface. Thus, antenna fabrication with pad printing technique [32] directly onto the bottle surface using conductive thick film ink is an interesting topic for future research. Alternatively, as the narrow antenna trace was found favorable in this application, the antenna shape is well suited for fabrication with inkjet printing [31] in the backside of an ordinary product label.

4.2 Metal Mountable Tag for Large Conductive Items

Compared with water, the proximity of metal has even more severe impact on the functioning of antennas. This is because the image current induced in the nearby metal acts as a secondary source of radiation with an approximately opposite phase compared with the antenna itself. Thus, the radiated field obtained as the superposition of the two components is weak and the antenna radiation efficiency is low. In addition, separation from a metal surface (even a small one in size compared with the antenna) can significantly affect the antenna radiation pattern and impedance [40][43].

Antennas including a ground plane, which prevents the radiating antenna current from interacting with the conductive platform, are therefore possible candidates for metal mountable tags. Some of this type of antennas, such as the microstrip patch antenna, can also be made relatively low-profile, typically in the order of 1-to-3 mm at the UHF RFID frequencies. This is sufficient for tag development and compared with omnidirectional antennas, such as dipoles and slots, the comparatively high directivity of patch antennas can help to achieve longer read ranges.

To obtain a rough estimate for the obtainable read range of tags based on patch antennas, equation (23) can be used. Evaluation with a tag IC wake-up power of −14 dBm and a fairly typical patch antenna gain of 6 dBi, gives the tag read range of approximately 16 meters. This makes patch antennas an exciting choice for applications, where long read range on conductive platforms is the top design priority. Such applications include the identification of vehicles, train cars, cargo containers, industrial machinery, and other high-value assets.

The metal mountable tag presented in [VI] is based on a rectangular microstrip patch antenna (Fig 25). The input impedance of this type of antenna depends on the feed point and the feeding method, but a typical the antenna impedance is inductive below the fundamental resonance frequency (Table 2). Moreover, the feed point resistance and reactance are increased when moving from the center of the patch towards the edge, while ideally the resistance is zero in the center of the patch. The commonly used feed methods, such as the inset feed or a strategically positioned coaxial probed connected to the patch through an opening in the ground plane, have been developed for achieving good impedance matching with a 50 Ω feed line. [58]

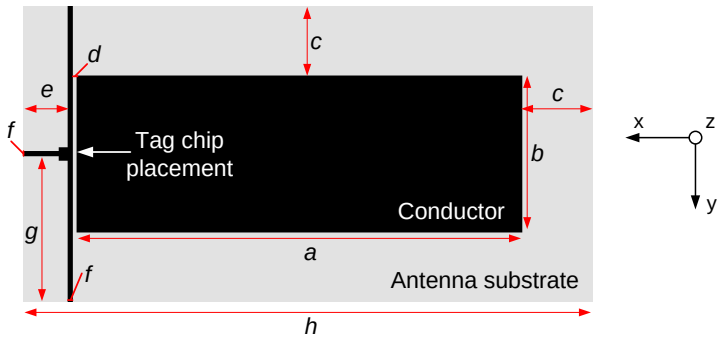

Figure 25. Structure of the prototype tag mountable on large conductive items.

For tag antennas, however, impedance with relatively high inductive reactance in the order 100s of Ωs is desired. In view of this, connecting the tag IC directly at the high impedance patch edge can be an advantageous approach. The metal mountable tag presented in [VI] is based on this approach: one of the tag IC terminals is connected directly to the patch edge, while narrow strips which wrap over the patch edge to avoid drilled vias connect the other IC terminal to the ground. Simulations with HFSS showed that the input impedance can be adjusted over an adequate range by controlling the width of the shorting strips (parameter *f* in Fig. 25), which determines the related inductance per unit length. The antenna directivity is adjusted with the patch shape (parameters *a* and *b* in Fig. 25). To fully account for the effect of metal surface on the antenna performance, all the simulations were conducted with the antenna mounted on 20×20 cm^2 copper plate. For efficient on-metal operation, a clearance of 16 mm between the patch edge and substrate edge (parameter *c* in Fig. 25) was found to suppress interaction of the fringing fields at the edges of the patch with the metal plate sufficiently to provide high radiation efficiency: $e_{rad,tag} = 0.89$.

In the final design stage, the built-in genetic optimizer in the HFSS version 12 was employed to maximize the realized tag antenna gain at 915 MHz. Equation (20) with the measured IC impedance [III] was used in this process. As seen, from Fig. 26a, the impedance of the prototype antenna is little affected when it is mounted on the metal plate. Thanks to the co-design approach where the metal plate was included in the simulation model, the peak performance is achieved on metal (Fig. 26b). For design validation, the uncertainty bounds shown in Fig. 26b were obtained using the numerically efficient computation of the minimum and maximum values for the antenna-IC power transfer efficiency formulated in [IV]. Maximum 5% variation in the antenna resistance and reactance and the one standard deviation uncertainty in the measured IC impedance reported in [III] were used to compute the presented bounds. The realized gain and tag read range were measured in air and on metal with the power ramping method discussed in Section 3.1 using Voyantic Tagformance RFID measurement system.

In conclusion, the simulation and measurement results presented in Fig. 26b are in excellent agreement and the simulation-based design is validated within the considered limits of uncertainty. With the tag is mounted on 20×20 cm^2 copper plate, the measured realized tag antenna gain attains the maximum value of 6.7 dBi at 915 MHz corresponding to the read range of 25 m (*EIRP* = 4 W), in free space conditions. Considering the antenna

size-performance ratio, this is competitive against state of the art (Table 4) and to our knowledge the achieved read range is among the highest reported for metal mountable tags for large conductive items.

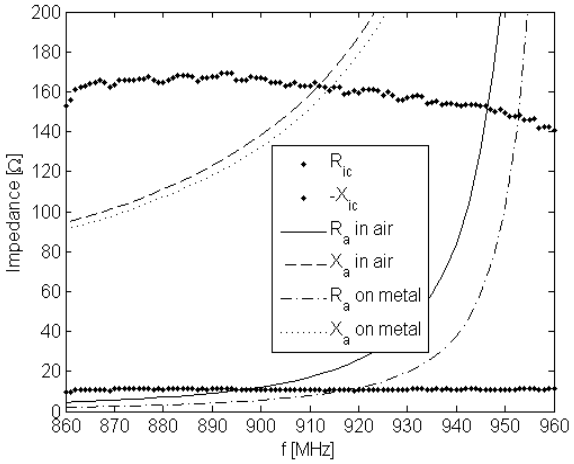

Figure 26a. Simulated antenna impedance and the conjugate of the IC impedance.

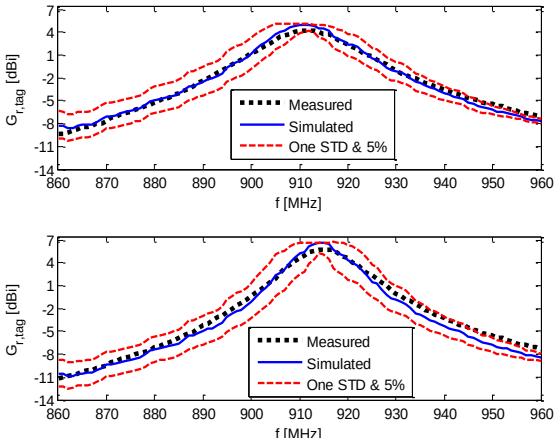

Figure 26b. Simulated and measured realized gain in air and on 20×20 cm^2 copper plate in the direction of the positive z axis in Fig. 25

Table 4. Comparison against state of the art.

Ref.	[45]	[46]	[47]	[48]	[49]	This work
Tag size [mm^3]	62×51.3 ×3	70×24 ×3	110×80 ×0.8	80×80 ×2	120×35 ×5	131×68 ×3.3
Structure	PIFA	Two shorted patches joined by the tag IC	Trapezoid patch	Four shorted patches. Tag IC in a proximity coupled loop.	T-shaped slot on a foam layer	Rectangular patch with inductive feed network
P_{ic0} [dBm]	−18	−18	−14	−14	−14	−18
d_{tag} (d_{tag}*) [m]	13.2	2.8 (11.2)	4.8 (10.7)	3.6 (16)	14 (22.1)	25
Metal plate [cm^2]	46×46	17×17	40×40	20×20	20×40	20×20

d_{tag}* is the reported d_{tag} referred to P_{ic0} = −18 dBm and EIRP = 4 W under perfect polarization alignment.

4.3 Metal Mountable Tag for Small Conductive Items

For making RFID ubiquitous, the tag size and cost-performance ratio are major concerns. While the metal mountable tag based on a patch antenna [VI] discussed in Section 4.2 is well-suited for tracking of large high-value assets, smaller antenna solutions are required in the identification of smaller items. Taking into account that small everyday item is likely to be less valuable, structurally simple antennas based on a single conductor layer

are preferred to achieve lower tag cost. However, few low-profile single layer antennas have been reported for metal mountable tags [54][55] and they have relatively large footprints. On the other hand, more research results on the miniaturization of patch antennas consisting of two or more conductor layers has been published [50]-[53]. In contrast, the small antenna for metal mountable tags presented in [VII] is a slot type radiator. The advantages of a slot antenna in this application include: simple structure (single conductor layer and no need for vias), omnidirectional radiation pattern for reliable energy harvesting, and inherently inductive impedance below the fundamental resonance frequency to facilitate the impedance matching with capacitive tag ICs.

A novel feature in the design is the ceramic substrate composed of Barium Titanate ($BaTiO_3$) as the main component (90%) and Aluminium Oxide (Al_2O_3) (10%) to provide sufficient durability for practical applications. The molecular properties of $BaTiO_3$ enable potentially high permittivities compared with regular microwave circuit board materials [101][102]. As an antenna substrate, such material can be utilized in lowering the fundamental resonance frequency of an antenna of given. This helps to achieve extremely small antenna size [22][23][98][99];[VII]. Antennas for metal mountable tags benefit from the high-permittivity substrate also in another way: the electrical distance between the antenna and the metal surface is increased. This helps to mitigate the adverse effects due to the image current. As $BaTiO_3$ may have significant dielectric losses [98] and the added Al_2O_3 is decreases the permittivity of the compound compared with pure $BaTiO_3$, the values ε_r=39 and $\tan\delta$=0.02 were used to model the ceramic substrate. This estimate was justified through the comparison of simulation and measurement results on six different designs based on dielectric parameters $\tan\delta$=0.02 and ε_r=37,38,…,42, as explained in [VII].

Since the image current in the metal surface beneath the tag is a major factor to consider in the design of antennas for metal mountable tags, an initial study with a dipole antenna and a slot antenna placed on a ceramic $BaTiO_3$ disk (diameter: 27.5 mm, thickness 2.75 mm) backed by a copper plate with size of 3×3 cm^2 was conducted. The ampli-

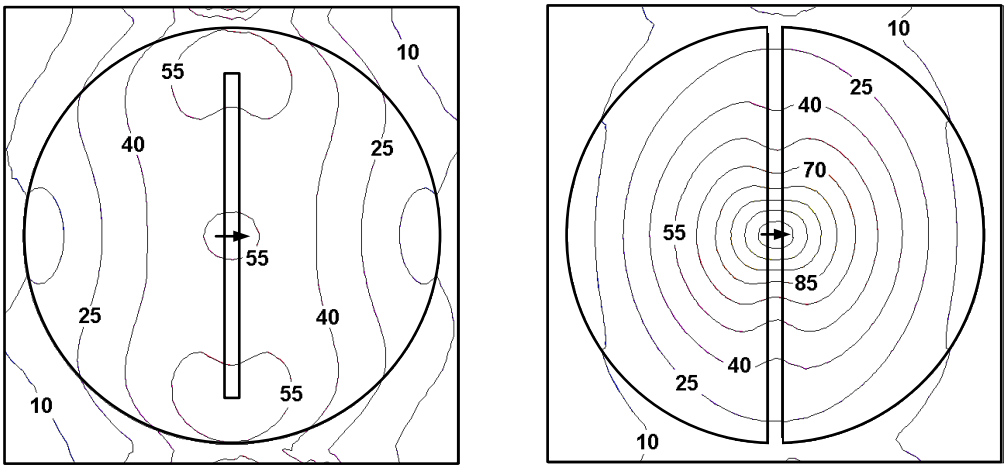

Figure 27. Simulated surface current density amplitude [A/m] in a copper plate beneath slot (on the left) and dipole (on the right) antennas, both accepting 100 mW power. The impressed source current is indicated with the black arrows.

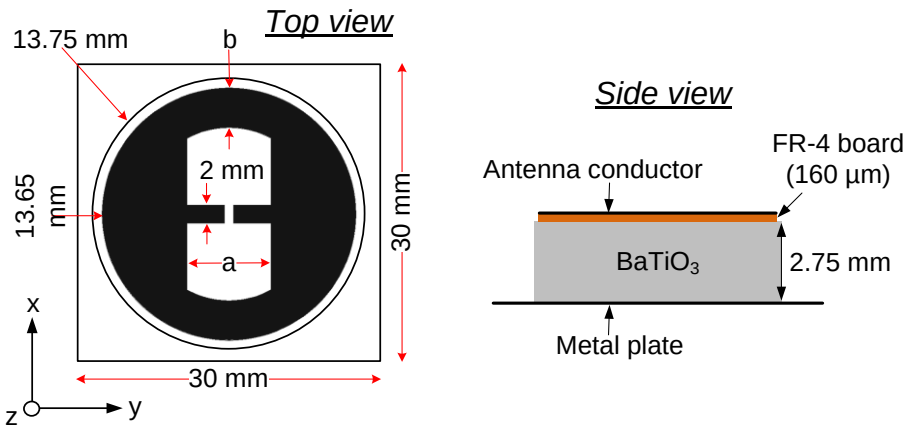

Figure 28. Structure of the prototype tag mountable on small conductive items.

tude of the simulated surface current density in the copper plate in case of a dipole and slot antenna is shown in Fig. 27. Shapes of these antennas were chosen in accordance with the small antenna design principles to occupy the available space with conductor as much as possible, while avoiding current cancellation [19][22][23]. As seen from the results, the peak current in the copper plate due to the slot antenna is much lower than that of the dipole, while the overall area with the surface current density amplitude less than 55 A/m is similar for both antennas. Based on this comparison, the slot configuration was chosen for further development.

As the slot antenna radiation originates predominantly from the current in the vicinity of the slot edge, the shape of the canonical type rectangular slot was modified further in order to achieve conjugate matching with the tag IC. In practice, parameters *a* and *b* shown in Fig. 27 were adjusted to maximize the antenna-IC power transfer efficiency at 915 MHz. Equation (9) with the simulated antenna impedance and measured tag IC impedance [III] were used in the calculation.

To facilitate the testing, the prototype antenna is fabricated on thin copper clad FR-4 board (thickness: 0.16 mm) using the regular milling method. The board is then mounted on $BaTiO_3$ substrate as shown in Fig. 28. For consistency, the board was included in the simulations for design optimization. Recalling that the aim of the design is to develop a tag for the identification of small metallic items, the potential improvement in the antenna directivity due to an electrically large metal plate backing the tag antenna cannot be expected. Therefore, the final design optimization was conducted with the antenna mounted on a small 3×3 cm^2 metal plate. The parameter values to describe the prototype antenna are a=9 mm and b=4.3 mm. The relevant simulated antenna performance data is summa-

Table 5. Simulated antenna performance at 915 MHz. Values of the radiation properties are listed in the direction of the positive z axis in Fig 28.

Z_a [Ω]	Z_{ic} [Ω]	τ	D_{tag} [dBi]	$e_{rad,tag}$	G_{tag} [dBi]	$G_{r,tag}$ [dBi]	d_{tag} [m]
16.8+j158	11−j162	0.93	2.6	0.011	−16.8	−17.2	1.8

rized in Table 5.

As an experimental performance evaluation, the tag read range was measured with the power ramping method discussed in Section 3.1 using Voyantic Tagformance RFID measurement system. The measurement results are presented in Fig. 29. At 915 MHz, the simulation overestimates the read range by approximately 60 cm compared with the measurement. This is likely due to larger than expected dielectric loss in the ceramic substrate, but most importantly the measured results verify the principal design goal: 1-to-2 meter tag read range on small metal plates. On larger plates, the antenna directivity is increased and thereby longer read ranges up to 2.85 m on 20×20 cm^2 plate are achieved. This performance exceeds state of the art (Table 6).

Due to its simple structure based on only a single conductor layer, the prototype antenna can be fully fabricated in a printable electronics process. In the future, we aim to deposit the antenna directly on a flexible $BaTiO_3$-polymer composite substrate using inkjet printing. This will allow the development of small and flexible metal mountable tags.

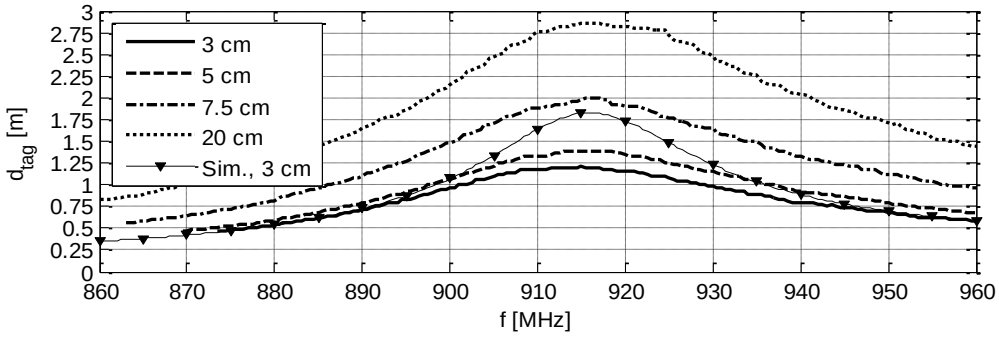

Figure 29. Measured and simulated tag read range in the direction of the positive z axis, on square metal plates of various sizes.

Table 6. Comparison against state of the art.

Ref.	[50]	[51]	[52]	[53]	This work
Tag size [mm^3]	$65 \times 20 \times 1.5$	$32 \times 18 \times 3.2$	$50 \times 50 \times 1.6$	$53 \times 20 \times 3.5$	$27.5 \times 27.5 \times 2.91$
# Cond. layers	2	3	2	2	1
Structure	Two shorted patches joined by the tag IC	As [50] + a non-connected patch in another layer	Slotted patch + IC in a proximity coupled loop	Patch + IC in a proximity coupled loop	Slot antenna on a high-permittivity substrate based on $BaTiO_3$
P_{ic0} [dBm]	−14	−14	−10	−18	−18
d_{tag} (d_{tag}*) [m]	3.1 (6.9)	1.5 (3.3)	2 (5)	2.5	2.85
Metal plate [cm^2]	17×17	17×17	17×17	20×20	20×20

d_{tag}* is the reported d_{tag} referred to P_{ic0} = −18 dBm and EIRP = 4 W under perfect polarization alignment.

5 CONCLUSIONS

The antenna design methodology presented in this work is tailored for the specific needs of tag antennas. This provides holistic tag performance optimization based on modern computational electromagnetics, new analysis tools and design methods for reducing the design uncertainty, as well as a setting for judicious validation of the simulation-based designs through measurements on fully assembled prototypes. Combined with the use of novel electronics materials and new fabrication methods, this provides compelling means for the development of antennas for inconspicuous passive long range UHF RFID tags. [I-VI]

Using the presented design methodology, the development of antennas for tags in challenging applications involving materials, which have adverse effects on the functioning of conventional antennas, was investigated. As a result, three prototype tags exceeding the state of the art performance were proposed [V-VII]. Each tag demonstrates different design choices for achieving an optimal cost-performance ratio in the considered application.

The top priority in the design of the water bottle tag [V] is to achieve sufficient read range coverage around the bottle with an extremely low-profile tag, which conforms seamlessly to the bottle surface. This is challenging due to the presence of dissipative water, but with the co-design approach where the bottle was considered as a part of the antenna, the stringent requirements were satisfied. In fact, the developed antenna does not require an additional platform at all and is therefore fit for fabrication directly on the bottle surface or in the backside on an ordinary product label using printable electronics.

For the identification of large conductive items, such as cargo containers, long read range is paramount. The careful evaluation of the performance of antennas mounted on conductive surface showed that a microstrip patch antenna is perhaps the best choice in this application. It has high directivity and thanks to the ground plane the undesired image current induced in the conductive surface is reduced. These favorable properties combined with a thorough design optimization provided an impressive read range of 25 meters in free space conditions measured for the prototype tag presented in [VI].

For the item-level identification of small everyday conductive items, low tag cost is more important than achieving a very long read range. For this reason, small and structurally simple antennas based on a single conductor layer are preferred. However, meeting these requirements, calls for completely new design approaches. The miniature slot antenna for metal mountable tags presented in [VII] exploits a high-permittivity substrate based on Barium Titanate ($BaTiO_3$) to increase the electrical separation of the antenna from the metal surface and to lower its fundamental resonance frequency for size-reduction purposes. Thanks to the single layer structure, the antenna can also be fully fabricated in printable electronics processes. Moreover, the presented design approach

provides exciting opportunities for creating flexible metal mountable tags on $BaTiO_3$-polymer composite substrates.

Overall, the presented new analysis tools together with modern computational electromagnetics, novel electronics materials, and new fabrication methods, provide compelling means for the development of small and unobtrusive antennas for passive UHF RFID tags. The prototype tags with antennas designed using the proposed methodology together with novel design techniques, achieve improved performance in applications where conventional antennas do not perform well. These are significant contributions to the analysis and development of RFID systems and making them ubiquitous.

REFERENCES

[1] D. Dobkin, *The RF in RFID: Passive UHF RFID in Practice*, Newnes-Elsevier Inc., Burlington, MA, USA, 2008.

[2] K. Michael, J. McCathie, "The pros and cons of RFID in supply chain management," *Proc. Int. Conf. on Mobile Business*, pp. 623-629, 11-13 July 2005, Sydney, Australia.

[3] A. Lehto, J. Nummela, L. Ukkonen, L. Sydänheimo, M. Kivikoski, "Passive UHF RFID in paper industry: challenges, benefits and the application environment," *IEEE Trans. Autom. Sci. Eng.*, vol. 6, no. 1, pp. 66-79, Jan. 2009.

[4] J. Virtanen, L. Ukkonen, T. Björninen, A. Z. Elsherbeni, L. Sydänheimo, "Inkjet printed humidity sensor for passive UHF RFID systems," *IEEE Trans. Instrum. Meas.*, vol. 60, no. 8, pp. 2768-2777, Aug. 2011.

[5] S. S. Saad, Z. S. Nakad, "A standalone RFID indoor positioning system using passive tags," *IEEE Trans. Ind. Electron.*, vol. 58, no. 5, pp. 1961-1970, May 2011.

[6] G. Marrocco, "Pervasive electromagnetics: sensing paradigms by passive RFID technology," *IEEE Wireless Commun.*, vol. 17, no. 6, pp. 10-17, Dec. 2010.

[7] S. Roy, V. Jandhyala, J. R. Smith, D. J. Wetherall, B. P. Otis, R. Chakraborty, M. Buettner, D. J. Yeager, Y.-C. Ko, A. P. Sample, "RFID: from supply chains to sensor nets," *Proc. IEEE*, vol. 98, no. 9, pp. 1583-1592, Sept. 2010.

[8] T. Kellomäki, T. Björninen, L. Ukkonen, L. Sydänheimo, "Shirt collar tag for wearable UHF RFID systems," *Proc. EuCAP Conf.*, 12-16 Apr. 2010, Barcelona, Catalonia, Spain.

[9] J. M. Rabaey, M. Mark, D. Chen, C. Sutardja, C. Tang, S. Gowda, M. Wagner, D. Werthimer, "Powering and communicating with mm-size implants," *Proc. DATE Conf.*, pp. 1-6, 14-18 Mar. 2011, Grenoble, France.

[10] Z. Xiao, C.-M. Tang, C. M. Dougherty, R. Bashirullah, "A 20μW neural recording tag with supply-current-modulated AFE in 0.13μm CMOS," *Proc. IEEE ISSCC*, pp.122-123, 7-11 Feb. 2010, San Francisco, CA, USA.

[11] V. Subramanian, J. M. J. Frechet, P. C. Chang, D. C. Huang, J. B. Lee, S. E. Molesa, A. R. Murphy, D. R. Redinger, S. K. Volkman, "Progress toward development of all-printed RFID tags: materials, processes, and devices," *Proc. IEEE*, vol. 93, no. 7, 1330-1338, July 2005.

[12] P. R. Foster, R. A. Burberry, "Antenna problems in RFID systems," *IEE Colloquium on RFID Technology*, 3/1-3/5, Oct. 25 1999, London, UK.

[13] J. D. Griffin, G. D. Durgin, A. Haldi, B. Kippelen, "RF tag antenna performance on various materials using radio link budgets," *IEEE Antennas Wireless Propag. Lett.*, vol. 5, no. 1, pp. 247-250, Dec. 2006.

[14] S. R. Aroor, D. D. Deavours “Evaluation of the state of passive UHF RFID: an experimental approach,” *IEEE Syst. J.*, vol. 1, no. 2, pp. 168-176, Dec. 2007.

[15] International Organization for Standardization, ISO/IEC 18000-6, www.iso.org/

[16] EPCglobal, Overview of the ultra high frequency (UHF) regulations worldwide: http://www.gs1.org/epcglobal/implementation

[17] J. C. Rautio, ”Twenty three years: the acceptance of Maxwell’s equations,” *J. Appl. Computational Electromagn. Soc.*, vol. 25, no. 12, pp. 998-1006, Dec. 2010.

[18] J. Rashed, C.-T Tai, ”A new class of resonant antennas,” *IEEE Trans. Antennas Propag.*, vol. 39, pp. 1428-1430, Sep. 1991.

[19] S. R. Best, J. D. Morrow, ”On the significance of current vector alignment in establishing the resonant frequency of small space-filling wire antennas, ” *IEEE Antennas Wireless Propag. Lett.*, vol. 2, pp. 201-204, 2003.

[20] A. Harmouch, H. A. Al Sheikh, ”Miniaturization of the folded-dipole antenna,” *IEEE Antennas Propag. Mag.*, vol. 51, no. 1, pp. 117-123, Feb. 2009.

[21] G. Marrocco, ”The art of UHF RFID antenna design: impedance-matching and size-reduction techniques,” *IEEE Antennas Propag. Mag.*, vol. 50, no. 1, pp. 66-79, Feb. 2008.

[22] R. C. Hansen, *Electrically Small, Superdirective, and Superconducting Antennas*, John Wiley & Sons, Inc., Hoboken, NJ, 2006.

[23] J. L. Volakis, C.-C. Chen, K. Fujimoto, *Small Antennas: Miniaturization Techniques & Applications*, McGraw-Hill, New York, NY, USA, 2010.

[24] L. J. Chu, “Physical limitations of omni-directional antennas,” *J. Appl. Phys*, vol. 19, no. 12, pp. 1163-1175, Dec. 1948.

[25] M. Gustafsson, C. Sohl, G. Kristensson, “Physical limitations on antennas of arbitrary shape,” *Proc. R. Soc. A*, vol. 463 no. 2086, pp. 2589-2607, July 2007.

[26] A. Blayo, B. Pineaux, “Printing processes and their potential for RFID printing, “*Proc. Joint sOc- EUSAI Conf.*, pp. 27–30, 12-14 Oct. 2005, Grenoble, France.

[27] M. Pudas, N. Halonen, P. Granat, J. Vähäkangas, “Gravure printing of conductive particulate polymer inks on flexible substrates,” *Prog. Organic Coat.*, vol. 54, no. 4, pp. 310-316, Dec. 2005.

[28] I. Löcher, G. Tröster, “Screen-printed textile transmission lines,” *Textile Res. J.*, vol. 77, no. 11, pp. 837-842, 2007.

[29] S. Merilampi, T. Laine-Ma, P. Ruuskanen, “The characterization of electrically conductive silver ink patterns on flexible substrates,” *Mircoelectron. Reliab.*, vol. 49, no. 7, pp. 782-790, July 2009.

[30] V. Palukuru, K. Sonoda, V. Pynttäri, T. Hu, R. Mäkinen, M. Mäntysalo, J. Hagberg, H. Jantunen, “Inkjet-printed RF structures on BST-polymer composites; an

application of a monopole antenna for 2.4 GHz WLAN operation," *Intl. J. Appl. Ceramic Tech.*, vol. 8, no. 4, pp. 940-946, May 2010.

[31] J. Virtanen, T. Björninen, L. Ukkonen, L. Sydänheimo, "Passive inkjet-printed narrow-line RFID tags," *IEEE Antennas Wireless Propag. Lett.*, vol. 9, no. 1, pp. 440-443, Dec 2010.

[32] S. Merilampi, T. Björninen, L. Ukkonen, P. Ruuskanen, L. Sydänheimo "Characterization of UHF RFID tags fabricated directly on convex surfaces by pad printing," *Int. J. Adv. Manuf. Tech.*, vol. 53, no. 5, pp. 577-591, Mar. 2011.

[33] K. Woo, Y. Kim, B. Lee, J. Kim, J. Moon "Effect of carboxylic acid on sintering of inkjet-printed copper nanoparticulate films," *ACS Appl. Mater. Interfaces*, vol. 3, no. 7, pp. 2377-2382, May 2011.

[34] Y. C. Or, K. W. Leung, R. Mittra, K. V. S. Rao, "Analysis on the platform-tolerant radio-frequency identification tag antenna," *IET Microw. Antennas Propag.*, vol. 3, no. 4, pp. 601-606, June 2009.

[35] X. Jingtian, Z. Hailong Zhu, T. T. Ye, "Platform-tolerant PIFA-type UHF RFID tag antenna," *Proc. IEEE Int. Conf. on RFID*, pp.174-180, 14-16, Apr. 2010, Orlando, FL, USA.

[36] H. Rajagopalan, Y. Rahmat-Samii, "Platform tolerant and conformal RFID tag antenna: design, construction and measurements," *J. Appl. Computational Electromagn. Soc.*, vol. 25, no. 6, June 2010.

[37] J. H. Deng, W. S. Chan, B.-Z. Wang, S. Y. Zheng, K. F. Man, "An RFID multicriteria coarse- and fine-space tag antenna design," *IEEE Trans. Ind. Electron.*, vol. 58, no. 6, pp. 2522-2530, June 2011.

[38] L. Yang, L. J. Martin, D. Staiculescu, C. P. Wong, M. M. Tentzeris, "Conformal magnetic composite RFID for wearable RF and bio-monitoring applications," *IEEE Trans. Microw. Theory Tech.*, vol. 56, no. 12, pp. 3223-3230, Dec. 2008.

[39] X. Qing, C. K. Goh, Z. N. Chen, "Impedance characterization of RFID tag antennas and application in tag co-design," *IEEE Trans. Mircrow. Theory Tech.*, vol. 57, no. 5, pp. 1268-1274, May 2009.

[40] S. R. Elliot, *Antenna Theory and Design*, An IEEE Classical Reissue, John Wiley & Sons, Inc., Hoboken, New Jersey, 2003.

[41] W. L. Stutzman, G. A. Thiele, *Antenna Theory and Design*, 2nd Ed., John Wiley & Sons, Inc., Hoboken, New Jersey, 1998.

[42] C. A. Balanis, *Advanced Engineering Electromagnetics*, John Wiley & Sons, Inc., Hoboken, New Jersey, 1989.

[43] P. Raumonen, L. Sydänheimo, L. Ukkonen, M. Keskilammi, M. Kivikoski, "Folded dipole antenna near metal plate," *Proc. IEEE AP-S Int. Symp.*, pp. 848-851, June 22-27 2003, Columbus, OH, USA.

[44] L. Ukkonen, L. Sydänheimo, M. Kivikoski , ”Effects of metallic plate size on the performance of microstrip patch-type tag antennas for passive RFID,” *IEEE Antennas Wireless Propag. Lett.*, vol. 4, pp. 410-413, Dec. 2005.

[45] M. Hirvonen, K. Jaakkola, P. Pursula, J. Säily, ”Dual-band platform tolerant antennas for radio-frequency identification,” *IEEE Trans. Antennas Propag.*, vol. 54, no. 9, pp. 2632-2637, Sept. 2006.

[46] S.-L. Chen, R. Mittra, “Long read range RFID tag design for metallic objects,” *Proc. EuCAP Conf.*, 12-16 Apr. 2010, Barcelona, Spain.

[47] H.-D. Chen, Y.-H. Tsao, C.-Y. Kuo, “Low-profile radio frequency identification tag antenna using a trapezoid patch mountable on metallic surfaces,” *Microw. Optical Tech. Lett.*, vol. 52, no. 8, pp. 1697-1700, Aug. 2010.

[48] J. Z. Huang, P. H. Yang, W. C. Chew, T. T. Ye, “A novel broadband patch antenna for universal UHF RFID tags,” *Microw. Optical Tech. Lett.*, vol. 52, no. 12, pp. 2653-2657, Dec. 2010.

[49] Y. Park, J. N. Lee, J. K. Park, “Design of UHF radio frequency identification metal tag antenna using T-shaped slot,” *Microw. Optical Tech. Lett.*, vol. 53, no. 10, pp. 2251-2255, Oct. 2011.

[50] S.-L. Chen, K. H. Lin, “A slim RFID tag antenna design for metallic object applications,” *IEEE Antennas Wireless Propag. Lett.*, vol. 7, no. 1, pp. 729-732, Dec. 2008.

[51] S.-L. Chen, “A miniature RFID tag antenna design for metallic objects application,” *IEEE Antennas Wireless Propag. Lett.*, vol. 8, no. 1, pp. 1043-1045, Dec. 2009.

[52] T. V. Koskinen, H. Rajagopalan, Y. Rahmat-Samii, “A thin multi-slotted dual patch UHF-band metal-mountable RFID tag antenna,” *Microw. Optical Tech. Lett.*, vol. 53, no. 1, Oct. 2011.

[53] P. H. Yang, Y. Li, L. Jiang, W. C. Chew, T. T. Ye, “Compact metallic RFID tag antennas with a loop-fed method,” *IEEE Trans. Antennas Propag.*, vol. 59, no. 12, pp. 4454-4462, Dec. 2011.

[54] J. Dacuna, R. Pous, “Low-profile patch antenna for RF identification applications,” *IEEE Trans. Microw. Theory Tech.*, vol. 57, no. 5, pp. 1406-1410, May 2009.

[55] S.-K. Kuo, L.-G. Liao “An analytic model for impedance calculation of an RFID metal tag,” *IEEE Antennas Wireless Propag. Lett.*, vol. 9, pp. 603-607, Dec. 2010.

[56] J. D. Jackson, *Classical Electrodynamics*, 3rd Ed., John Wiley & Sons, Inc., Hoboken, New Jersey, 1999.

[57] S. Merilampi, T. Björninen, A. Vuorimäki, L. Ukkonen, P. Ruuskanen, L. Sydänheimo, “The effect of conductive ink layer thickness on the functioning of printed UHF RFID antennas,” *Proc. IEEE*, vol. 98, no. 9, pp. 1610-1619, Sept. 2010.

[58] W. F. Richards, “Microstrip Antennas,” in *Antenna Hand Book Vol. II: Antenna Theory* [Edited by Y. T. Lo and S. W. Lee], Van Nostrand Reinhold, New York, NY, 1993.

[59] H. Stockman, ”Communication by means of reflected power,” *Proc. IRE*, vol. 36, no. 10, pp. 1196-1204, Oct. 1948.

[60] A. R. Koelle, S. W. Depp, R. W. Freyman, ”Short-range radio-telemetry for electronic identification, using modulated RF backscatter,” *Proc. IEEE*, vol. 63, no. 8, pp. 1260-1261, Aug. 1975.

[61] J. Landt, ”The history of RFID,” *IEEE Potentials*, vol. 24, no. 4, pp. 8-11, Oct.-Nov. 2005.

[62] U. Karthaus, M. Fischer, ”Fully integrated passive UHF RFID transponder IC with 16.7-μW minimum RF input power,” *IEEE J. Solid-State Circuits*, vol. 38, no. 10, pp. 1602-1608, Oct. 2003.

[63] NXP Semiconductors, Eindhoven, Netherlands. UCODE G2iL(+) series tag ICs: http://www.nxp.com/products/identification_and_security/smart_label_and_tag_ics/ucode/

[64] Impinj, Inc., Seattle, WA, USA. Monza series tag ICs: http://www.impinj.com/support/downloadable_documents.aspx

[65] Alien Technology, Morgan Hill, CA, USA. Higgs series tag ICs: http://www.alientechnology.com/tags/rfid_ic.php

[66] J. P. Curty, N. Joehl, C. Dehollain, M. J. Declercq, “Remotely powered addressable UHF RFID integrated system,” *IEEE J. Solid-State Circuits*, vol. 40, no. 11, pp. 2193-2202, Nov. 2005.

[67] S. Mandal, R. Sarpeshkar, “Low-power CMOS rectifier design for RFID applications,” *IEEE Trans. Circuits Syst. I, Reg. Papers*, vol. 54, no. 6, pp. 1177-1188, June 2007.

[68] G. De Vita, G. Iannaccone, ”Design criteria for the RF section of UHF and microwave passive RFID transponders,” *IEEE Trans. Microw. Theory Tech.*, vol. 53, no. 9, pp. 2978-2990, Sept. 2005.

[69] C.-H. Loo, K. Elmahgoub, F. Yang, A. Z. Elsherbeni, D. Kajfez, A. A. Kishk, T. Elsherbeni, L. Ukkonen, L. Sydänheimo, M. Kivikoski, S. Merilampi, P. Ruuskanen, “Chip impedance matching for UHF RFID tag antenna design,” *Prog. Electromagn. Res.*, vol. PIER 81, pp. 359-370, 2008.

[70] P. V. Nikitin, K. V. S. Rao, R. Martinez, S. F. Lam, “Sensitivity and impedance measurements of UHF RFID chips,” *IEEE Trans. Microw. Theory Tech.*, vol. 57, no. 5, pp. 1297-1302, May 2009.

[71] L. W. Mayer, A. L. Scholtz, "Sensitivity and impedance measurements on UHF RFID transponder chips," *2nd Int. EURASIP Workshop on RFID Technology*, 7-8 July 2008, Budapest, Hungary.

[72] H.-W. Son, C.-S. Pyo, "Design of RFID tag antennas using an inductively coupled feed," *Electronics Letters*, vol. 41, no. 18, pp. 994-996, Sept. 2005.

[73] Y. Zhou, Z. Zhong, Y. Hong, "An effective fast matching oriented slot antenna designing method with RFID tag chip," *Proc. IEEE MAPE Int. Symp.*, pp.575-578, 16-17 Aug. 2007, Hangzhou, China.

[74] T. Björninen, L. Ukkonen, L. Sydänheimo, "Design and non-invasive design verification of a slot-type passive UHF RFID tag," *Proc. IEEE RWS.*, pp.132-135, 10-14 Jan. 2010, New Orleans, MS, USA.

[75] X. Jingtian, T. T. Ye, "Wideband and material-insensitive RFID tag antenna design utilizing double-tuning technique," *Proc. IEEE AP-S Int. Symp.*, pp.545-548, 3-8 July 2011, Spokane, WA, USA.

[76] K. Koski, E. Koski, L. Ukkonen, L. Sydänheimo, T. Björninen, J. Virtanen, A. Z. Elsherbeni, "Effects of laboratory-scale IC attachment methods on passive UHF RFID tag performance," *Proc. IEEE AP-S Int. Symp.*, pp.1004-1007, 3-8 July 2011, Spokane, WA, USA.

[77] P. Y. Ufimtsev, "Comments on diffraction principles and limitations of RCS reduction techniques," *Proc. IEEE*, vol. 84, no. 12, pp. 1830-1851, Dec 1996.

[78] R. C. Hansen, "Relationships between antennas as scatterers and as radiators," *Proc. IEEE*, vol. 77, no. 5, pp. 659-662, May 1989.

[79] K. Kurokawa, "Power waves and the scattering matrix," *IEEE Trans. Microw. Theory Tech.*, vol. 13, no. 2, pp. 194-202, Mar. 1965.

[80] R. E. Collin, "Limitations of the Thévenin and Norton equivalent circuits for a receiving antenna," *IEEE Antennas Propag. Mag.* vol. 45, no. 2, pp. 119-123, Apr. 2003.

[81] P. Pursula, T. Vähä-Heikkilä, A. Müller, D. Neculoiu, G. Konstantinidis, A. Oja, J. Tuovinen, "Millimeter-wave identification—a new short-range radio system for low-power high data-rate applications," *IEEE Trans. Microw. Theory Tech.*, vol. 56, no. 10, pp. 2221-2228, Oct. 2008.

[82] P. V. Nikitin, K. V. S. Rao, "Antennas and propagation in UHF RFID systems," *Proc. IEEE RFID Int. Conf.*, pp. 277-288, 16-17 April 2008, Las Vegas, NV, USA.

[83] G. Marrocco, E. Di Giampaolo, R. Aliberti, "Estimation of UHF RFID reading regions in real environments," *IEEE Antennas Propag. Mag.*, vol. 51, no. 6, pp. 44-57, 2009.

[84] H. T. Friis, "A note on a simple transmission formula," *Proc. IRE*, vol. 34, no. 5, pp. 254-256, May 1946.

[85] C. Icheln, J. Krogenius, P. Vainikainen, "Use of balun chokes in small-antenna Radiation Measurements," *IEEE Trans. Instrum. Meas.*, vol. 53, no. 2, Apr. 2004.

[86] P. Pursula, D. Sandström, K. Jaakkola, "Backscattering-based measurement of reactive antenna input impedance," *IEEE Trans. Antennas Propag.*, vol. 56, no. 2, pp. 469-474, Feb. 2008.

[87] J. Zhang, S. Pivnenko, O. Breinbjerg, "A cable-free impedance and gain measurement technique for electrically small antennas," *Proc. AMTA Symp.*, pp. 195-201, 10-15 Oct. 2010, Atlanta, GA, USA.

[88] S. Bories, G. Le Fur, L. Cannavo, C. Lach, C. Delaveaud, "Non-invasive radiation pattern measurement of electrically small antenna using fiber optic link," *Proc. AMTA Symp.*, pp. 435-440, 16-21 Oct. 2011, Englewood, CO, USA.

[89] Voyantic, Ltd., Espoo, Finland: http://www.voyantic.com/

[90] ANSYS, Inc., Canonsburg, PA, USA: http://www.ansys.com/

[91] A. R. Djordjevic, R. M. Biljie, V. D. Likar-Smiljanic, T. K. Sarkar, "Wideband frequency-domain characterization of FR-4 and time-domain causality," *IEEE Trans. Electromagn. Compat.*, vol. 43, no. 4, pp. 662–667, Apr. 2001.

[92] G. Gonzales, *Microwave Transistor Amplifiers: Analysis and Design*, Prentice Hall, Inc., Englewood Cliffs, NJ, USA, 1984.

[93] J. Rahola, J. Ollikainen, "Removing the effect of antenna matching in isolation analyses using the concept of electromagnetic isolation," *Proc. IEEE Int. Workshop on Antenna Technology: Small Antennas and Novel Metamaterials*, pp. 554-557, 4-6 Mar. 2008, Chiba, Japan.

[94] Agilent Technologies, Inc., Santa Clara, CA, USA: www.agilent.com/find/eesof-info

[95] Agilent Technologies, Inc., Santa Clara, CA, USA: *Agilent Impedance Measurement Handbook. A Guide to Measurement Technology and Techniques.* 4th Ed., June 2009.

[96] A. Z. Elsherbeni, V. Demir, *The Finite Difference Time Domain Method for Electromagnetics: With MATLAB Simulations*, SciTech Publishing, 2009.

[97] W. J. Ellison, K. Lamkaouchi, J.-M. Moreau, "Water: a dielectric reference," *J. Mol. Liq.*, vol. 68, no. 2-3, pp. 171-279, Apr. 1996.

[98] S. Koulouridis, G. Kiziltas, Y. Zhou, D. J. Hansford, J. L. Volakis, "Polymer-ceramic composites for microwave applications: fabrication and performance assessment," *IEEE Trans. Microw. Theory Tech.*, vol. 54, no. 12, Dec. 2006.

[99] S.-H. Jeong, H.-W. Son, "UHF RFID tag antenna for embedded use in a concrete floor," *IEEE Antennas Wireless Propag. Lett.*, vol. 10, no. 1, pp.1158-1161, Dec. 2011.

[100] L. Josefsson, P. Persson, *Conformal Array Antenna Theory and Design*, IEEE Press, Piscataway, NJ, USA, 2006.

[101] W. M. Middleton, *Reference Data for Engineers: Radio, Electronics, Computer, and Communications*, Newnes-Butterworth-Heinemann, Woburn, MA, USA, 2002.

[102] A. J. Moulson, J. M. Herbert, *Electroceramics: Materials, Properties, Applications*, 2nd Ed., John Wiley & Sons, Ltd., Chichester, West Sussex, UK, 2003.

Publication I

T. Björninen, S. Merilampi, L. Ukkonen, P. Ruuskanen, L. Sydänheimo, “Performance comparison of silver ink and copper conductors for microwave applications,” *IET Microw. Antennas Propag.*, vol. 4, no. 9, pp. 1224-1231, Sept. 2010.

Performance Comparison of Silver Ink and Copper Conductors for Microwave Applications

Toni Björninen[1], Sari Merilampi[2], Leena Ukkonen[1], Pekka Ruuskanen[2], Lauri Sydänheimo[1]

1. Tampere University of Technology, Institute of Electronics, Rauma Research Unit, Kalliokatu 2, 26100 Rauma, Finland

2. Tampere University of Technology, Pori, Electronics, Pohjoisranta 11 A, 28100 Pori, Finland

Abstract

In this paper copper and silver ink microstrip lines (MSL) are simulated, measured and compared. Implementation and performance of a coupled-line coupler using printed microstrip lines was investigated. At microwave frequencies it is important to consider conductor losses, especially in thin conducting structures. The effect of the conductivity of the conductor material, substrate losses and the effect of protective coating were also investigated. The results showed that despite the lower conductivity of the silver ink compared to copper, the screen printed lines that we studied are still applicable to microwave applications.

1 Introduction

RF-applications utilizing printed electronics as a manufacturing method have recently become high profile technologies. Printing is an environmentally friendly process since the conductors are printed only on the areas that need to be conductive. This means that fewer different chemicals are needed in the manufacturing process and less waste is produced. In addition, printing is possible on a wide variety of materials, which enables integration of printed electronics directly onto challenging non-planar surfaces, such as clothes or paper reels. Printing also allows mass production, and thus provides one possible manufacturing method for future PCBs.

Different printing techniques are available for printing conductive patterns. Screen printing, gravure printing, lithography, flexography and inkjet printing are examples of these techniques [1],[2],[3] [4],[5],[6],[6],[7]. They have been used to manufacture products such as RFID transponder antennas in [9],[10],[11] and [12], transmission lines in [12] and [14] and patch antennas for microwave applications in [15] and [16].

The above-mentioned printing technologies use conductive inks. In general these inks have lower conductivity than pure metals, such as copper or aluminium. The conductive inks consist mainly of inorganic particles (as conductive phase), binder material (insulator phase), solvents and additives. The composition and conductivity of the ink varies according to printing technique. Silver flakes, for example, are a commonly used filler material in screen printable inks. Typical conductivity for this kind of ink is a few mega siemens per metre. In the inkjet technique materials such as gold nanoparticles can be used as filler. In [17] the conductivity of gold nanocrystal ink is reported to be 10-30 MS/m.

In addition to the conductor material, the composition and the amount of ink have a crucial effect on the realized conductivity of the printed conductor. The particles (material, size, amount, shape, distribution and orientation) influence the electrical and mechanical properties of printed conductors. Further, the viscosity of the ink affects the way it is transferred onto the substrate. In the case where the substrate surface is rough compared to the desired ink layer thickness, the current paths will elongate and variations in the deposited conductive layer thickness will occur, resulting in increased resistance. The curing temperature of the ink is an important parameter as well. [1]

The lower the conductivity, the thicker (ink) the layer needed to minimize the losses in RF-circuits, since at high frequencies the skin effect begins to decrease the effective conductivity of the ink. Therefore, in practical applications, it is important to ensure that the performance of the conductors is satisfactory throughout the desired frequency range, regardless of the fabrication method. [1],[17],[18]

In transmission lines, couplers, circulators and passive RF-devices in general, the conductivity of the ink is related to the insertion loss, i.e. the power loss due to the line structure. In antenna applications radiation efficiency can be greatly affected by the conductivity [9]. In article [19] the insertion loss of inkjet-printed transmission lines were investigated up to 5 GHz and the authors found them to be low enough for many applications.

Nowadays microstrip line (MSL) and co-planar waveguide (CPW) are the most widely used transmission line structures in RF-circuits. Both structures allow fabrication by different printing methods and possess good miniaturization capabilities and each has its own application-specific advantages. Common to these structures is that they allow the signal to be transferred as a quasi-TEM wave partially inside a dielectric material. The signal conductor is placed on top of the dielectric, which is therefore referred to as the substrate. In MSL a conducting plane is placed beneath the substrate and in CPW, conducting planes are placed on both sides of the signal conductor on the substrate. Part of the electromagnetic fields of these transmission lines exists inside the substrate and, therefore, in addition to the conductor material, the electrical properties of the substrate have a bearing on signal propagation. [20],[21]

Together with the geometry of the transmission line structure, the electrical properties of the substrate determine the characteristic impedance of the line. In article [22] H. A. Wheeler derived approximate formulae, which link these features together. The formulation can be used to select the desired width-to-thickness ratio or characteristic impedance of the MLS when either one of the related quantities is fixed. Design of CPW is, however, less straightforward and is discussed in more detail, e.g. in [21]. A printed CPW is discussed, e.g. in [3], where the inkjet technique is used to fabricate CPW with copper ground plane, and the performance properties of the line are investigated.

A wireless sensor module was fabricated using the inkjet technique in [23]. Fabrication of other passive transmission line devices, such as a filter, circulator, and coupler are studied in [14],[23] and [25]. The results indicate that the performance of the lithographically printed microstrips is reasonable. In the early development of printed microwave conductive lithographic films (CLF), the conductor was first printed on a paper and the paper was attached to a secondary substrate. Copper ground plane was on the other side of the secondary substrate [14]. In [14] a flexible and fully printed microstrip line was fabricated. The substrate of the flexible microstrip was plated polymer substrate. As the authors of [14] observed, the printing of the ground plane increases losses.

The application examples mentioned above prompted us to manufacture fully printed MSL and a coupled-line coupler by screen printing in order to study the feasibility and performance of these structures compared to traditional copper-etched devices. No secondary substrate, copper ground plane or plating of the substrate or electro deposit plating on printed patterns were used since we wished to eliminate the effect of these on the performance of the devices. This enabled us to perform a fair comparison between the printed and etched devices.

In industrial manufacturing PCBs are typically plated with protective coating and in the case of copper PCBs, with a solder mask. The effect of the solder mask on the performance of microwave electronics is also investigated in this article.

The paper is structured as follows: geometry, materials and fabrication methods of the samples are introduced in section 2. Section 3 presents the simulation methods and measurement setup for this study. The simulations and measurement results are introduced and discussed in section 4. The conclusions and future work are presented in Section 5.

2 Experiment arrangements

The printed microstrip lines and coupled-line couplers were manufactured by the screen printing method and by etching. In screen printing the conductive ink is pressed through a screen onto the substrate with a squeegee [26]. The characteristics of the ink used are presented in Table 1. The ground planes were first printed on one side of the substrate and cured in accordance with the manufacturers' recommendations (Table 1).The conductors were then printed on the other side of the substrate and cured under the recommended conditions. Ferricloride was used as an etchant and 1.5 mm thick FR-4 was used as the substrate for both printed and etched samples.

Table 1: Characteristics of screen printable ink.

Manufacturer's description	Curing conditions (°C, min)	Viscosity (P)	Conductivity (MS/m)
Single component silver ink consisting of polyester resin, silver flakes, solvent and additives. Silver content is 60 - 65 wt% and polyester resin content is	120, 20	200 - 300	1,25

11-14 wt%. Particle size is mainly in a range from 3 to 15µm.			

Commercial solder mask was printed on the etched samples by screen printing. According to the manufacturer, the dielectric constant of the solder mask is between 3.4 and 3.6 at 1GHz and loss tangent can vary from 0.01 to 0.03. The samples were first plated with the solder mask on one side and the mask was pre-dried in an oven. This procedure was repeated on the other side of the board and the samples were exposed to UV light, developed and cured. SMA-connectors were attached to the printed samples by conductive epoxy and by soldering to the etched samples.

Figure 1: Fabricated lines and couplers.

2.1 Microstrip lines

All fabricated test lines are 10 cm long. Conductor thickness in the etched lines is 35 µm, whereas the nominal thickness for the screen printed line was set to 20 µm and this value was used to select the geometry for the printed design. The thickness achieved was then measured and used to produce the simulation results for comparison with the measurement results. Ground plane size for the fabricated lines is 10 cm x 10 cm.

In the initial studies, a dielectric constant of 4.5 and a loss tangent of 0.02 were used to model the FR-4 substrate. Calculation using the formulation in [22] suggested that 3.0 mm line width would provide 50-Ω characteristic impedance for the microstrip lines. This was verified by Ansoft's High Frequency Structure Simulator (HFSS) which also suggested that the same line width would be suitable for both screen printed and etched lines.

2.2 Coupled-line coupler

As an application of the screen printed MSLs, we considered a coupled-line coupler since it is a common example of a 4-port passive microwave circuit.

The same design is proposed for both conductor materials. The design process was carried out using Agilent ADS RF-circuit simulator and the results were verified with HFSS. Centre frequency for the design is 2.45 GHz and the specified value for the coupling is –20 dB. Conductor thicknesses and substrate are the same as in the previously discussed MSLs and the coupler is intended for 50-Ω system impedance. Geometry of the design is shown in Fig. 2 and the key-dimensions are presented in Table 2.

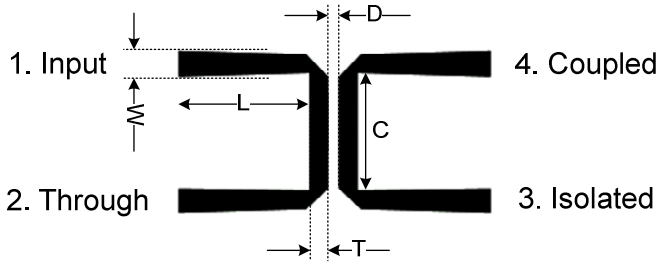

Figure 2: Geometry and key dimensions of the coupler design.

Table 2: Key dimensions of the coupler design.

W	L	T	C	L
3.8mm	19.8mm	3.0mm	17.5mm	1.6mm

3 Simulations and Measurements

The thickness of the solder mask and silver ink layers were measured using software connected to an optical microscope. The measurement was performed at 20 different points on the cross-sections of the samples. Figure 3 shows the location of the measurement cross-section. The thickness of the silver ink layer was assumed to be the same for the printed couplers and MSLs since the manufacturing parameters and materials are the same. The ink layer thickness and conductivity parameter are taken into account in our HFSS and ADS simulations. As might be expected, a finer mesh is introduced in these simulations to predict the correct response from the coupler.

Figure 3: Arrow indicates the location of cross-section for the thickness measurement.

3.1 Microstrip lines

Performance of a MSL can be evaluated by its insertion loss per unit length; in our study, dB/cm. In the absence of coupling and discontinuities in the line, which would result in additional radiation loss, insertion loss is strictly due to dielectric and conductor losses [28]. Approximate formulation for these can be found, e.g. in [27], though in this study we investigate only the losses by simulation software packages and measurements.

In many practical designs, such as the coupled line coupler we investigate, the permittivity and loss tangent of the FR-4 substrate can be modeled as constants over a wide band of frequencies [29]. However to study the insertion loss of the fabricated transmission lines accurately, it may suffice to use only a constant approximation for the loss tangent.

Our study is confined to frequencies from 50 MHz to 5 GHz. Simulations were conducted with constant approximations $\tan(\delta)=0.02$ and $\tan(\delta)=0.025$ and for comparison with an approximation, where $\tan(\delta)=0.016$ at 100 MHz and increases directly proportional to the frequency, to $\tan(\delta)=0.024$ at 5 GHz. This approximate model was created according to the frequency-dependent results for loss tangent of FR-4 in [29]. Insertion loss simulations were conducted with HFSS, where the losses in the thin conducting structure were modeled by solving the fields inside the conductor instead of relying on the surface field approximation. The effect of lowering the conductivity gradually from the nominal value $\sigma_0=1.25$ MS/m down to $\sigma=0.325\sigma_0$ was also studied

in the simulations to model possible imperfections in the fabrications process, which in practice might indicate lower effective conductivity.

HP8722D vector network analyzer (VNA) was used to extract the scattering matrix of the line, and from this data the insertion loss was determined by a "black-box" method that relies solely on the measured S-parameter data.

To calculate the insertion loss from the measured insertion loss, assume that power P_G is fed from the generator. Then power $(1-|\Gamma_{in}|^2)P_G$ is delivered to the input of the line. Some part of the power is lost in the line so that available power for the load is $IL(1-|\Gamma_{in}|^2)P_G$, where IL is the insertion loss of the line. The actual delivered power to the load is then

$$P_L = IL(1-|S_{11}|^2)(1-|S_{22}|^2)P_G.$$

Now, relation

$$|S_{21}|^2 = \frac{P_L}{P_G}$$

together with the previous expression for P_L implies insertion loss

$$IL_{\mathrm{dB}} = -10\log_{10}\frac{|S_{21}|^2}{(1-|S_{11}|^2)(1-|S_{22}|^2)}$$

in decibels, where the minus sign is added to obtain positive values. Insertion loss per unit length can be found from this by scaling the obtained result with the physical line length.

The introduced measurement method makes no assumptions about the transmission line arrangement between the ports. Because of this, it can be used to take into account all the loss sources, such as radiation and coupling to other lines. We also use this method later in our study to find the insertion loss of the coupled-line coupler. The effect of a solder mask was studied by comparing the measurement results from the etched and plated samples with the results from the etched samples without the coating (solder mask).

3.2 Coupler

A more practical approach was taken to the coupler design. The objective here was to investigate by measurement whether the performance of the printed coupler differs significantly from the nominal design for copper. An etched coupler with solder mask layer was also measured for reference. In the simulations only a constant approximation $\tan(\delta)=0.02$ was used for the loss tangent of FR-4 and the dielectric constant was set to 4.5. The simulations were conducted mainly with Agilent's ADS.

With regard to the port numbering in Fig. 2, S_{11} gives the input return loss when other ports are terminated, and S_{41} and S_{31} yield the coupling and isolation, respectively, when other ports are terminated. These parameters were measured with VNA.

4 Results and discussion

The thickness measurement results of the silver ink layer on FR-4 are presented in Table 3. The ink layer is not completely uniform and thickness variations are evident, as can be seen in Fig. 4. An uneven printed layer is not unusual with the screen printing technique and screen printable silver inks (pseudoplastic, relatively high viscosity), even on smooth surfaces.

Table 3. Mean, minimum, maximum and standard deviation of the silver ink on FR4

Mean	Min	Max	Standard deviation
14.6 µm	12.6 µm	17.2 µm	1.3 µm

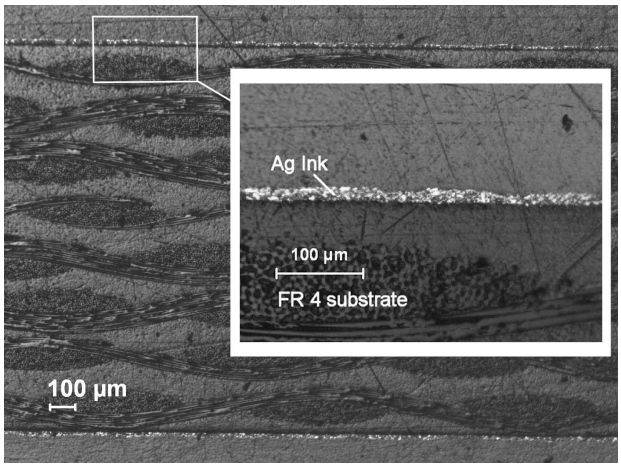

Figure 4: A Cross-section of a printed coupler. No significant difference between the thickness of the silver ink conductor and the silver ink ground plane can be seen.

Mean, minimum, maximum and standard deviation of the solder mask thickness is presented in Table 4. Fig. 5 presents the solder mask on copper conductor.

Table 4: Solder mask thickness.

Mean	Min	Max	Standard deviation
17 µm	16 µm	18 µm	1 µm

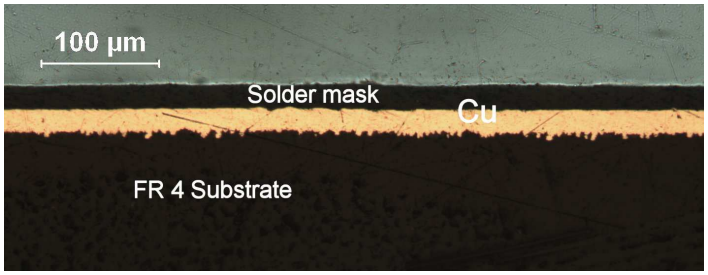

Figure 5. The solder mask on copper conductor.

The solder mask was not studied in the case of the printed samples because its effect on the etched samples was small, as the results below indicate (See Figs. 9 and 11).

4.1 Microstrips

The measured and simulated results for insertion loss of the etched line are presented in Fig. 6 and for screen printed line in Fig. 7. The effect of lowering the conductivity of the silver ink, while using the linear approximation of tan(δ) is illustrated in Fig. 8. The measured insertion losses for all

the fabricated lines are shown in Fig. 9. The thickness of the silver ink layer used in the simulations was set to a measured mean value of 14.6 µm, but the thickness variations in the silver ink layer (see Fig. 4) may lead to a difference between simulated and measured results in the case of the printed samples.

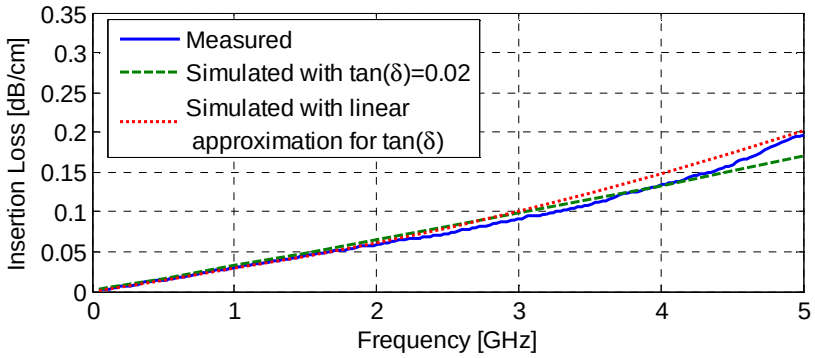

Figure 6: Insertion loss of the etched line.

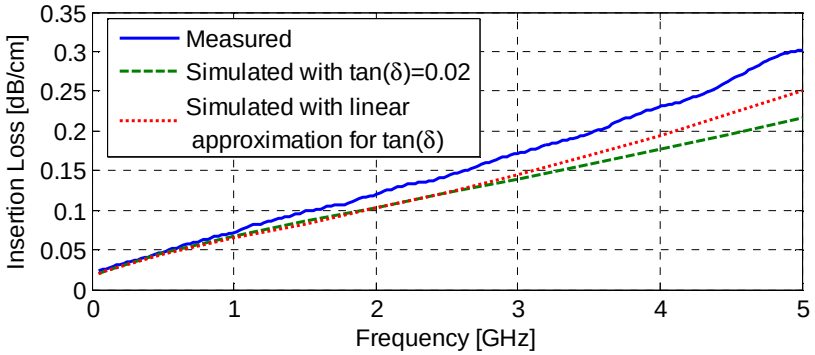

Figure 7: Insertion loss of the screen-printed line.

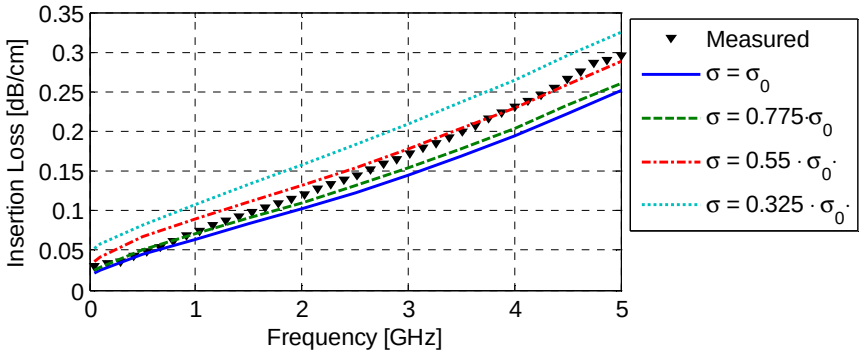

Figure 8: Effect of lower the conductivity of the silver ink.

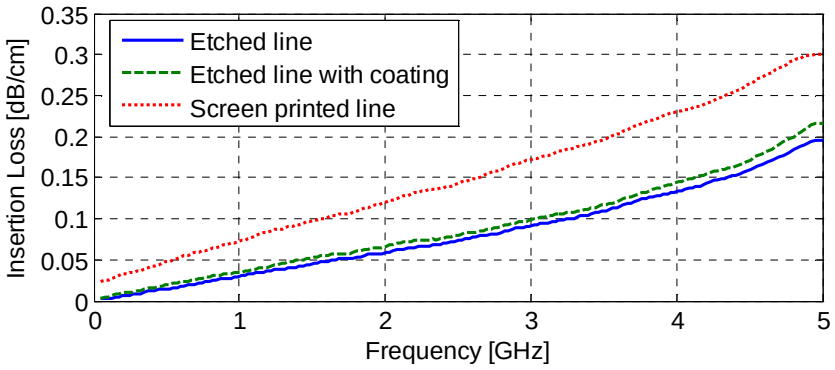

Figure 9: Measured insertion losses of the fabricated lines.

According to the results in Fig. 6, the measurement result for the etched line agrees well with the simulations, although the slightly non-linear behavior in the measurement result remains unpredicted by the simulations. The increase in insertion loss at highest frequencies is not predicted by the constant approximation for loss tangent, but otherwise this approximation seems reasonable. Linear approximation, on the other hand, predicts slightly more loss than was actually measured at frequencies from 3 GHz to 5 GHz, whereas at frequencies below 2 GHz, both approximations correspond closely to the measurement result.

Based on the results presented in Fig. 6, it is concluded that the substrate model in our simulations is sufficiently accurate to study the insertion losses of the lines. It can therefore be concluded from the results in Fig. 7 that there is an additional loss source, which is not included in the simulation model. This additional loss begins to occur after 1 GHz. Possible physical reasons for this include imperfections in fabrication, resulting in lower effective conductivity and non-idealities in the connections to SMA connectors due to the high frequency characteristics of the conductive epoxy.

Since the conductive inks binder, polyester resin, surrounding the silver flakes (i.e. the conductive phase) is also dielectric, it affects the propagation of the signal. The behavior of such material as a function of frequency is not well understood and it might actually be the observed additional loss source. This provides an interesting subject for future studies.

The effect of impaired realized conductivity was further studied by simulation and the results obtained are presented in Fig. 8. It can be seen that the curves closest to the measurement result are the 77.5% and 55% curves. On the basis of this we conclude that the fabricated lines may have 25% lower conductivity than expected. However, even though the 55% curve would fit the measurement data better at high frequencies, we do not expect such a great impairment due to the non-uniform distribution of the silver ink. In addition it can be seen that the 55% and 32.5% curves do not correspond as well with the measurements at lowest frequencies as do the other curves. This also supports the proposition of higher than 77.5% realized conductivity, since the effect of other measurement uncertainties due to parasitic effects is expected to increase with frequency.

For simple comparison, Figure 9 presents the measured insertion losses of all the fabricated lines. Firstly, this figure shows that the effect of the protective coating does not significantly increase the losses of the line. This is to be expected since the coating material has approximately the same loss tangent as the substrate while the thickness of the coating layer is very thin compared to the substrate thickness. Therefore, the contribution of the field distribution within the substrate remains dominant.

Secondly, due to the lower conductivity of the silver ink, the screen printed line has greater insertion loss compared to the etched lines. In our study the insertion loss for the screen printed line

can be 0.1 dB/cm higher than that for the etched line in the studied frequency range. Maximum insertion loss occurs at the highest end of the frequency band and the difference between the results decreases towards the lower end of the band.

4.2 Coupler

Simulated and measured input return loss (S11), coupling (S41) and isolation (S31) of the designed etched and coupler are shown in Fig. 10. Comparisons of the input return loss, coupling and isolation of the etched coupler (nominal design in our study) against the etched coupler with protective coating and screen printed coupler are illustrated in Figs. 11 and 12 respectively. Measured insertion losses from Input- to Through-port of all the fabricated couplers are presented in Fig. 13.

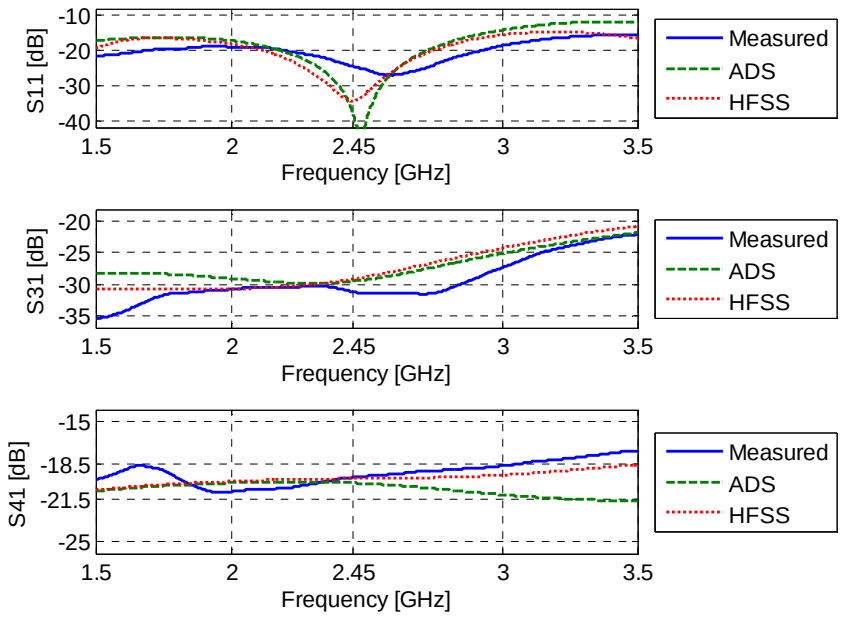

Figure 10: Simulated and measured S-parameters of the etched coupler.

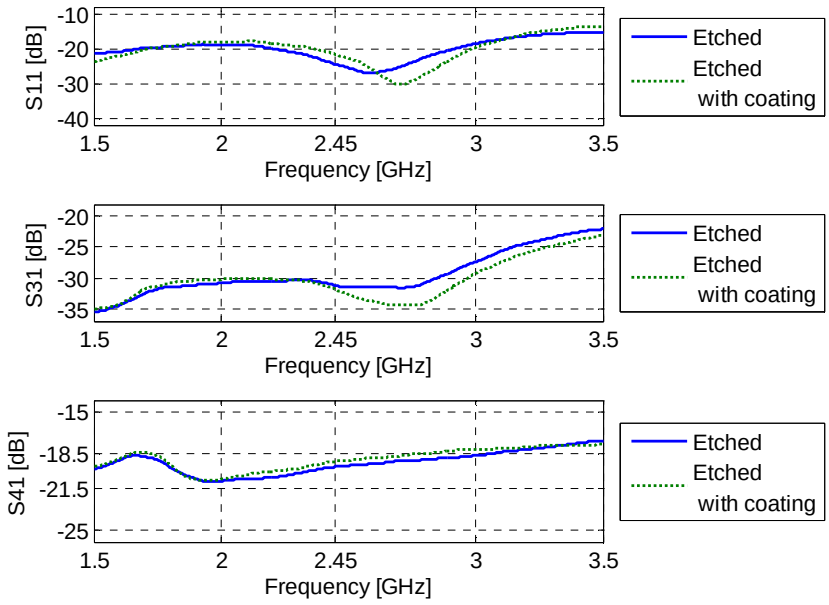

Figure 11: S-parameter comparison between etched coupler and etched coupler with protective coating.

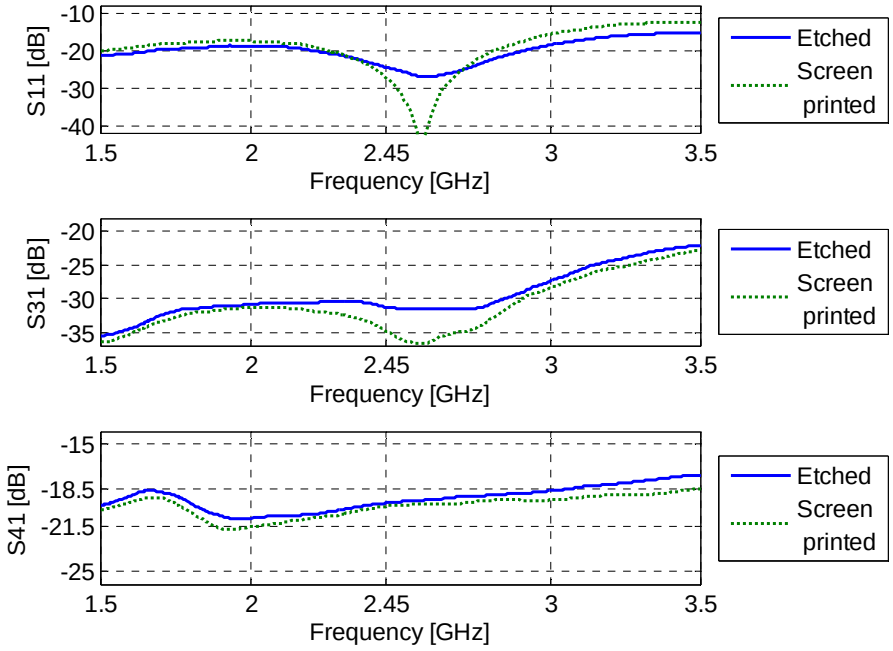

Figure 12: S-parameter comparison between the etched and screen printed couplers.

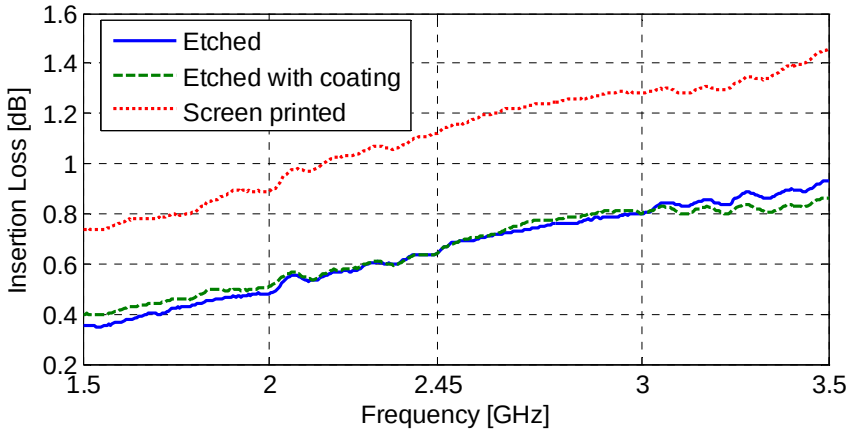

Figure 13: Measured insertion losses of the fabricated couplers.

Simulation results in Fig. 10 predict good matching, specified –20 dB coupling and −29 dB isolation from both copper and screen printed couplers. The measured values in the same figure show that the input matching is best at 2.6 GHz instead of 2.45 GHz, but S11 at the design frequency is still around –25 dB. The measured coupling is very close to –20 dB as predicted and measured isolation is –31 dB, which is some 2 dB better than the simulated value.

Figure 11 illustrates the effect of the protective coating on the operation of the coupler. Best matching is seen to shift upwards, thereby decreasing the S11 at the design frequency to –20 dB; but otherwise the effects are not significant in practice. The coupling, especially, is affected only by less than 0.5 dB when the protective coating is added.

The comparison between the etched coupler and screen printed coupler in Fig. 12 shows a similar result to that in Fig. 11, namely that operation of the printed coupler at the design frequency remains very similar to that of the etched coupler. Coupling is still very close to the specified –20 dB and the matching and isolation at the centre frequency is improved, although notable frequency shifts do not occur.

The greatest difference in operation between the screen printed and etched coupler, which is not seen directly from the S-parameter results, is the insertion loss, which is depicted for all fabricated couplers in Fig. 12. As observed above with the transmission lines, the screen printed lines have greater insertion loss. This is seen again by comparing the insertion losses of the couplers in Fig. 13, where the etched line with and without protective coating shows rather similar performance. However, with the screen printed line the insertion loss on a decibel scale roughly doubles throughout the studied frequency band.

5 Conclusions

Insertion loss of a screen-printed silver ink microstrip line with screen-printed ground plane on a common FR-4 substrate was measured to be less than 0.1 dB/cm higher than that of the etched lines at frequencies up to 5 GHz. This is low enough for many RF-circuit implementations. The effect of a common protective coating was also studied and was found to be negligible.

The fabricated screen printed coupled-line coupler performed well, with a 0.2 dB higher insertion loss in through-path compared to the etched coupler. Excluding the increased insertion loss in the screen-printed version, the performance of the etched and screen-printed devices was found to be almost identical. This indicates that while modelling the losses of printed devices can be challenging, the operation of printed passive RF-circuits can be otherwise predicted accurately with traditional high frequency simulation procedures.

REFERENCES

[1] Merilampi S., Laine-Ma T., and Ruuskanen P.: 'The characterization of electrically conductive silver ink patterns on flexible substrates', Microelectronics reliability, 2009, 7, (49), pp. 782-790

[2] Harrey, P.M.; Evans, P.S.A.; Harrison, D.J.: 'Integrated capacitors for conductive lithographic film circuits', IEEE Transactions on Electronics Packaging Manufacturing, 2001, 24, (4), pp.333-338

[3] Szczech, J.B.; Megaridis, C.M.; Gamota, D.R.; and Zhang J.: 'Fine-line conductor manufacturing using drop-on demand PZT printing technology', IEEE Transactions on Electronics Packaging Manufacturing, 2002, 25, (1), pp.26-33

[4] Shepherd, P.R., Taylor C., Evans, P. S. A., and Harrison D. J.: 'Measurement and Modelling of MIC Components Using Conductive Lithographic Films', Proc. European Microwave Conference, London, England, September 2001, pp. 1-4

[5] Evans, P.S.A, Ramsey, B.J, Harrison, D.J,: 'A comparison of the characteristics of conductive lithographic films and screen printed circuits', Proc. 11th Annual European Passive Components Conference (CARTS-Europe), Prague, Czech Republic, October 1997, pp. 24-28

[6] Evans, P.S.A., Harrey, P.M., Ramsey, B.J., and Harrison, D.J.: 'Lithographic Film Circuits—A Circuit World, Journal of the Printed Circuit Industry Federation, 2001, 27, (3)

[7] Pudas, M., Halonen, N., Granat, P., and Vähäkangas, J.: 'Gravure printing of conductive particulate polymer inks on flexible substrates' Progress in Organic Coatings, 2005, 54, pp 310 – 316

[8] Siden, J., Olsson, T., Fein, M., Koptioug, A., and Nilsson, H-E.: 'Reduced Amount of Conductive Ink with Gridded Printed Antennas' Polytronic 2005. 5th International IEEE Conference on Polymers and Adhesives in Microelectronics and Photonics, Wroclaw , Poland, October 2005, pp. 86-89

[9] Siden, J., Fein, M. K., Koptyug A., and Nilsson, H-E.: 'Printed antennas with variable conductive ink layer thickness', IET Microw. Antennas Propag., 2007, 1, (2), pp. 401–407

[10] Merilampi S., Ukkonen L., Sydänheimo L., Ruuskanen P., and Kivikoski M., 'Analysis of Silver Ink Bow-Tie RFID Tag Antennas Printed on Paper Substrates', International Journal of Antennas and Propagation, Hindawi International Journal of Antennas and Propagation, 2007, Article ID 90762

[11] Costenoble, J.: 'Rotary Screen Printing: The Productive Solution for HF/UHF RFID Labels', SGIA Journal, 2005, fourth quarter, pp. 7-10

[12] Björninen. T., Merilampi S., Ukkonen L., Sydänheimo L., and P. Ruuskanen,: 'The Effect of Fabrication Method on Passive UHF RFID Tag Performance', Hindawi International Journal of Antennas and Propagation, 2009, Article ID 920947

[13] Locher I., Tröster G.: 'Screen-printed Textile Transmission Lines', Textile Research Journal, 2007, 77, (11), pp. 837–842

[14] Evans, P.S.A, Ramsey, B.J, Harrison, D.J., and Shepherd, P.R.: 'Further developments of microwave CLFs', Proc. Automated R.F. and Microwave Measurement Society Conf., Malvern, England, April 1997

[15] Mäntysalo, M, and Mansikkamäki P.: 'An inkjet-deposited antenna for 2.4 GHz applications', International Journal of Electronics and Communications, 2007, 63 1, pp. 31-35

[16] Kirschenmann, K., Whites, K.W., and Woessner, S.M.: 'Inkjet printed microwave frequency multilayer antennas', Proc. IEEE Antennas and Propagation Society International Symposium, Honolulu, Hawai'i, USA, June 2007, pp.924-927

[17] Molesa, S., E.: 'Ultra-Low-cost Printed Electronics', Electrical Engineering and Computer Sciences. Technical Report No. UCB/EECS-2006-55, University of California at Berkeley

[18] R.S. Khandpur: 'Printed Circuit Boards, Design, fabrication and Assembly' (Mc Graw-Hill, 2006)

[19] Radivojevic, Z., Andersson, K., Hashizume, K., Heino, M., Mäntysalo, M., Mansikkamäki, P., Matsuba, Y., and Terada, N.: 'Optimised curing of silver ink jet based printed traces'. 12th International Workshop on THERMal INvestigation of ICs and Systems, Côte d'Azur, France, September 2006, pp. 163-168

[20] Balanis, C.A.: 'Advanced Engineering Electromagnetics', (Wiley, 1989)

[21] Simons, R.N., 'Coplanar Waveguide Circuits, Components, and Systems' (Wiley, 2001)

[22] Wheeler, H.A., 'Transmission-Line Properties of a Strip on a Dielectric Sheet on a Plane', IEEE Transactions on Microwave Theory and Techniques , 1977, 25, (8), pp. 631-647

[23] Vyas, R.J.; Rida, A.; Li Yang; Tentzeris, M.M.: 'Design and development of the first entirely paper-based wireless sensor module' Proc. IEEE Antennas and Propagation Society International Symposium, San Diego, USA, July 2008, pp.1-4, 5-11

[24] Evans, P.S.A., Ramsey, B.J., Harrey, P.M. and Harrison, D.J.: 'Printed analogue filter systems', IEE Electronics Lttrs, 1999, 35 (4), pp. 306-8

[25] Evans, P.S.A., Harrey, P.M., Ramsey, B.J. and Harrison, D.J.: 'R.F. circulator structures via offset lithography', IEE Electronics Lttrs, 1999, 35 (19), pp. 1634-6

[26] Landers, T. L., Brown, D. B., Fant, E. W., Malstrom, E. M., and Schmitt, N. M.: 'Electronics Manufacturing Processes', (Prentice Hall, 1994)

[27] CT-33 Costa L. and Valtonen M.: 'Implementation of Single and Coupled Microstrip Lines in APLAC', October 1997. Helsinki University of Technology. Circuit Theory Laboratory Report CT-33, December 1997.

[28] Denlinger, E.J.: 'Losses of Microstrip Lines', IEEE Transactions on Microwave Theory and Techniques, 1980, 28, (6), pp. 513-522

[29] Djordjevic, A.R., Biljie, R.M., Likar-Smiljanic, V.D., and Sarkar, T.K.: 'Wideband frequency-domain characterization of FR-4 and time-domain causality,' IEEE Transactions on Electromagnetic Compatibility, 2001, 43, (4), pp.662-667

Publication II

T. Björninen, S. Merilampi, L. Ukkonen, L. Sydänheimo, P. Ruuskanen, “The effect of fabrication method on passive UHF RFID tag performance,” *Intl. J. Antennas Propag.,* vol. 2009, Article ID 920947, 8 pages, May 2009.

Errata

In the last sentence of the third paragraph of Section I: ”0.37 percent of” should be ”by factor of 0.37 compared with”.

In Fig. 5b the y-axis should be labelled ”Reactance [Ω]”.

Hindawi Publishing Corporation
International Journal of Antennas and Propagation
Volume 2009, Article ID 920947, 8 pages
doi:10.1155/2009/920947

Research Article

The Effect of Fabrication Method on Passive UHF RFID Tag Performance

Toni Björninen,[1] Sari Merilampi,[2] Leena Ukkonen,[1] Lauri Sydänheimo,[1] and Pekka Ruuskanen[2]

[1] *Rauma Research Unit, Institute of Electronics, Tampere University of Technology, Kalliokatu 2, 26100 Rauma, Finland*
[2] *Department of Electronics, Tampere University of Technology-Pori, Pohjoisranta 11 A, 28100 Pori, Finland*

Correspondence should be addressed to Toni Björninen, toni.bjorninen@tut.fi

Received 22 October 2008; Revised 11 February 2009; Accepted 7 May 2009

Recommended by You Chung Chung

In passive Radio Frequency Identification (RFID), transponders or tags are used to label objects to be identified. In this study passive tag antennas were produced using etching, screen-printing, and gravure printing methods. The threshold and backscattered signal strengths of the tags were measured to determine the effect of different manufacturing methods on the tags' performance. Conductivity, skin depth, thickness, and the quality of the conducting layer have a major effect on tag performance. Each manufacturing method sets its own boundary conditions on the processibility of the high quality conduction layer and such conditions need to be considered in tag design. Tag design also affects the manufacturing parameters used in the different techniques. The results of the study show that each of the studied fabrication methods can be used to manufacture reliable RFID tags.

1. Introduction

The use of passive UHF RFID systems is increasing rapidly in numerous applications. Globally, the allowed frequencies for UHF RFID range from 840 MHz to 955 MHz, depending on the local regulations [1].

Antennas are integrated into a variety of applications such as product packaging and clothing. Currently copper is the most commonly used conductor in tag antennas and the etching is the most widely used manufacturing technique to produce the conductive patterns. However, the cost of antennas is a crucial factor in the mass production of antennas and there is an increasing need to develop new manufacturing techniques to enable the manufacturing of RFID tags on complicated curved surfaces at economically competitive cost. This can be achieved by applying new economical manufacturing methods to produce the antenna structures. Printing techniques may provide a new and fast way to do this. In printed electronics silver particles are often used to form the conductive layer, and therefore it is important to optimize the amount of silver and the thickness of the conductive layer. At the same time it is also important that the ink layer is thick enough to achieve low ohmic losses. However, in RFID systems thin conducting layers are preferred to maintain low manufacturing costs.

The penetration depth and ohmic losses of the conductive layer set the boundary condition for the manufacturing methods and manufacturing parameters such as the amount of silver and the thickness of the layer. One factor controlling the thickness of the conductive layer is the skin effect or penetration depth. At high frequencies, like UHF, the current density is packed in the region near the surface of a good conductor. This is called the skin effect. Skin depth or penetration depth is defined as the depth below the surface of the conductor at which the amplitude of the incident electric field decays to 0.37 percent of the amplitude at the surface of the conductor.

For good conductors, the penetration depth has the well-known approximate expression

$$\delta = \frac{1}{\sqrt{\pi f \mu \sigma}}, \tag{1}$$

where f is the frequency, μ is the permeability ($\sim \mu_0$), and σ is the conductivity of the conductor material [2].

RFID tags can be made in various ways. In this study, etching, screen, and gravure printing techniques were compared and used to produce RFID antennas. Etching, which is the traditional way of making the conductors, was used as a reference technique for the printing techniques. It is a well-known method and is widely used to produce conductive patterns in the electronics industry. However, printing techniques have several advantages over the etching technique. Printing is a fast and environmentally friendly process; less hazardous chemicals are needed and printing can be used to produce 3D conductive patterns in an economically competitive way.

In etching process, a thin copper or aluminum foil on a substrate material is etched into the form of the designed antenna pattern. In an industrial process the IC-chip can be connected to the antenna, for example, by reflow soldering. In case the antenna is etched on a special substrate, which does not tolerate reflow process or the antenna pattern is printed, conductive adhesives can be used. Usually the antenna structure is also shielded with a thin layer of plastic to improve its endurance. In etching process, the substrate material must tolerate the chemicals used in the etching process, and this restricts the choice of substrate material. Polyethelene Terephthalate (PET) is commonly used as an antenna substrate material. The thickness of the foils is typically 18 μm or 35 μm for copper and 9 μm for aluminum. A typical etchant is ferricloride, which corrodes both copper and aluminum. The thickness of the conductor metal has an influence on the etching process, tag antenna performance, and also on the manufacturing costs [3–5].

In the electronics industry there is increased use of a variety of printing techniques to produce electrical conductors. The main components used in a printed RFID antenna are conductive ink and a substrate. Conductive inks consist of a polymer matrix, conductive fillers, and solvents. Silver particles are commonly used as the conductive filler material. Paper, plastic, and fabric can be used as the substrate material. The printing techniques offer a new way to transfer electronics circuits onto several materials, such as paper, plastic, and fabric. Different printing technologies require different ink characteristics [3, 6].

Screen printing is commonly used in electronic manufacturing. The conductive ink is pressed through a stencil onto the substrate with a squeegee. The stencil consists of the frame and a fabric mesh of threads. The advantage of this technique is that it enables very thin printing and also very thick films (from 0.02 μm to 100 μm according to [5]). The thickness of the ink layer is determined by the screen and the printing parameters. One possible constraint with screen printing is resolution, which reaches a maximum of about 50 lines per centimetre [4, 6, 7].

Gravure printing is a technique, which uses an engraved cylinder to transfer the figure to the substrate. The engraved figure on the cylinder consists of gravure cells which hold the ink while transferring the figure [8]. Gravure printing is used for very long runs. It is a fast technique and enables mass production. The thickness of the printed figure depends on the engravings on the gravure cylinder but process parameters such as printing speed and pressure also have an effect on the figure. In article [9] 20–60 μm gravure cells produced a 4–7 μm ink layer. The substrate must be flexible in gravure printing because of the pressure needed in figure transfer. The resolution that can be achieved with gravure printing is 100 lines per centimeter according to [6].

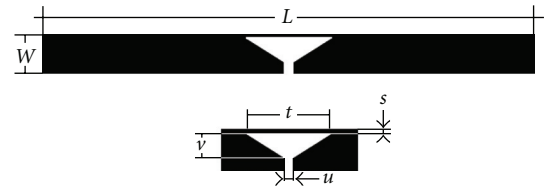

Figure 1: Shape and dimensions of the printed tag design.

2. Experimental Arrangements

2.1. Simulations. Input impedance at the antenna terminals depends on the geometry and material of the antenna and all other proximate materials. By definition, the radiation resistance of an antenna is the resistance, which relates the radiated power to the current at the antenna terminals. Similarly antenna loss resistance relates the terminal current to the difference of the accepted power and radiated power. The total resistance at the antenna input is the sum of these two resistances and its input reactance is related to the reactive power in the near field zone [10]. Antenna impedance is therefore strongly dependent on the antenna radiation and near-field coupling, which makes it a complicated parameter as a whole. Nevertheless antenna impedance is an important parameter in antenna design, since the power delivery to the load depends crucially on the impedance matching between the antenna and load impedances. In this study Ansoft's High Frequency Structure Simulator (HFSS) was used to design complex conjugate match between the antenna and load impedances.

Tag antennas used in the present study are rectangular short dipole tags equipped with a triangular matching loop. This matching technique is a slightly modified embedded T-matching, which is discussed in [11]. The embedded T-matching with a rectangular gap is successfully used for tag antenna matching, for example, in [12], but in the simulations we found the triangular gap better suited for our design.

Figure 1 shows the geometry of the screen-printed and gravure-printed tags and the dimensions of the designs are gathered in Table 1.

From the simulated antenna impedance we calculated the Power Reflection Coefficient (PRC) [12], which describes the quality of the complex conjugate match. According to the calculated PRC, the dimensions of the matching loop were adjusted to tune the screen-printed tag and the etched tag for optimal operation at 866 MHz. The IC-chip for both designs is Alien Higgs H2 [13]. It is provided by the manufacturer in a strap, which is readily attached to antenna structure.

Table 1: Dimensions of different antenna designs.

Dimension [mm]	Screen- and gravure-printed	Etched
W	8	9
L	97	100
s	17	15.6
t	0.5	0.5
u	2	2
v	5	6

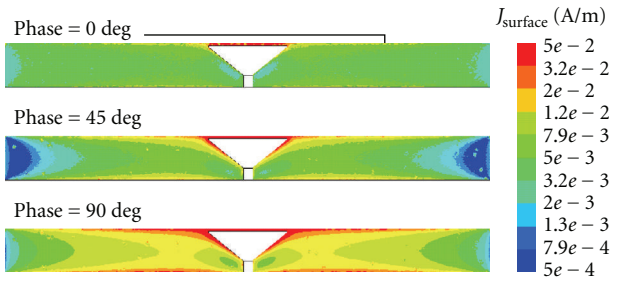

Figure 2: Simulated surface current density in the antenna structure under a plane wave incidence with different phases of incident wave.

In our study we have used impedance $Z_c = (17 - j137)\,\Omega$ to model the strap at 866 MHz, in order to maximize power transfer at this frequency, but in reality the strap impedance changes with frequency. In addition the dipole antenna is not designed for operation in the Global UHF RFID frequency range, and therefore we have limited our study around the European RFID frequencies.

In practice the nonuniform distribution of the ink becomes apparent when the printed layer is very thin, as in the gravure-printed tag. This effect is particularly evident in narrow traces, where the current density is high, such as in the matching loop of the manufactured tag (see Figure 11). The high current density in this part is shown in Figure 2, which illustrates induced current density in the structure under a normal plane wave incidence with amplitude 1 V/m.

The effect of the non-ideal print quality in this part the antenna was modelled afterwards by reducing the nominal trace width by 30% to account for the effect of the ragged edge of the actual printed conductor. This makes it possible to predict the frequency shift in the measurement results (see Figures 5 and 6).

2.2. Tag Fabrication. The RFID tags shown in Figure 1 were manufactured by screen printing, gravure printing and etching methods. PET was used as the substrate material for all prototype tags. The thickness of the PET substrate was 75 μm when printing was used for tag fabrication and 50 μm when etching was used for tag fabrication.

Screen-printed tags were printed with screen printable polymeric silver ink. The characteristics of the screen printing ink are presented in Table 2.

Gravure-printed tags were printed using polymeric rotogravure ink. The characteristics of the gravure printable ink are presented in Table 3.

Table 2: Characteristics of screen printable ink.

Manufacturer's description	Curing conditions (°C, min)	Viscosity (P)	Conductivity (MS/m)
Single component silver ink consisting of polyester resin and silver particles.	120, 20	200–300	1.25

Table 3: Characteristics of gravure printable ink.

Manufacturer's description	Curing conditions (°C, min)	Viscosity (P)	Conductivity (MS/m)
Silver pigment in a thermoplastic resin for flexographic or rotogravure printing techniques.	120, 20	40	4

Table 4: The printed samples.

Sample	Symbol	Printing equipment	Number of ink layers
Sample 1	Screen	Screen (mesh/width of thread: 124/27)	2
Sample 2	Gravure	Gravure cylinder (Depth of cells: 60 μm)	1

Information on the printed samples is presented in Table 4. Screen-printed samples were produced by printing two layers of ink. The ink layer was cured after the second printing. Rotogravure silver ink was diluted with n-Propylacetate before gravure printing.

Copper tags were produced by etching. Copper of 20 μm thickness on 50 μm thick PET foil were used as tag materials. The negative photosensitive resist foil was laminated on the copper and light exposure was performed under UV light. The resist was developed with 1.2% Na_2CO_3 and 32% $FeCl_3$ was used for the etching. The resist was stripped with 3% NaOH.

3. Measurement Equipments and Procedures

3.1. Thickness of the Printed Tags. The thickness of the conductive layer was measured before antenna measurements using software connected to an optical microscope. The thickness values are an average value of 20 different measurement points in the middle of the cross-section, which is marked Figure 3 by the red line. Location was selected by visual inspection to represent a typical distribution of the printed ink layer.

The copper layer is more uniform than the printed layers and has a thickness of 20 μm as reported by the copper foil manufacturer.

3.2. Antenna Measurements. Two different quantities, threshold power and backscattered signal power, were measured

Figure 3: Location of the cross-section for the thickness measurement.

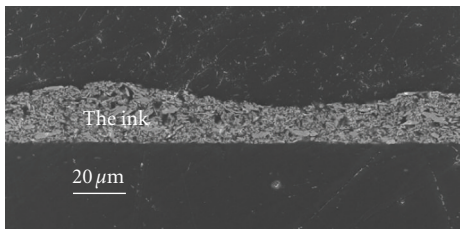

Figure 4: Scanning electron micrograph of a cross-section of a screen-printed sample.

to study the performance of the fabricated tags. All the measurements were made with Voyantic Tagformance measurement unit [14]. The distance for threshold and backscatter measurements was 1.5 m.

Threshold power is the minimum sufficient power to activate the IC-chip. Measurement of threshold power was performed by increasing the transmitted power until the tag can respond to the reader's query command. The effect of path loss and tag antenna gain can be approximated by using a calibration tag, with known properties. Calibration tag is provided by the manufacturer of the measurement device, as part of the measurement system. Decisive factors for the threshold power are the quality of the conjugate match between the antenna and the IC-chip, and the sensitivity of the IC-chip.

Backscattered signal power is a critical factor for the performance of an RFID tag. Assuming that the tag has sufficient power to activate the IC-chip, backscattered signal power together with the reader's sensitivity are the key factors for the tag-reader read range and reliability of the reception.

In addition to the above-described performance parameters an intuitive way to evaluate the performance of an RFID tag is the detection range. It is the maximum distance at which a valid response from the tag can be received. In a passive RFID system the detection range is typically limited by the forward link operation and more specifically the IC-chip's sensitivity. Detection range also depends on the radiation patterns and polarization of the reader antenna and the tag and the propagation channel. The detection range patterns in two orthogonal planes were measured for the fabricated tags. In this measurement the polarizations of the reader and tag antenna were matched and measurement was done with 2 W transmitted ERP-power, which is the maximum allowed transmitted power in the European RFID band.

4. Results and Discussion

4.1. Thickness of the Printed Tags. When printing is used to produce prototype tag antennas there are thickness variations in the ink layer. The thickness measurement results of the printed samples are presented in Table 5. The variation in the ink layer after screen printing can be seen in Figure 4. The variations in thickness make the modeling challenging, but a good estimate of the ink layer thickness can still be found by multiple measurements.

Table 5: Thickness measurement statistics for the printed tags.

Sample	Average [μm]	Min [μm]	Max [μm]	Standard deviation [μm]
Screen	21.5	16.8	26.0	2.5
Gravure	3.8	1.6	5.4	0.8

4.2. The Antenna Measurements. Simulated antenna impedances for different antennas are shown in Figure 5. Corresponding PRC's are presented in Figure 6, where the dashed blue and black curves correspond to situations where strap reactance would be 3 Ω less or 3 Ω more than the nominal value, respectively. Figure 7 shows the simulated PRC's for different antennas with nominal strap impedance. For gravure-printed tag two simulations were performed: "nominal" and "realized". The former term refers to nominal design and the latter to the simulation where the effect of the nonuniform distribution of the conductive ink was taken into account.

Measurement results for threshold power and backscattered signal power are presented in Figures 8 and 9, respectively.

Simulation results in Figure 5 predict that the nominal antenna resistances and reactances are within 5 Ω from each at the studied frequencies. Simulated resistance of the realized gravure printed tag is slightly increased from the nominal one, but it is still within 5 Ω from the simulated resistance of the other tags. Its reactance, however, differs significantly from the simulated reactances of the tags.

In reality accurate knowledge of the chip impedance is important for realization of impedance matching at the intended frequency. To account for uncertainties in the strap impedance, due to parasitics of the chip package and attachment to the antenna, ±3 Ω variations from nominal reactance was studied in Figure 6. Study was performed for chip reactance, since in simulations it was found to have stronger effect on the PRC's frequency behavior. According to this simulation ±3 Ω change in chip reactance may shift the operation frequency around 10 MHz from the nominal case.

Simulation results in Figure 7 were obtained with nominal strap impedance and one can see that all the designs are reasonably well tuned for operation at 866 MHz. It should be noted that conductivity and thickness of the conducting layer affect the radiation efficiency. The measured threshold power curves in Figure 8 therefore appear in a different order to the simulated PRC's in Figure 7. However, the simulation results can be used to predict fairly accurately the operating frequencies corresponding to the minimum threshold powers as well as their mutual order; only the measured operation frequency of the screen-printed tag

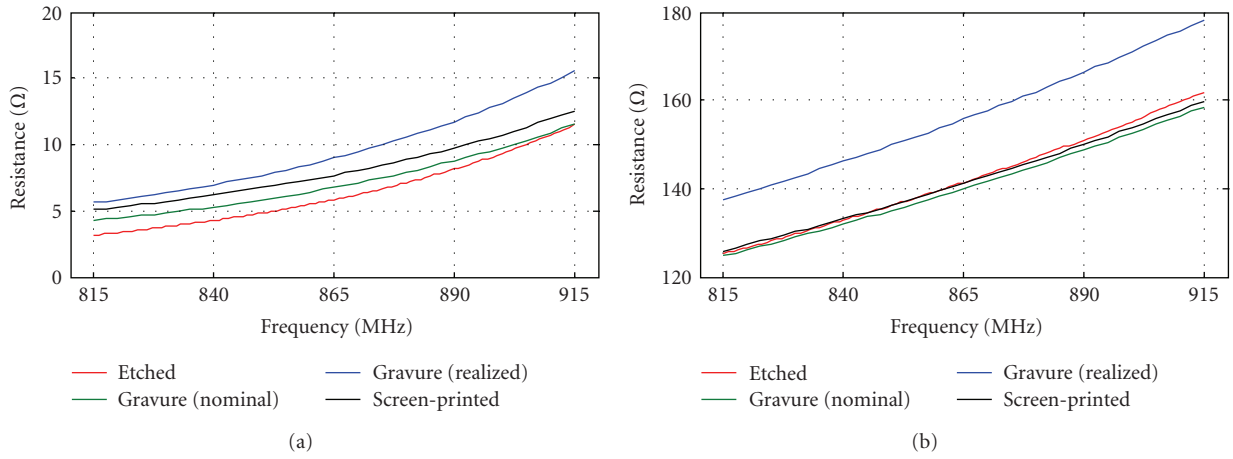

Figure 5: Simulated antenna impedances.

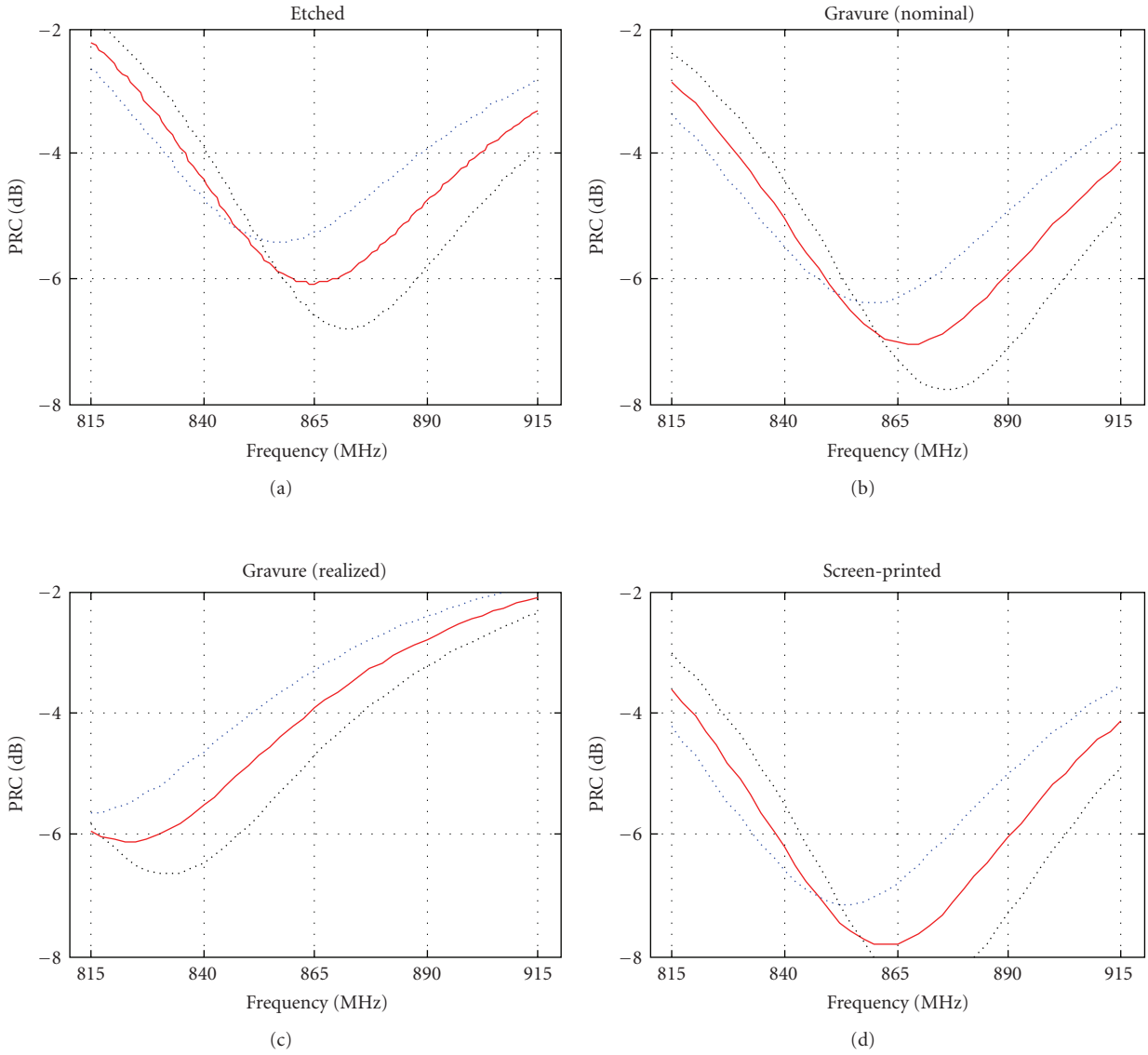

Figure 6: Calculated PRC's according to simulated antenna impedances with −3 Ω (red dashed curve) and +3 Ω (black dashed curve) tolerances for chip reactance.

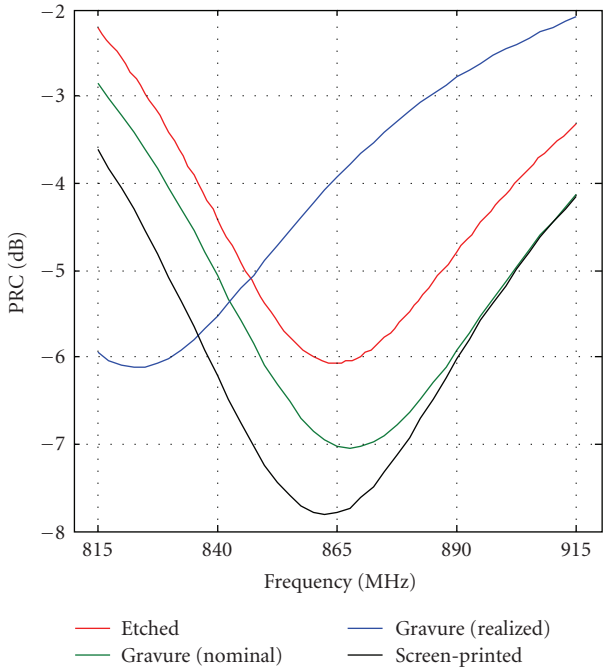

Figure 7: PRC's of different antenna models according to the simulated antenna impedances.

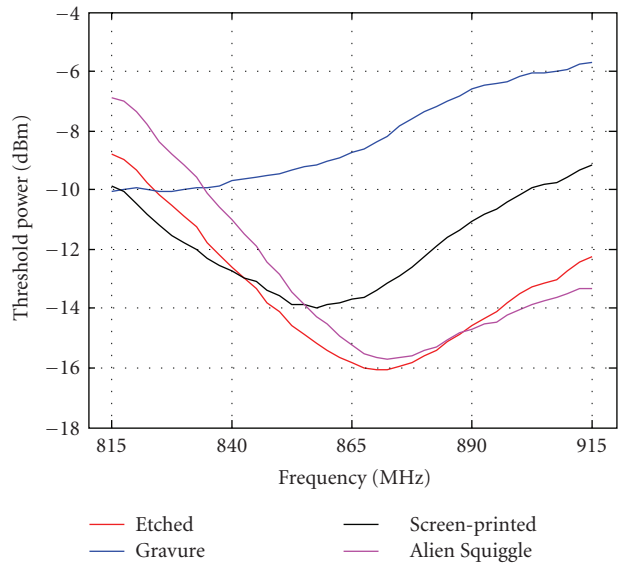

Figure 8: Measured threshold power versus frequency.

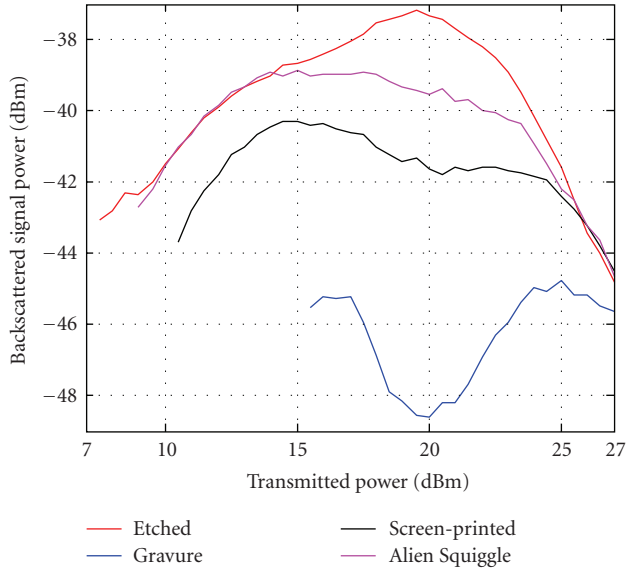

Figure 9: Measured backscattered signal power versus transmitted power at 866 MHz.

seems to be slightly lower than predicted. This might be due to lower than expected strap reactance, as results in Figure 6 suggest.

The measurement results for backscattered signal power in Figure 9 show that at the threshold power, when the IC-chips on the different tags receive approximately equal power, the strength of the responses are almost the same from the etched and screen-printed tags as well as from the commercial Alien Squiggle tag, which was measured as a reference. Response from the gravure-printed tag is about 2 dB weaker.

Since the manufactured tags are very similar to each other, differences in the measured power levels can be attributed to differences in conductivity and conductor thickness. The commercial Alien Squiggle tag was measured here to provide a frame of reference for the measured values. However, since it is smaller in size, no direct comparison can reasonably be made of its performance against the results from the other tags.

Measured detection range patterns for the fabricated tags are presented in Figure 10. On the left is the orthogonal plane for the dipole axis (H-plane) and on the right is the plane containing the dipole axis (E-plane). The mutual order of the measured detection ranges corresponds with the measured threshold powers, but results in Figure 10 provide yet another way to evaluate the fabricated tags' performance. In addition the detection range patterns show how the radiation pattern of the tag affects its detection range, expectedly the measured patterns follow the shape of dipole radiation pattern. Comparing the obtained results between each other it should be remembered, that the detection range for the Gravure-printed tag is not optimal, since as discussed above, the impedance matching of the fabricated gravure printed tag was impaired due to the fabrication process. Nevertheless the measured detection range for the gravure-printed tag demonstrates how the fabrication method may affect the performance of the tag. In this case the maximum achievable range remains around 4 meters, which is quite modest compared to the screen-printed tag. Taking into account that the measured threshold power for the screen-printed tag was 2 dB higher than for the etched tag (see Figure 8), we conclude that the measured detection range for the screen-printed tag is comparable with the etched tag.

The penetration depth of gravure ink is 8.6 μm at 866 MHz. This means that the ink layer thickness is less than

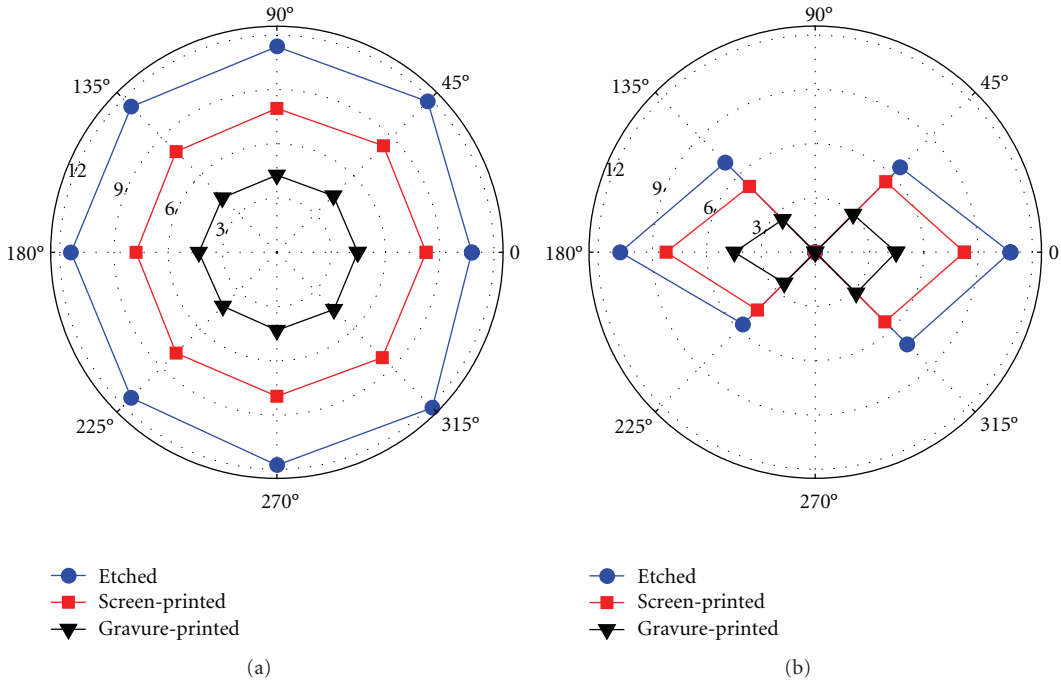

Figure 10: Measured detection ranges (m) at 866 MHz in two orthogonal planes, using 2 W ERP-power.

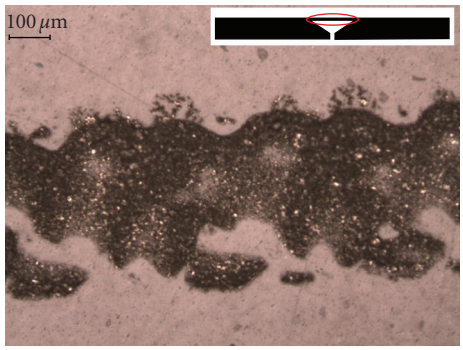

Figure 11: Narrow conductive line in antenna, printed with gravure printing.

half of the penetration depth, which affects the performance of the gravure-printed tag by increasing the ohmic losses. As Figure 11 shows, coverage of the ink is not perfect in the narrow part of the antenna and this has probably also affected the measurement results.

The penetration depth of screen printable ink is 15 μm at 866 MHz because its conductivity is lower than the conductivity of the gravure printable ink, which means that a thicker layer is required when screen printing is used.

The penetration depth in copper is 2.2 μm at 866 MHz and so the 20 μm layer is thick in comparison to the penetration depth. The current density has reduced approximately 95% of its value at the surface after three penetration depths. Therefore it can be assumed that the current flow is not adversely affected by the structure and the ohmic losses remain low [1].

The performance of printed silver ink dipole antennas and copper dipole antennas are investigated, for example, in [15]. Authors found that although silver inks are considerably less conductive, they are competitive when more material is used and can be competitive when using at 1 mm line widths. Copper dipoles were found to be more efficient than silver ink dipoles of similar dimensions due to the higher conductivity of copper. Authors of [15] also made a simple RFID tag and measured the threshold power, which was higher in case of silver ink tags. Also in [16] silver ink was found to be suitable for fabrication of UHF RFID tags. Printed coil tag antennas were investigated in [17] and they were shown to have read ranges comparable to the copper wire antennas. In [18] RFID bow-tie tag printed with ink jet technique provided good overall performance.

The results we obtained are in accordance with above mentioned results in the references. Printed tags were tuned at the desired frequency and we managed to manufacture a printed tag with almost the same geometry as the copper tag; only a minor change was done to optimize the antenna impedance.

Possible restrictions of printed tags are the maximum ink layer thickness and resolution achieved with different printing methods. Still it is possible to increase the conductivity of the ink, for example, by decreasing the particle size and adding solid content of the ink, but this increases the tag price. Also the printing method has to be selected according the tag model and materials. So it is most probably possible to achieve the same performance as the etched tags, but this increases the costs.

Antenna designing is always a compromise between, among other things, antenna performance, physical dimen-sions of the tag, price, materials (substrate material,

conductor material, materials nearby during the use of the tag), and manufacturing requirements (process limitations).

5. Conclusions

RFID tags can be manufactured using each of the methods investigated in this paper. The performance of the fabricated screen-printed tag is comparable to the copper etched tag with the same conductor thickness. Observed minor difference in their performance is due to the lower conductivity of the screen-printing ink. Decreasing conductor thickness increases losses and thereby decreases efficiency and results to weaker backscatter from the tag.

For a thin conductor layer, the nonuniform distribution in the conducting material in a narrow trace which was included in the matching network of the antenna detuned the antenna significantly impairing its performance. Thus the print quality needs special attention when UHF RFID tags are printed using very thin conducting layers or narrow traces.

Obtained results support the use of printing process as an alternative to etching in manufacturing of RFID tags. Especially printing is an advantageous manufacturing method when the substrate does not tolerate the etching chemicals or tags need to be integrated directly on the product packages.

Acknowledgment

The financial support of the Finnish Cultural Foundation, Satakunta Regional Fund, and the Ulla Tuominen Foundation is gratefully acknowledged.

References

[1] EPCglobal, http://www.epcglobalinc.org/tech/freq_reg.

[2] C. A. Balanis, *Advanced Engineering Electromagnetics*, John Wiley & Sons, New York, NY, USA, 1989.

[3] W. Zoomer, "Printing technologies make their mark in radio frequency identification," Screenweb, a companion site of the screen printing magazine, 2006.

[4] T. L. Landers, D. B. Brown, E. W. Fant, E. M. Malstrom, and N. M. Schmitt, *Electronics Manufacturing Processes*, Prentice-Hall, Englewood Cliffs, NJ, USA, 1994.

[5] WebelementsTM, http://www.webelements.com/aluminium.

[6] A. Blayo and B. Pineaux, "Printing processes and their potential for RFID printing," in *Joint sOc- EUSAI Conference*, pp. 27–30, Grenoble, France, October 2005.

[7] J. Costenoble, "Rotary screen printing: the productive solution for HF/UHF RFID labels," *SGIA Journal*, pp. 7–10, 2005.

[8] S. B. Hoff, *Screen Printing: A Contemporary Approach*, Delmar, Albany, NY, USA, 1997.

[9] M. Pudas, N. Halonen, P. Granat, and J. Vähäkangas, "Gravure printing of conductive particulate polymer inks on flexible substrates," *Progress in Organic Coatings*, vol. 54, no. 4, pp. 310–316, 2005.

[10] W. L. Stutzman and G. A. Thiele, *Antenna Theory and Design*, John Wiley & Sons, New York, NY, USA, 2nd edition, 1998.

[11] G. Marrocco, "The art of UHF RFID antenna design: impedance-matching and size-reduction techniques," *IEEE Antennas and Propagation Magazine*, vol. 50, no. 1, pp. 66–79, 2008.

[12] L. Ukkonen, M. Schaffrath, J. Kataja, L. Sydanheimo, and M. Kivikoski, "Evolutionary RFID tag antenna design for paper industry applications," *International Journal of Radio Frequency Identification Technology and Applications*, vol. 1, no. 1, pp. 107–122, 2006.

[13] Alien Technology, http://www.alientechnology.com.

[14] Voyantic Ltd., http://www.voyantic.com.

[15] A. Syed, K. Demarest, and D. D. Deavours, "Effects of antenna material on the performance of UHF RFID tags," in *IEEE International Conference on RFID*, pp. 57–62, Grapevine, Tex, USA, March 2007.

[16] P. V. Nikitin, S. Lam, and K. V. S. Rao, "Low cost silver ink RFID tag antennas," in *IEEE Antennas and Propagation Society International Symposium (AP-S '05)*, vol. 2B, pp. 353–356, July 2005.

[17] S. Y. Y. Leung and D. C. C. Lam, "Geometric and compaction dependence of printed polymer-based RFID tag antenna performance," *IEEE Transactions on Electronics Packaging Manufacturing*, vol. 31, no. 2, pp. 120–125, 2008.

[18] L. Yang, A. Rida, R. Vyas, and M. M. Tentzeris, "RFID Tag and RF structures on a paper substrate using inkjet-printing," *IEEE Transactions on Technology Microwave Theory and Techniques*, vol. 55, no. 12, part 2, pp. 2894–2901, 2007.

Publication III

T. Björninen, M. Lauri, L. Ukkonen, R. Ritala, A. Z. Elsherbeni, L. Sydänheimo, “Wireless measurement of RFID IC impedance,” *IEEE Trans. Instrum. Meas.*, vol. 60, no. 9, pp. 3194-3206, Sept. 2011.

Wireless Measurement of RFID IC Impedance

Toni Björninen, *Member, IEEE*, Mikko Lauri, Leena Ukkonen, *Member, IEEE*, Risto Ritala, Atef Z. Elsherbeni, *Fellow, IEEE* and Lauri Sydänheimo, *Member, IEEE*

***Abstract*— Accurate knowledge of the input impedance of an RFID IC at its wake-up power is valuable as it enables the design of a performance-optimized tag for a specific IC. However, since the IC impedance is power-dependent, few methods exist to measure it without advanced equipment. We propose and demonstrate a wireless method, based on electromagnetic simulation and threshold power measurement, applicable to fully assembled RFID tags, to determine the mounted IC's input impedance in the absorbing state including any parasitics arising from the packaging and the antenna-IC connection. The proposed method can be extended to measure the IC's input impedance in the modulating state as well.**

***Index Terms*—Impedance measurement, Microwave radio communication, Microwave antennas, Error analysis, Monte Carlo methods**

I. Introduction

Radio Frequency Identification (RFID) system is a wireless automatic identification system, where objects are tagged with transponders, consisting of an antenna and an integrated circuit (IC). Passive RFID tags scavenge energy for their operation from an incident electromagnetic field, set by the reader unit. When the on-tag IC receives sufficient power to enable its full functionality, it is able to demodulate commands from the reader and to modulate the tag's response to the antenna-mode backscattered field by switching its input impedance between two values. Most importantly, the IC's memory contains a unique identification code providing an identity for the tagged object. Battery assisted passive tags are equipped with an on-tag battery to provide energy for the IC, but they also backscatter their response to the reader only under the reader's interrogation, as do the passive tags. Active RFID tags, on the other hand, are capable of independent transmission and they can act effectively as radio transmitters [1].

Manuscript received March 8, 2010. This work was supported by the Tampere Doctoral Programme in Information Science and Technology (TISE), Finnish Funding Agency for Technology and Innovation (TEKES), the Academy of Finland and the Centennial Foundation of Finnish Technology Industries.

Toni Björninen, Leena Ukkonen and Lauri Sydänheimo are with Tampere University of Technology, Department of Electronics, Rauma Research Unit, Kalliokatu 2, FI-26100 Rauma, Finland; e-mail: toni.bjorninen@tut.fi.

Mikko Lauri and Risto Ritala are with Tampere University of Technology, Department of Automation Science and Engineering, P.O. Box 692, FI-33101 Tampere, Finland.

Atef Z. Elsherbeni is with the University of Mississippi, University, MS 38677-1848, USA.

Computational electromagnetics (CEM) tools are essential in design of RFID tags of any type. Towards the end of the 20th century, many efficient CEM tools have become widely available for microwave engineers and at present a common work station computer can be used to simulate various microwave devices, including antennas. In field of RFID, CEM tools have been successfully applied to design efficient, compact tag antennas [2],[3]. Tag miniaturization is motivated by the application: tags need to be seamlessly integrated into product packages and have low manufacturing costs, but at the same time sufficient power transfer between the IC and the tag antenna need to be arranged to cover the global UHF RFID frequencies from 860 MHz to 960 MHz.

Research on different size-reduction and impedance matching techniques has been carried out in the RFID context [2]–[4] and the results from the research done in a more general setting [5],[6] are also available for engineers and researcher working on RFID. However, the lack of accurate knowledge of the IC's impedance may keep the tag designer from getting the full benefit out of the applied antenna design techniques. This is true particularly in design of broadband impedance matching, which is the principal design goal in many RFID tag designs. In view of this, accurate knowledge of the tag antenna properties, provided by CEM tools or measurements is not enough, but accurate knowledge of the IC impedance is crucial for successful tag design as well.

In the absorbing impedance state, the integrated rectifier and voltage multiplications stages provide sufficient DC voltage to enable the IC's functionalities. This frontend circuitry of the IC is typically composed of capacitors, diodes and semiconductor switches, making its input impedance capacitive and frequency and power dependent [7],[8]. In addition, the packaging of the IC, as well as the tag antenna-IC connection, affect the impedance, seen from the tag antenna terminals towards the IC, making the input impedance of the IC a complex quantity as a whole [9]. The same applies to the modulating state input impedance, which together with the absorbing state input impedance, determines the modulation efficiency of the tag [10],[19].

On the product datasheets, IC manufacturers typically list the input impedance of RFID ICs in the absorbing state at few frequency points in the global UHF RFID frequency band or provide an equivalent circuit model for the input impedance without presenting the actual measured impedance data. Further, the input impedance in the modulating state may not be listed at all. Thus, by measuring the chip impedance in both

operating states including the parasitic effects from the tag antenna-IC connection, uncertainty related to the conjugate impedance matching between the tag antenna and the IC can be significantly reduced and more insight to the efficiency of the backscattering modulation process can be obtained. We expect the latter to become increasingly important for passive tag design in the future as the sensitivities of the ICs improve and especially for battery assisted RFID where the on-tag power supply enables significantly better sensitivities to begin with.

If the power loss due to the impedance mismatch between the tag antenna and the IC is small enough, the IC may remain operational at any available incident power above its sensitivity level. Thus, the complex conjugate of the IC's input impedance at the sensitivity level is commonly taken as the target for the tag antenna design. In practice the input impedance of an RFID IC has a strong dependence on the incident power and therefore carrying out the impedance measurement at an appropriate incident power to the IC is of great importance [11].

Typical measurement configurations to determine the IC's input impedance include an RFID tester to determine the threshold power and a vector network analyzer (VNA) for measuring the impedance of the IC [12]. The frequency dependent threshold power of the IC is first determined with the RFID tester and the impedance is then measured at this power. The input impedance of the IC is capacitive and varies significantly from the typical 50-Ω characteristic impedance of measurement devices. This is problematic since the sensitivity of VNAs is best around their characteristic impedance with performance decaying rapidly with loads differing from the characteristic impedance [13]. By using static pre-matching [14], VNA measurements are more accurate and the incident power on the IC can be adjusted easily. Direct measurement of the input impedance of the bare IC has the disadvantage that the result does not include the effect of mounting parasitics. This can be alleviated by mounting the IC on a sample of the antenna material [12] or by employing a method for verifying the matching condition between the antenna and IC [15] specifically suitable for assembled RFID tags.

In this article, we propose a wireless measurement method for measuring the absorbing state input impedance of an IC mounted on an RFID tag, by combining information from CEM simulations and far field measurement while communicating with the tag using the EPC Gen2 protocol. The method requires few specialized measurement devices and it can be extended to measure the modulating state input impedance as well.

The rest of the article is organized as follows. Section II introduces the theoretical background and formulation of the measurement method. In Section III the design of the test tag antennas is discussed and the related simulation results, as well as the raw measurement data are presented. Section IV presents the results for the IC impedance and the uncertainties of the method, in Section V measured tag antenna performance is compared with a prediction based on simulation with the measured IC impedance and finally conclusions are drawn in Section VI.

II. Proposed Measurement Method

A. Power Transfer between Complex Impedances

Perfect power transfer between complex source Z_S and load Z_L impedances occurs only when the impedances are complex conjugates of each other. Kurokawa studied the concept of power waves [16] and derived an expression for the ratio of the available power from the source (P_S) and the reflected power (P_R) from the load due to impedance mismatch:

$$\frac{P_R}{P_S} = \left| \frac{Z_L - Z_S^*}{Z_L + Z_S} \right|^2 = |\rho|^2, \tag{1}$$

where $(\cdot)^*$ denotes the complex conjugate. The impedance ratio, denoted by ρ in equation (1) is also defined as the power wave reflection coefficient [16]. By observing that power $P_S - P_R = P_L$ is delivered to the load, the power transmission coefficient (τ) or the matching coefficient between the source and the load can be written as

$$\tau = \frac{P_L}{P_S} = \frac{4R_S R_L}{|Z_S + Z_L|^2} = \frac{4R_S R_L}{|Z_S - (-Z_L)|^2}, \tag{2}$$

where the second equality follows from equation (1). As we assume that R_s and R_L are strictly positive, it holds that $0<\tau\leq 1$ with the value $\tau=1$ being attained only under the conjugate matched condition: $Z_S=Z_L^*$ and the value $\tau=0$ being approached as the distance between Z_S and $-Z_L$ in the complex plane tends to infinity. In this study we use equation (2) to describe the quality of the power transfer between the tag antenna and the IC.

B. Threshold Power and Link Calculations for a Far Field RFID System

For far field RFID systems, the Friis' model [17] can be applied to approximate the delivered power to the IC (P_{IC}) from the generator. In the present study we use linearly polarized antennas on tag and reader side, which we have carefully aligned to minimize the link loss due to polarization mismatch and thus the Friis' model is applied assuming perfect polarization matching. Under this assumption

$$P_{IC} = \tau L_C G G_{TX} \left(\frac{\lambda}{4\pi d} \right)^2 P_{TX}, \tag{3}$$

where L_C is the cable loss factor, G_{TX} and G are the gains of the transmitter antenna and the tag antenna, respectively, P_{TX} is the time-averaged transmitted carrier power, d is the distance between the transmitter antenna and the tag antenna and τ is

the power transmission coefficient between the tag antenna and the IC.

In the absence of any multipath propagation and assuming that the receiver sensitivity is not limiting the communication with the tag, which is commonly the case with passive RFID tags, the transmitted power is given as

$$P_{TH} = \frac{P_{IC,0}}{\tau L_C G G_{TX} \left(\frac{\lambda}{4\pi d} \right)^2}, \quad (4)$$

when the delivered power to the IC equals the IC's sensitivity, denoted $P_{IC,0}$. Since in practice the sensitivity of the IC is defined with respect to an operation that produces an observable response from the tag, also P_{TH} has this property. Commonly, the sensitivity of the IC refers to its read sensitivity, i.e. to the minimum power required to reply to the EPC Gen2 protocol's *query* command. This is the most common and expectedly the least power consuming task for the IC, since the tag's reply to *query* consists only of its ID number. Therefore we adopt this definition for the IC's sensitivity as well.

As we measure the impedance at the read sensitivity of the IC, the measurement result can be useful for designing RFID tags with maximal readable range. However, it may not yield maximal operation range for other commands such as *write*.

In order to solve equation (4) with respect to the IC's impedance, contained implicitly in τ, all the other quantities in the equation need to be known and since the impedance is a complex quantity, a pair of equations is required to produce solutions for both real and imaginary parts. As modern CEM tools allow accurate simulation of simple antenna structures, we use three plain straight dipoles as test tags. These antennas, the simulation results and the developed procedure to obtain the IC impedance are described in the next section. In addition, we measure the gain of the transmitter antenna and use the IC's sensitivity provided by the manufacturer.

In the tag measurements, we used a compact anechoic cabinet and in order to further suppress any possible multipath propagation due to the non-idealities of the measurement environment, we have mapped P_{TH} to its free space value by multiplying the raw measurement quantity by a correction factor

$$\Lambda = \frac{L_{tot}}{L_c G_{tx} \left(\frac{\lambda}{4\pi d} \right)^2}, \quad (5)$$

where L_{tot} is the path loss, from the transmitter output to an imaginary unity-gain tag and L_c is the cable loss between the generator output and transmitter antenna. In our measurements, the quantity L_{tot}, is obtained through a calibration procedure included in the measurement equipment used. This process is based on measuring a reference tag with accurately known properties, which allows the system to calculate L_{tot}. For calibration, we used a reference tag provided by the measurement device manufacturer.

Though path loss correction by using the factor Λ can provide additional accuracy, correcting the measured P_{TH} is not in general necessary; the IC impedance can be obtained similarly through the procedure described below by assuming perfectly anechoic measurement environment. Therefore we have suppressed the factor Λ from the formulation presented, yet keeping in mind that at any point P_{TH} can be replaced by ΛP_{TH}.

C. Measurement of an RFID IC's Absorbing State Input Impedance

Proceeding with the solution of equation (4) with respect to the IC's impedance, the tag antenna and the IC impedances are denoted by $Z_A=R_A+jX_A$ and $Z_L=R_L+jX_L$, respectively. Considering the tag antenna as the source and the IC as the load and taking τ to be constant, equation (2) can be rearranged to

$$4R_A^2 \frac{1-\tau}{\tau^2} = \left(R_L - R_A \frac{2-\tau}{\tau} \right)^2 + \left(X_L - \left(-X_A \right) \right)^2, \quad (6)$$

which defines a circle in the complex plane with center point

$$P(\tau) = \left(R_A \frac{2-\tau}{\tau}, -X_A \right) \quad (7)$$

and radius

$$r(\tau) = 2R_A \frac{\sqrt{1-\tau}}{\tau}. \quad (8)$$

Thus, measuring P_{TH} for two tag antennas and solving τ for each measured tag from equation (4), substituting the measured values into equations (6)-(8) and locating the intersection points of the constant-τ circles obtained yields the solutions for the IC's impedance. However, as two circles may intersect each other at zero, one, two or an infinite number of points, care must be taken to pick the physically meaningful solution. The cases with one or infinite number of intersection points are special cases, rarely if ever arising in our measurement procedure and therefore we assume to have zero or two intersection points throughout the presented analysis. In the case with two intersection points, only one of them can represent the physical solution and if, due to measurement uncertainty or errors, the circles do not intersect, the IC's impedance cannot be determined from the data.

To pick the physical solution for the IC's impedance corresponding to one of the two intersection points of the constant τ-circles defined by equations (6)-(8), we use three test tags to obtain three pairs of equations, each producing two pairs of solutions. Three is the minimum number of tags required for identifying the physical impedance solution with

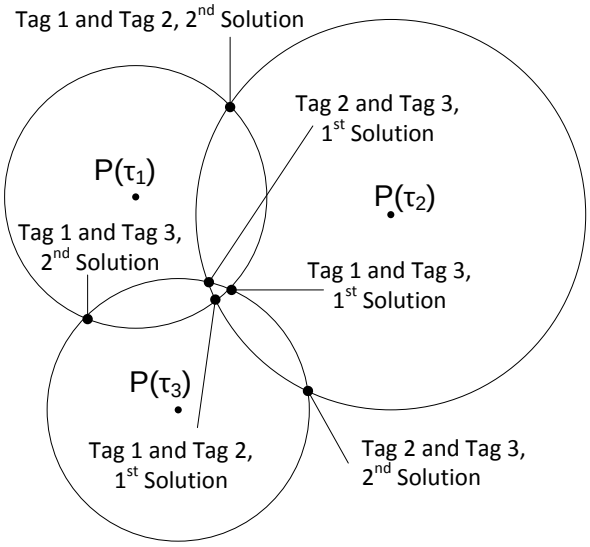

Fig. 1. Illustration of constant-τ circles obtained by measuring P_{TH} of three test tags and solutions for the IC's impedance produced by each test tag pair. The centre points and radii of the circles are determined by equations (7) and (8), respectively.

the method described here, but using more test tags could improve the accuracy of the measurement method, since the threshold power measurement would be repeated for a greater number of individual ICs.

Assuming a sufficiently small measurement uncertainty and identical ICs in all the test tags, the physical solutions produced by each tag pair are expected to be bunched close to each other – ideally at the same point – in the complex plane, as illustrated in the Fig. 1. To identify these solutions, we consider the solution triplets (circle intersection points marked in the Fig. 1) where only one solution produced by each tag pair is included. For clarity, these triplets are listed in Table I. As we know that ideally the triangle spanned by the physical triplet would degenerate to a single point, we expect this triplet to be the three solutions on the same row in Table I, which span the triangle with the minimal circumference in the complex plane. Referring to the example in Fig. 1, this triplet would be formed by the first solutions produced by each tag pair

In this article, we only consider the case with three tags. With a number of tags $n > 3$, the selection of the physical solutions becomes more involved, since instead of triangles, n-polygons would need to be examined. As n increases, it might be useful to simply consider the sample variance of different solution combinations to determine the physical solution.

D. Measurement of an RFID IC's Modulating State Input Impedance

Assuming that the absorbing state input impedance of an IC is measured – or otherwise accurately known – the above method can be extended to extract the IC's modulating state input impedance based on the measured backscattered signal power. Below we assume that the backscattered power is measured at the transmitted threshold power, since during the backscatter measurement the incident power to the IC needs to correspond to the value at which the absorbing state input impedance is known.

TABLE I
SOLUTION TRIPLETS WHERE ONLY ONE SOLUTION PRODUCED BY EACH TAG PAIR APPEARS.

Tag 1 and Tag 2, 1st Solution	Tag 1 and Tag 3, 1st Solution	Tag 2 and Tag 3, 1st Solution
Tag 1 and Tag 2, 1st Solution	Tag 1 and Tag 3, 1st Solution	Tag 2 and Tag 3, 2nd Solution
Tag 1 and Tag 2, 1st Solution	Tag 1 and Tag 3, 2nd Solution	Tag 2 and Tag 3, 1st Solution
Tag 1 and Tag 2, 1st Solution	Tag 1 and Tag 3, 2nd Solution	Tag 2 and Tag 3, 2nd Solution
Tag 1 and Tag 2, 2nd Solution	Tag 1 and Tag 3, 2nd Solution	Tag 2 and Tag 3, 2nd Solution
Tag 1 and Tag 2, 2nd Solution	Tag 1 and Tag 3, 2nd Solution	Tag 2 and Tag 3, 1st Solution
Tag 1 and Tag 2, 2nd Solution	Tag 1 and Tag 3, 1st Solution	Tag 2 and Tag 3, 2nd Solution
Tag 1 and Tag 2, 2nd Solution	Tag 1 and Tag 3, 1st Solution	Tag 2 and Tag 3, 1st Solution

In the impedance modulation process, the input impedance of the IC is switched between the absorbing and modulating states, to modulate the response from the tag to the reader in the antenna-mode scattered field, which is the load dependent component of the total scattered field of the tag antenna [18]. The quality of this modulation procedure can be described with the modulated radar cross-section denoted as σ_m, which is analogous to the classical radar cross-section, but combines the tag antenna's reflectivity and the modulation efficiency of the tag. The total backscattered information carrying power equals the incident carrier power density at the tag's location multiplied by σ_m. Using 1:1 duty cycle in the impedance switching scheme to modulate the backscatter results in [19]

$$\sigma_m = \frac{G^2\lambda^2}{4\pi}\frac{1}{4}\left|\rho_1 - \rho_2\right|^2, \tag{9}$$

where ρ_1 and ρ_2 are the power wave reflection coefficients between the tag antenna and the IC in the absorbing and modulating states of the IC, respectively. Denoting the IC's impedance in the modulating state by $Z_M = R_M + X_M$, equation (9) can be written as

$$\sigma_m = \frac{G^2\lambda^2}{4\pi}\frac{R_A^2\left|Z_L - Z_M\right|^2}{\left|Z_A + Z_L\right|^2\left|Z_A + Z_M\right|^2} = \frac{G^2\lambda^2}{4\pi}L_{mod}, \tag{10}$$

where the explicitly impedance dependent part of σ_m has been defined as the modulation loss factor L_{mod}. Under the Friis' model [17], the backscattered signal power is

$$P_{BS} = \sigma_m \frac{\lambda^2 G_{TX}^2}{(4\pi)^3 d^4} P_{TH}, \quad (11)$$

when a single antenna with gain G_{TX} on the reader side is used for both transmission and reception. Since for a constant L_{mod}, equation (10) defines a circle in the modulating impedance plane, the intersection point method described in Section 2.3 for the absorbing state impedance can be applied for the modulating state impedance as well. In this article, we present measurement results only for the absorbing state impedance and reserve the more accurate description and demonstration of the measurement of the modulating state impedance for the future.

III. Test Tags and Measurement Results

The test tag antennas serve as test beds for the IC under test. From the point of view of tag antenna design, the only requirement for these antennas is sufficient gain and power matching with the IC to allow the threshold power measurement. Identical test tag antennas cannot be used, since as a result, the constant-τ circles illustrated in Fig. 1 would in theory lie on top of each other and the intersection point method described in Section II.C could not be used to find the solution for the IC's input impedance.

Keeping in mind that reliable simulation results for the test tag antennas are essential for the accuracy of the proposed method, simplistic antenna geometries are preferred. Because the measured impedance obtained from the proposed method is the input impedance of the whole circuitry beyond the test tag antenna terminals, it is important to mount the IC in the test tags exactly as in the tag antenna designs where the measured IC impedance is going to be used later.

We use straight dipole antennas to demonstrate the measurement method in practice. Dipole antennas have the advantage of structural simplicity, which facilitates accurate modeling. The dipoles are balanced structures to which ICs with differential input can be directly connected. Furthermore, dipole antennas are inherently linearly polarized, which simplifies the wireless link calculations. The size of the test tag antennas was selected so that within the studied frequency range they operate between their first and second resonance where the antenna input is inductive. This provides sufficient power matching to the IC under test to allow the threshold power measurement.

Three test tags, referred to as Tag A, Tag B, Tag C and an additional tag, Tag D were fabricated. Tag D was not used in the measurement procedure, but later to compare the measured and simulated tag antenna performance. The geometry and the dimensional parameters of all four tag antennas are shown in Fig. 2 and the values of the dimensional parameters are listed in Table II. As explained above, identical test tags cannot be used to measure the IC's impedance with the proposed method and therefore the length of each test tag antenna is different.

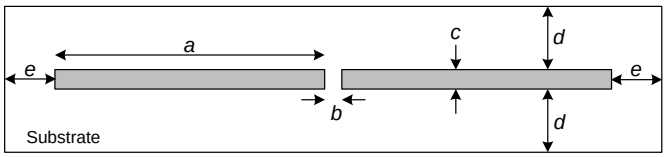

Fig. 2. Geometry and the related dimensional parameters of the test tags.

TABLE II
VALUES OF THE DIMENSIONAL PARAMETERS OF THE FABRICATED TAGS IN MILLIMETERS.

	a	*b*	*c*	*d*	*e*
Tag A	74.5	1	3	15	15
Tag B	79.5	1	3	15	15
Tag C	84.5	1	3	15	15
Tag D	89.5	1	3	15	15

TABLE III
ELECTRICAL PROPERTIES OF ROGERS RT/DUROID 5880.

Thickness	Relative permittivity	Loss tangent	Conductor material	Conductor thickness
3.17 mm	2.2	0.0009	Copper	35 µm

The assembled tags are equipped with the Alien Higgs-3 IC [20], which is provided by the manufacturer in a strap for easy attachment. Conductive epoxy was used to attach the strap to the antenna. Substrate material used for all fabricated tag antennas is the commercially available Rogers RT/Duroid 5880 with electrical properties listed in Table III.

The test tag antennas were simulated with the Ansoft High Frequency Structure Simulator (HFSS) based on the finite element method and a finite-difference time-domain (FDTD) code based on [21]. Simulated antenna impedance and gain in the direction normal to the antenna plane and away from the substrate are shown in Figs. 3-6. Good agreement between the results obtained by two fundamentally different CEM techniques provides additional assurance to our simulation procedures. Moreover, results from the two simulators serve as an example of the impact of small deviations in the simulated parameters to the final outcome of the proposed impedance measurement method.

The difference between the simulated impedance and gain between the different tag antennas is explained by the different length of the antennas alone, since all the other dimensional parameters are the same for all tags.

The threshold power of each test tag was measured in a compact anechoic cabinet with Tagformance measurement device [22], which is a measurement unit for RFID tag performance characterization. It allows power ramping at a defined frequency and thereby threshold power analysis. The

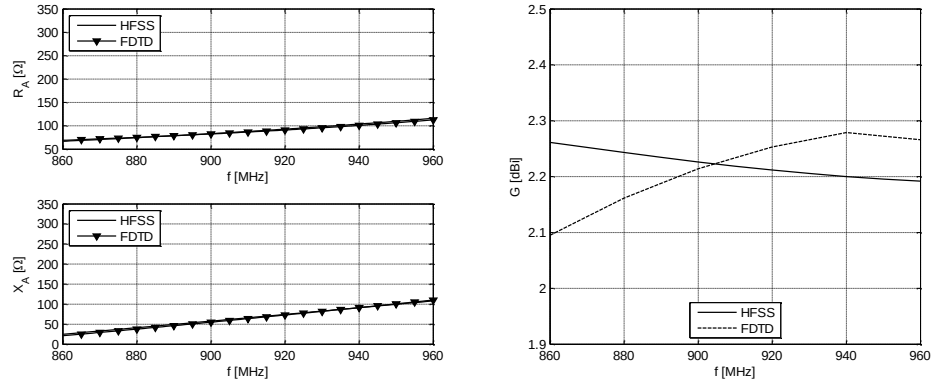

Fig. 3. Simulated impedance and gain of Tag A.

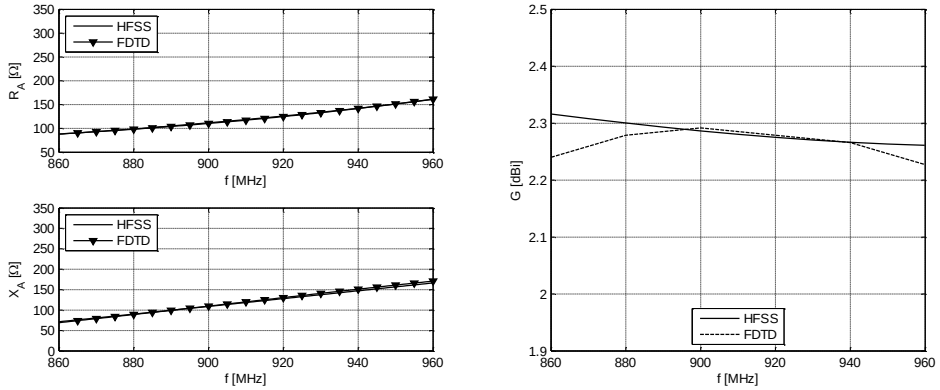

Fig. 4. Simulated impedance and gain of Tag B.

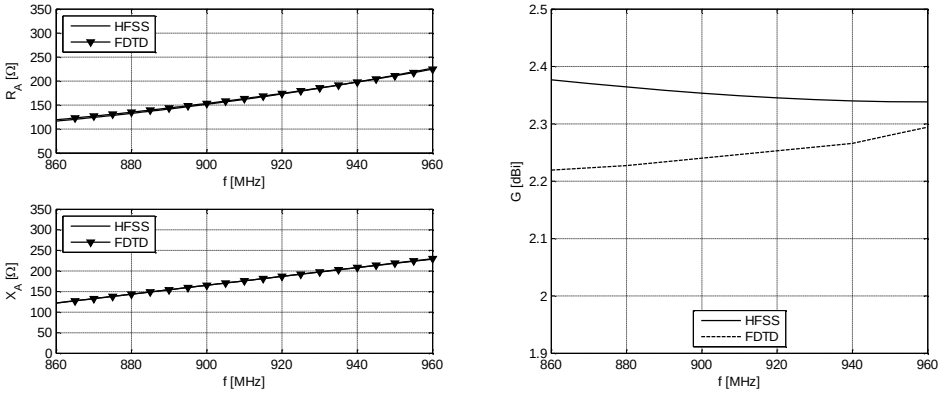

Fig. 5. Simulated impedance and gain of Tag C.

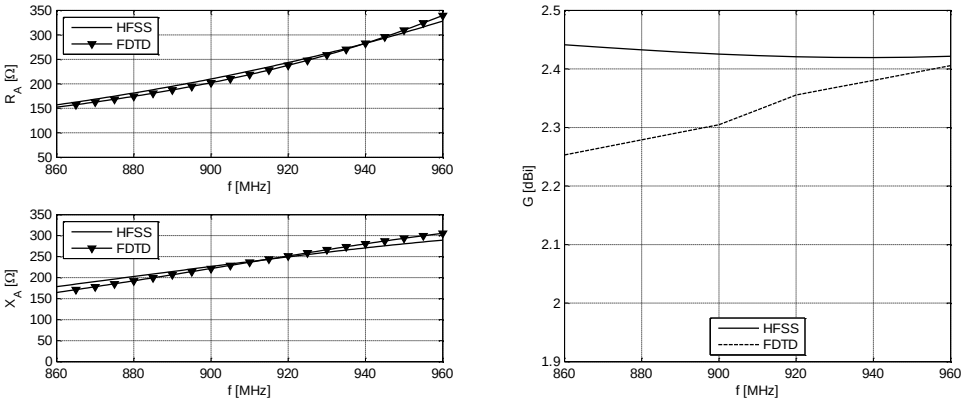

Fig. 6. Simulated impedance and gain of Tag D.

core operations of the device are performed with a vector signal analyzer. The sample mean of five threshold sweeps for each individual tag in identical conditions is presented in Fig. 7. In the measurement configuration, the separation between the linearly polarized transmitter antenna and the tag under test was 0.45 m and the transmitter antenna gain, provided by the manufacturer, is shown in Fig. 8

The measured threshold power of each test tag, shown in Fig. 7, is the raw measurement data for the proposed impedance measurement method. Each curve carries information about the tag antenna gain and impedance matching, which affect the power delivery from the incident wave to the IC. For example, the transmitted threshold power of Tag A at 900 MHz is $P_{TH} \approx 2.9$ dBm. At this frequency, the free space attenuation factor $(\Lambda/4\pi d)^2$ under the Friis' model is approximately −24.7 dB, the simulated tag antenna gain is 2.2 dBi (Fig. 3) and the transmitter antenna gain is 8.6 dBi (Fig. 8). Summing these values shows that around −11 dBm incident power on the IC enables response from the tag to the *query*. Since the read sensitivity of the IC is −18 dBm [20], there is an around 7 dB mismatch loss, which translates to a power transmission coefficient $\tau \approx 0.2$. As observed from Fig. 7, we were also able to conduct the measurement with much higher mismatch loss, corresponding to up to 6 dBm threshold power. This highlights the fact that the threshold power of the test tags can be successfully measured although knowledge of IC impedance is not available for designing impedance matching for these tags. Despite the observed mismatch the highest transmitted power we needed in the experiment was around 6 dBm. This implies that the measurement method is suitable for larger measurement chambers as well.

IV. IC Impedance and Measurement Uncertainty

We have applied a Monte Carlo simulation method to determine the IC's impedance and to quantify its uncertainty. In order to perform the simulation, we first estimate the probability density function (pdf) for the tag antenna impedance Z_A, gain G and threshold power P_{TH}. As shown by measurements in [12] and [14], the read sensitivity of RFID ICs is nearly constant in the bandwidth of interest and thus we take it to be constant in our simulations. As the conditions in the anechoic chamber remain constant during the threshold power measurement, we also assume the correction factor Λ defined in equation (5) to be constant.

A. Parametric pdf Estimation and the Simulation Procedure

Based on the principle of maximum entropy [23], we have chosen to represent the four quantities of interest as a vector valued random variable $\mathbf{x} = [R_A, X_A, G, P_{TH}]$, following a multivariate normal distribution $N(\mathbf{x}; \boldsymbol{\mu}, \boldsymbol{\Sigma})$ with parameters $\boldsymbol{\mu}$ and $\boldsymbol{\Sigma}$, the mean vector and covariance matrix, respectively. On any given frequency, the mean values for the impedance and gain of a tag antenna are obtained via CEM simulations. The mean value for threshold power at the IC's read sensitivity is obtained by using the measurement procedure described in Section III and computing the arithmetic mean of several repeated measurements. The elements of the covariance matrix are defined as:

$$\Sigma_{ij} = \begin{cases} \sigma_i^2 & \text{when } i = j \\ \rho_{ij}\sigma_i\sigma_j & \text{when } i \neq j, \end{cases} \tag{12}$$

where σ_i^2 is the variance of variable i and ρ_{ij} is the linear correlation coefficient between variables i and j. We assume the standard deviation (the square root of the variance) in both real and imaginary part of the tag antenna impedance and tag antenna gain to be proportional to their mean values. Mats et al. [24] studied the impedances of certain commercial tag antenna designs and found the 95% confidence limits of the real part of the impedances to be within ±10% of their mean value, but also less than 3 Ω even for antennas with a high resistive impedance. The 95% confidence limits of the imaginary part of the impedance was found to be at approximately 3% of their mean value. Additionally, they report that there is a slight positive correlation between the real and imaginary parts of the impedance. Based on this study, a standard deviation of 3% proportional to the mean value is set

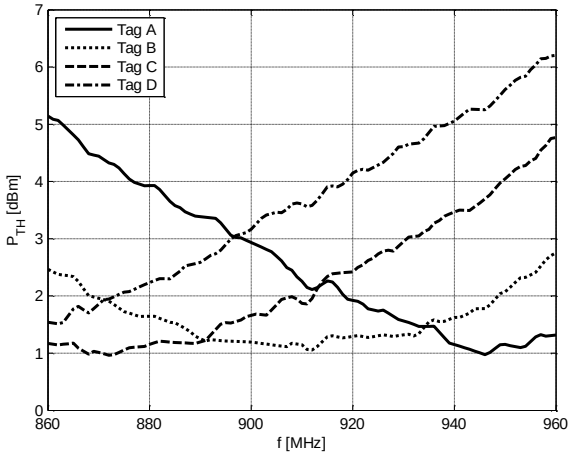

Fig. 7. Measured threshold power of the fabricated tags.

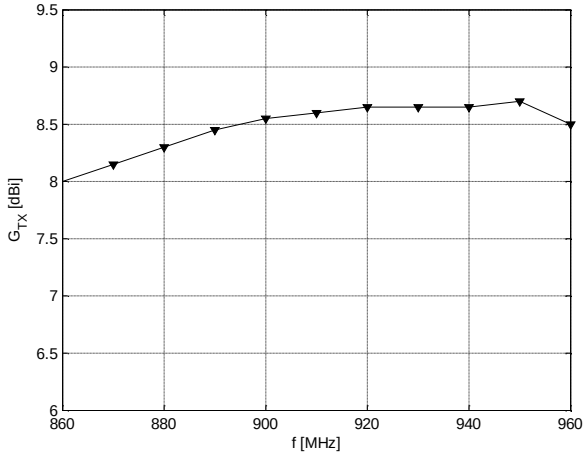

Fig. 8. Gain of the transmitter antenna.

for both the real and imaginary part of the tag antenna impedance in our test tags, with an additional limitation that the standard deviation is not allowed to be lower than 0.5 Ω or higher than 10 Ω. A weak linear correlation coefficient of 0.25 between the real and imaginary part is assumed. Additionally, based on authors' experience, the tag antenna gain is assumed to have a proportional standard deviation of 2% of its mean value on linear scale. The standard deviation for threshold power is obtained through a standard procedure [25] as sample standard deviation from measurement data. It is different for each of the tags and frequencies measured, with typical values of standard deviation ranging from 1 to 2 percent of the sample mean of the measurement result. For each of the k tags measured, we now have frequency dependent parametric pdf estimates $N(\mathbf{x}_k; \boldsymbol{\mu}_k(f), \boldsymbol{\Sigma}_k(f))$.

For the purposes of our simulation, we handle the complex-valued IC impedance as a two-dimensional quantity $Z_L = (R_L, X_L)$. The simulation procedure we have used is summarized in Table IV. On each measured frequency, we draw samples from the pdf estimates and compute for each possible tag pair the sample mean $Z_{ma}(f)$, which gives the expected values of IC impedance, and the sample covariance matrix $\mathbf{C}_m(f)$ to quantify the uncertainty associated with the expected values. In our simulation studies we have used a sample size of S=30000. The method described in Section 2.3, involving a search through all possible solution triplets to identify the physical solution as the triplet spanning the triangle with the minimal circumference in the complex plane is applied to select the most probable solutions for the IC impedance.

Propagating a sample from a normal distribution through the non-linear equations in Section II, results in a non-normal distribution for the IC impedance Z_L [25]. However, as in our studies no significant difference was found between representing Z_L as a normal distribution or with a more complex parametric pdf estimate, such as a Gaussian mixture model (GMM) [23], we shall only consider the normal distribution representation.

B. Impedance Measurement Results

Following the simulation procedure presented in the previous subsection, we compute for both HFSS and FDTD simulation data the sample means and sample standard deviations of each of the selected solution triplets. The results are shown in Figures 9-12.

On each frequency the solution triplet might come from a different row of Table I and therefore the details of the solution triplets are not listed in the figures. In all figures the mean values of the triplets are represented by opaque markers and the corresponding standard deviations are represented by bars.

Figures 9-10 show that the frequency trend of the three resistance solutions is consistent for both simulators. Also, for both simulators, the third resistance solution seems to differ approximately 3 Ω from the other solutions at the lowest measured frequency, but approaches the two other solutions as the frequency increases. From Figs. 11-12 it is seen that for both simulators, the frequency trends are different among the three reactance solutions. The slightly better agreement between the reactance solutions from the different simulators in the middle of the frequency band may be explained by the better agreement of the simulated gains between the different simulators at these frequencies. Also the individual characteristics of the ICs on the test tags may cause variations among the three solutions obtained using the same simulator.

TABLE IV
THE SIMULATION PROCEDURE APPLIED TO ESTIMATE IC IMPEDANCE SOLUTIONS.

1:	For each measured frequency f
2:	For each measured tag k
3:	Draw a random sample $X_{f,k}$ of size S from $N(\mathrm{x}_k; \mu_k(f), \Sigma_k(f))$.
4:	End
5:	For each possible tag combination m
6:	Applying the equations in section II, compute the IC impedances Z_m
7:	Compute sample mean $Z_{ma}(f)$ and sample covariance $C_m(f)$ of the two solutions in Z_m.
8:	End
9:	For each possible solution triplet (see Table 1 for list of all triplets)
10:	Using impedance values from all Z_m, apply the method described in section II to find the most probable solution triplet. Record the sample means and covariances for the selected triplet.
11:	End
12:	End

At each frequency the simulation procedure of Table IV was applied to estimate the parameters of three conditional probability distributions $f_i(Z_L|Y_i)$, where Y_i are the data sets containing all measurement and simulation data related to one row of Table I, indicating the most probable solution triplet. Since on each row of Table I, each tag is present in multiple columns, we can conclude that the data sets Y_i are not independent, from which it follows that the three $f_i(Z_L|Y_i)$ are not independent. To obtain a single mean and covariance parameter on each frequency, we approximate the distributions as independent and apply Bayes' formula [23] to obtain an estimate $g(Z_L|Y_1,Y_2,Y_3)$ of the distribution of the IC's impedance given all data sets Y_i. Since all $f_i(Z_L|Y_i)$ are normal distributions with parameters $\boldsymbol{\mu}_i$ and $\boldsymbol{\Sigma}_i$, $g(Z_L|Y_1,Y_2,Y_3)$ is also a normal distribution with parameters $\boldsymbol{\mu}_t$ and $\boldsymbol{\Sigma}_t$ given by

$$\boldsymbol{\Sigma}_t^{-1} = \boldsymbol{\Sigma}_1^{-1} + \boldsymbol{\Sigma}_2^{-1} + \boldsymbol{\Sigma}_3^{-1} \tag{13}$$

$$\boldsymbol{\mu}_t = \boldsymbol{\Sigma}_t \left(\boldsymbol{\Sigma}_1^{-1}\boldsymbol{\mu}_1 + \boldsymbol{\Sigma}_2^{-1}\boldsymbol{\mu}_2 + \boldsymbol{\Sigma}_3^{-1}\boldsymbol{\mu}_3 \right), \tag{14}$$

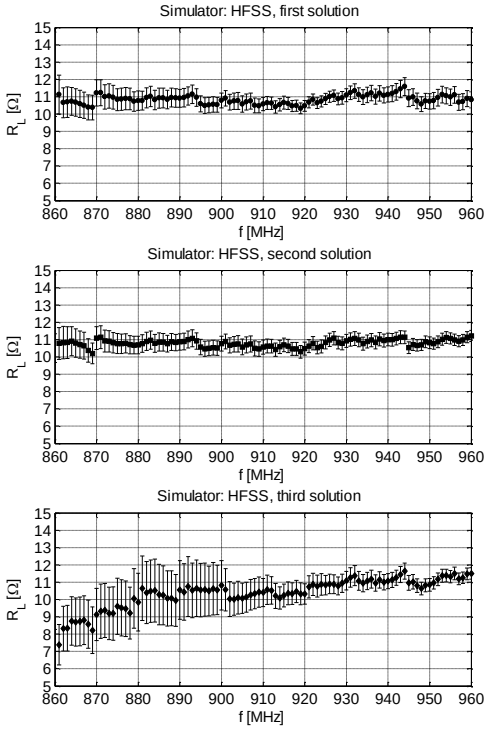

Fig. 9. Sample means with standard deviations of the IC's absorbing state input resistance using the HFSS simulation data.

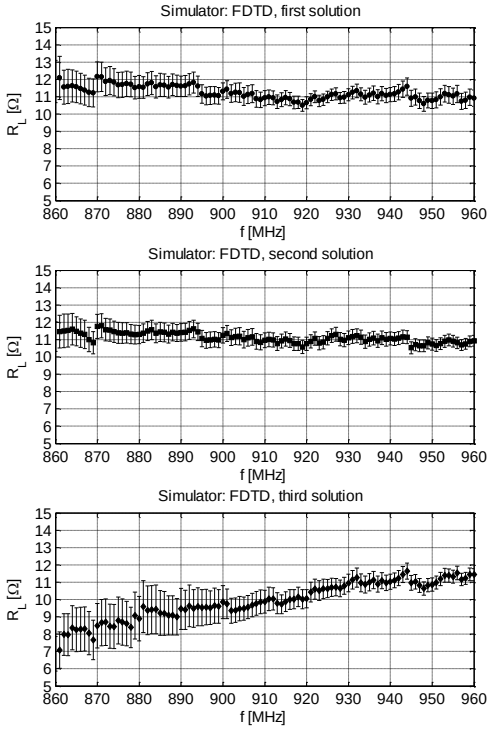

Fig. 10. Sample means with standard deviations of the IC's absorbing state input resistance using the FDTD simulation data.

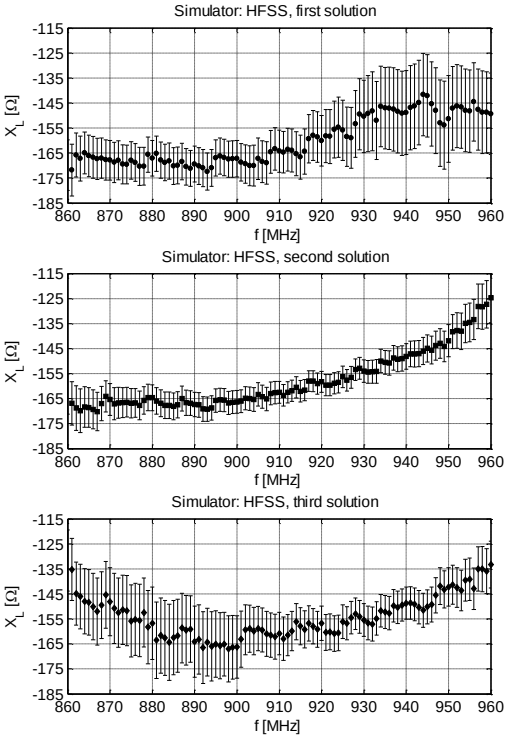

Fig. 11. Sample means with standard deviations of the IC's absorbing state input reactance using the HFSS simulation data.

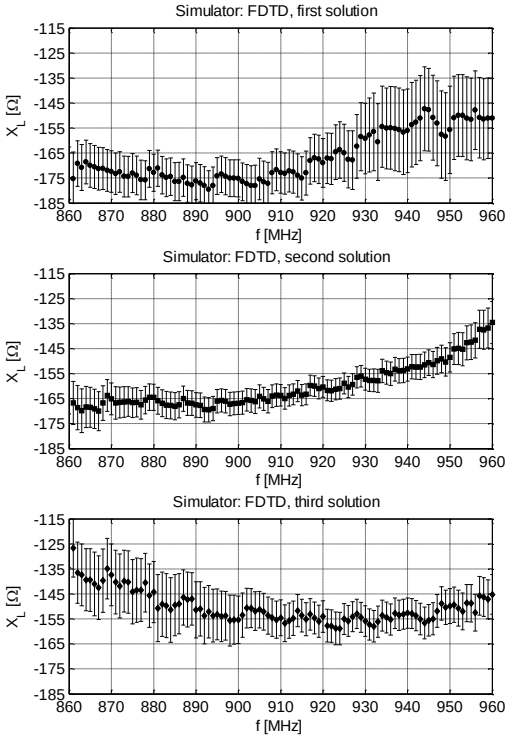

Fig. 12. Sample means with standard deviations of the IC's absorbing state input reactance using the HFSS simulation data.

where $(\cdot)^{-1}$ denotes matrix inversion. Figures 13-16 show the final estimates with one standard deviation limits for the IC's resistance and reactance with both HFSS and FDTD simulation methods. The means are indicated by opaque markers and the one standard deviation limits represented by the bars. The mean values are obtained from equation (14) and the standard deviations from equation (13).

Compared with the FDTD data, the final result with HFSS simulation data shows a steeper rise trend in the reactance after 920 MHz, but both methods predict the local reactance minimum at around 890 MHz. The standard deviations depict the uncertainty of the measured impedance and they are nearly equal using either simulation data. This suggests that the reliability of the proposed measurement method does not depend on the selected CEM tool, as long as the simulation model includes the essential physical details. The results obtained are credible from the physical point of view and indicate that our method is feasible for studying the absorbing state input impedance of an RFID IC.

It should be noted that the equivalent circuit model in the manufacturer's datasheet [20] gives somewhat different values for the input impedance of the measured IC because the circuit model is given at −14 dBm input power, whereas we measured the input impedance at the read sensitivity of the IC, which is −18 dBm. However, as a further assurance, a demonstration of the applicability of the proposed method in a practical design task is presented in the next section.

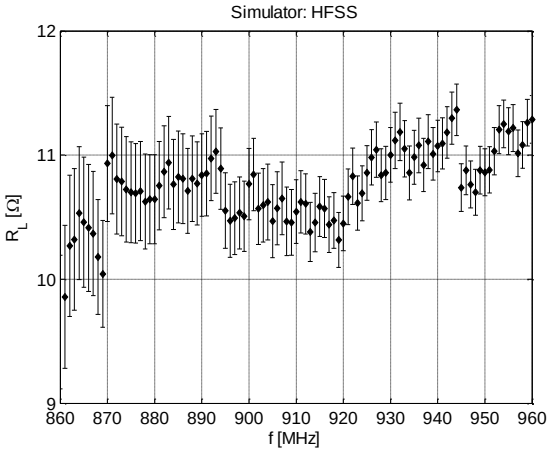

Fig. 13. Mean of the IC's absorbing state input resistance with one standard deviation bars using the HFSS simulation data.

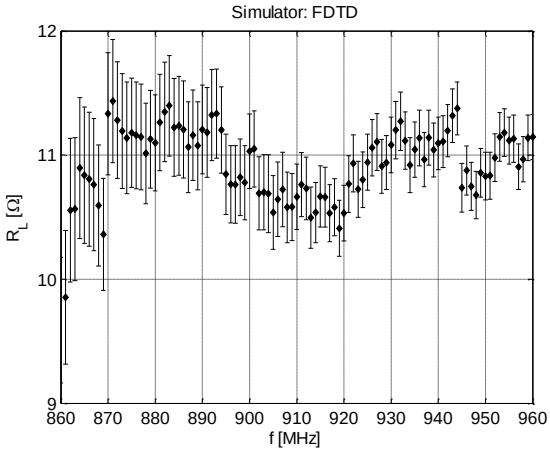

Fig. 14. Mean of the IC's absorbing state input resistance with one standard deviation bars using the FDTD simulation data.

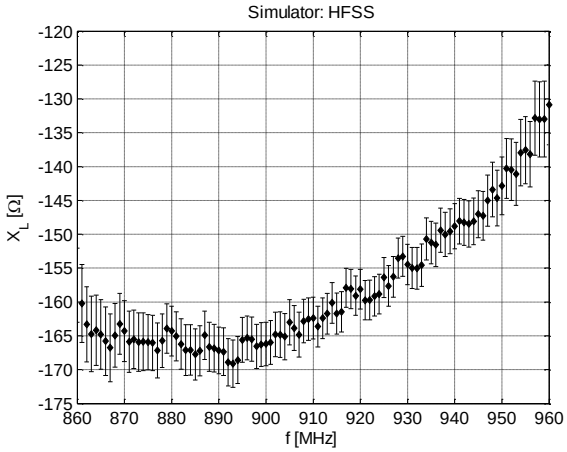

Fig. 15. Mean of the IC's absorbing state input reactance with one standard deviation bars using the HFSS simulation data.

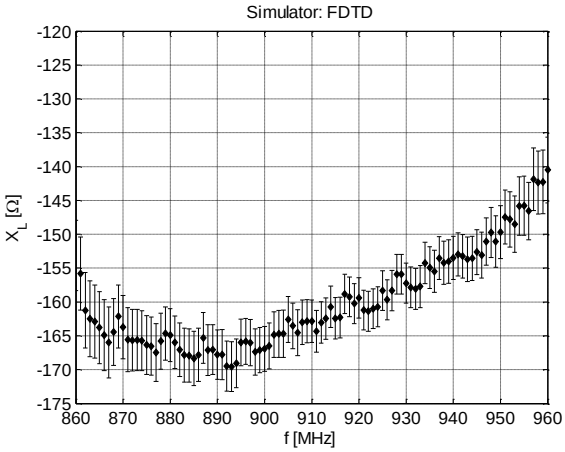

Fig. 16. Mean of the IC's absorbing state input reactance with one standard deviation bars using the FDTD simulation data.

V. Design Example Using the Measured IC Impedance

For a receiving antenna, the realized antenna gain (G_R) describes how much power from an incident electromagnetic plane wave is delivered to the antenna load compared with a lossless perfectly matched isotropic antenna with identical polarization properties. In another words $G_R = G\tau$

The performance of passive RFID tags can be evaluated by analyzing the realized tag antenna gain, since currently the detection range in passive RFID systems is limited by the power delivery to the IC and G_R includes the contributions of both tag properties; the impedance matching and the tag gain, which determine the power delivery from an incident wave to the IC.

In an anechoic measurement environment, the realized gain of a tag antenna can be conveniently approximated by performing a threshold power measurement and solving equation (4) with respect to Gτ. Simulation-based estimate for realized gain is obtained in a straightforward fashion as well, provided that the IC's impedance is known. Whenever this information is available, like in this case from the measurements, τ can be calculated according to the simulated antenna impedance using equation (2) with the antenna as the source and the IC as the load.

To evaluate the applicability of the measured IC impedance in tag antenna design we compared the measured and simulated realized gain of four tags; Tag A, Tag B, Tag C and Tag D, described in Section 3. Tag D was not used in the impedance measurement and thus it serves as an additional comparison tag, which is completely independent of the impedance measurement.

Based on the simulation results presented in Section 3, for the tag antennas considered here, the frequency trend of the realized gain is expected to be dominated by the impedance matching, due to the greater variability of the simulated tag antenna impedance and measured IC impedance compared with the simulated tag antenna gain.

Comparisons between the measured and simulated realized gains of each of the individual tag are presented in Figs. 17-20.

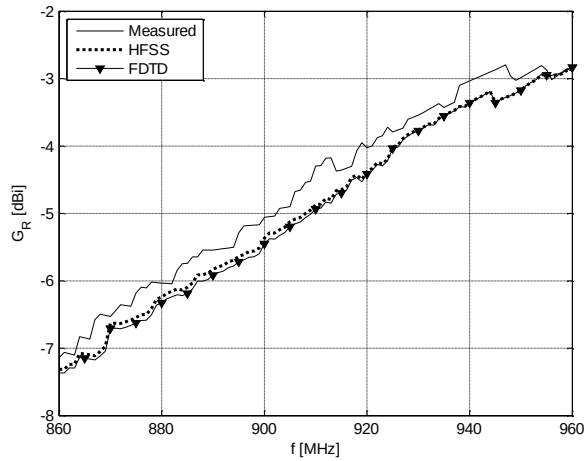

Fig. 17. Measured and simulated realized gain of Tag A.

..

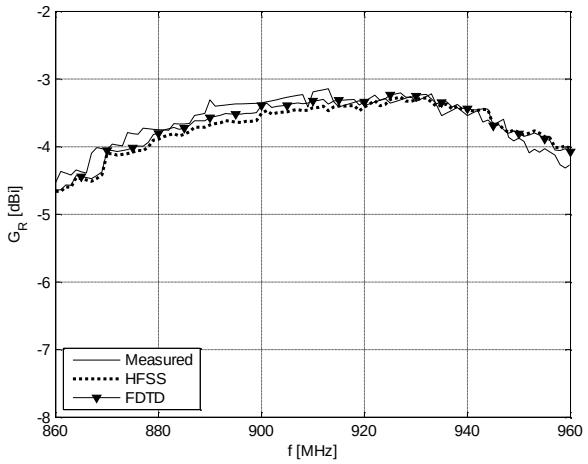

Fig. 18. Measured and simulated realized gain of Tag B.

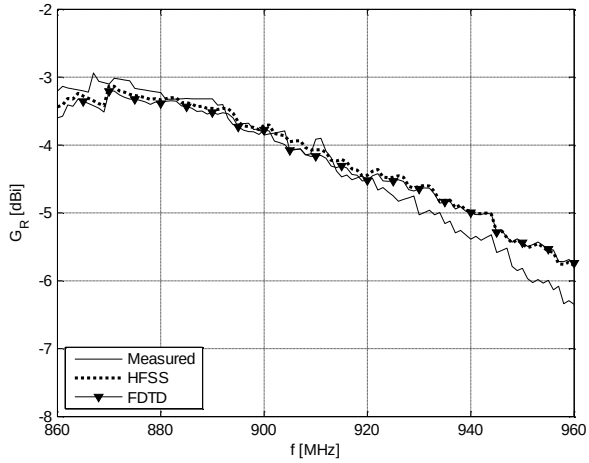

Fig. 19. Measured and simulated realized gain of Tag C.

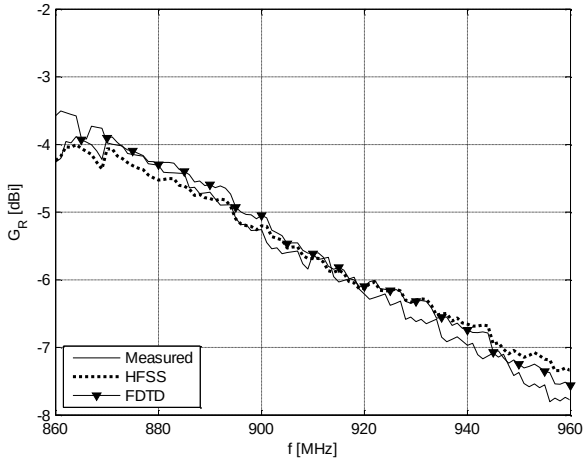

Fig. 20. Measured and simulated realized gain of Tag D.

According to the results shown in Figs. 17-20, there is a maximum 0.5 dB difference between the measured and simulated results (both simulators) for all the test tags over the studied frequency range. The frequency trend of the curves for each tag is predicted well by the simulations where the measured IC impedance was used. This suggests that the frequency dependency of the IC's impedance is captured accurately by our measurements.

As a whole the simulation and measurement results are in very close agreement, particularly for Tag B and Tag D. The slight level shift between the simulation and measurement results for Tag A and Tag C can be due to a small misalignment between the antennas during the measurement.

VI. Conclusions

We have demonstrated a wireless measurement method, based on CEM simulations and threshold power measurement, to determine the absorbing state input impedance of an RFID IC. The presented method takes into account parasitic effects arising from the packaging and the antenna-IC connection and thus provides ready-to-use data for tag antenna designers. Method has been applied to a set of test tags, its uncertainty has been quantified by Monte Carlo simulations and the simulated realized gain of the test tags using the measured IC impedance has been compared against measurement results to demonstrate the degree of accuracy expected from the proposed measurement method. Future work includes further demonstrations of the method by measuring the modulating state input impedance of an RFID IC.

References

[1] D. Dobkin, *The RF in RFID: Passive UHF RFID in Practice*, Newline, 2008.

[2] C. Cho, H. Choo, I. Park, "Broadband RFID tag antenna with quasi-isotropic radiation pattern," *Electronics Letters*, vol. 41, no. 20, pp. 1091-1092, Sept. 2005.

[3] T. Bjorninen, L. Ukkonen, L. Sydanheimo, "Design and non-invasive design verification of a slot-type passive UHF RFID tag," *Proceedings of the 2010 IEEE Radio and Wireless Symposium (RWS)*, pp. 132-135, 10-14 Jan., 2010, New Orleans, LA, USA.

[4] G. Marrocco, "The art of UHF RFID antenna design: impedance-matching and size-reduction techniques," *IEEE Antennas Propag. Mag.*, vol. 50, no. 1, pp. 66-79, Feb. 2008.

[5] S. R. Best, J. D. Morrow, "On the significance of current vector alignment in establishing the resonant frequency of small space-filling wire antennas," *IEEE Antennas Wireless Propag. Lett.*, vol. 2, pp. 201-204, 2003.

[6] A. Harmouch, H. A. Al Sheikh, "Miniaturization of the Folded-Dipole Antenna [Antenna Designer's Notebook]," *IEEE Antennas Propag. Mag.*, vol. 51, no. 1, pp. 117-123, Feb. 2009.

[7] G. De Vita, G. Iannaccone, "Design criteria for the RF section of UHF and microwave passive RFID transponders," *IEEE Trans. Microw. Theory Tech.*, vol. 53, no. 9, pp. 2978-2990, Sept. 2005.

[8] J.-P. Curty, N. Joehl, C. Dehollain, M. J. Declercq, "Remotely powered addressable UHF RFID integrated system," *IEEE J. Solid-State Circuits*, vol. 40, no. 11, pp. 2193- 2202, Nov. 2005.

[9] J. Ryoo, J. Choo, H. Park, J. Hong, J. Lee, "Full Wave Simulation of Flip-Chip Packaging Effects on RFID Transponder," *IEEE International Conference on RFID*, vol., no., pp.37-40, 26-28 Mar. 2007.

[10] U. Karthaus, M. Fischer, "Fully integrated passive UHF RFID transponder IC with 16.7-μW minimum RF input power," *IEEE J. Solid-State Circuits*, vol. 38, no. 10, pp. 1602-1608, Oct. 2003.

[11] C.-H. Loo, K. Elmahgoub, F. Yang, A. Z. Elsherbeni, D. Kajfez, A. A. Kishk, T. Elsherbeni, L. Ukkonen, L. Sydanheimo, M. Kivikoski, S. Merilampi, P. Ruuskanen, "Chip Impedance Matching for UHF RFID Tag Antenna Design," *Progress In Electromagnetics Research, PIER 81*, 359-370, 2008.

[12] P. V. Nikitin, K. V. S. Rao, R. Martinez, S. F. Lam, "Sensitivity and Impedance Measurements of UHF RFID Chips," *IEEE Trans. Microw. Theory Tech.*, vol. 57, no. 5, pp. 1297-1302, May 2009.

[13] Agilent Technologies Inc., "Agilent Impedance Measurement Handbook. A Guide to Measurement Technology and Techniques.", 4th edition, June 2009.

[14] L. W. Mayer, A. L. Scholtz, "Sensitivity and impedance measurements on UHF RFID transponder chips," *Proceedings of The Second International EURASIP Workshop on RFID Technology*, 7-8 July, 2008, Budapest, Hungary.

[15] S.-L. Chen, K.-H. Lin, R. Mittra, "A Measurement Technique for Verifying the Match Condition of Assembled RFID Tags," *IEEE Trans. Instrum. Meas.*, vol. 59, no. 8, pp. 2123-2133, Aug. 2010.

[16] K. Kurokawa, "Power Waves and the Scattering Matrix," *IEEE Trans. Microw. Theory Tech.*, vol. 13, no. 2, pp. 194-202, Mar. 1965.

[17] H. T. Friis, "A Note on a Simple Transmission Formula," *Proc. IRE*, vol. 34, no. 5, pp. 254-256, May 1946.

[18] R. C. Hansen, "Relationships between antennas as scatterers and as radiators," *Proc. IEEE*, vol.77, no. 5, pp. 659-662, May 1989.

[19] P. Pursula, T. Vaha-Heikkila, A. Muller, D. Neculoiu, G. Konstantinidis, A. Oja, J. Tuovinen, "Millimeter-Wave Identification—A New Short-Range Radio System for Low-Power High Data-Rate Applications," *IEEE Trans. Microw. Theory Tech.*, vol.56, no.10, pp.2221-2228, Oct. 2008.

[20] Alien Technology, RFID IC datasheets: http://www.alientechnology.com/tags/rfid_ic.php.

[21] A. Z. Elsherbeni, V. Demir, *The Finite Difference Time Domain Method for Electromagnetics: With MATLAB Simulations*, SciTech Publishing, 2009.

[22] Voyantic Ltd.: http://www.voyantic.com/

[23] C. M. Bishop, *Pattern Recognition and Machine Learning*, Springer, 2006.

[24] L. Mats, J. T. Cain, M. H. Mickle, "Statistical Analysis of Transponder Packaging in UHF RFID Systems," *IEEE Trans. Electron. Packag. Manuf.*, vol. 32, no. 2, pp. 97-105, Apr. 2009.

[25] ISO GUM 95 with minor corrections, JCGM 100:2008 - Evaluation of measurement data – Guide to the expression of uncertainty in measurement. BIPM, IEC, IFCC, ILAC, ISO, IUPAC, IUPAP and OIML. 2008.

Publication IV

T. Björninen, A. Z. Elsherbeni, L. Ukkonen, “Performance of single and double T-matched short dipole tag antennas for UHF RFID systems,” *J. Appl. Computational Electromagn. Soc.*, vol. 26, no. 12, pp. 953-962, Dec. 2011.

Publication V

T. Björninen, A. Z. Elsherbeni, L. Ukkonen, “Low-profile conformal UHF RFID tag antenna for integration with water bottles,” *IEEE Antennas Wireless Propag. Lett.*, vol. 10, no. 1, pp. 1147-1150, Dec. 2011.

Low-Profile Conformal UHF RFID Tag Antenna for Integration with Water Bottles

Toni Björninen, *Member, IEEE*, Atef Z. Elsherbeni, *Fellow IEEE*, and Leena Ukkonen, *Member, IEEE*

***Abstract*—Development of a low-profile and conformal RFID tag antenna with an omnidirectional radiation pattern when mounted on a water bottle is presented. The antenna design and design parameters uncertainty is quantified using numerical simulations. The simulation-based antenna design is verified experimentally for single and multiple tagged bottles configurations.**

***Index Terms*—Radio Frequency Identification (RFID), RFID tag antennas, Conformal antennas, UHF antennas**

I. Introduction

Versatile and energy efficient passive radio-frequency identification (RFID) technology is a strong candidate to replace some of the present automatic identification systems, based on the visual line of sight connection, biometric identification, and tracking assets with active transmitters. The advantages of RFID in asset tracking and supply chain management are already widely recognized [1], but there are still unresolved issues related to the design of cost effective RFID tag antennas for the identification of objects with non-planar surfaces and unfavorable material content for the operation of antennas. However, objects of this type are encountered continually in practical applications of RIFD, such as in the identification of water bottles, and it is therefore crucial to explore cost effective tag antenna solutions further.

The water bottle tag shares the design constraints and requirements with many tags intended for item-level RFID. Due to the very large asset base, the tag manufacturing costs need to be low. For flexibility and reliability, a single tag has to cover the whole global UHF RFID frequency band from 860 MHz to 960 MHz with good spatial coverage (also in the proximity of other tagged objects). Very often the tags also need to be seamlessly integrated with the objects.

The special features in the design of the water bottle tag antenna arise from the water contents of the bottle and the curved bottle surface. Firstly, since water has considerable electrical conductivity and it has high permittivity at the microwave frequencies [2], strong interaction between the water and the tag antenna is to be expected. Secondly, as the radiated field of a current on a cylindrical surface depends on the radius of the cylinder [3], the curved bottle surface need to be accounted for in the design. Neglecting these two design aspects while bending a traditional planar general purpose tag antenna onto the bottle, results in distorted radiation pattern [4] and declined read range due the influence of water on the antenna input characteristics [5]. A conformal antenna array on a cylindrical surface can produce a uniform radiation field in the plane perpendicular to the cylinder axis [6], but considering the tag design constraints discussed above, array configuration may not be a feasible solution in the present application. However, in RFID context, a dielectric resonator tag antenna on a bottle filled with liquids [7] and a dipole tag antenna wrapped around a human arm [8] have been reported providing omnidirectional radiation patterns. This motivated us to further investigate single-element tag antennas for water bottle identification.

The tag antenna prototype presented in this letter is fabricated on a thin flexible platform for seamless integration with a bottle. The tag performance is characterized with the antenna conductor facing the bottle surface, in order to better understand the expected performance in a scenario where the tag is manufactured directly onto the bottle or in the backside of an ordinary product label.

II. Tag Antenna Design

The design process outlined in this section is based on finite element method (FEM) simulations using ANSYS high frequency structure simulator (HFSS) [9]. To account for the influence of water on the antenna, a co-design approach, where the water bottle is considered as part of the antenna, was taken. The material parameters used for water at 1 GHz and temperature of 20 C° are σ_{water}=0.267 S/m and $\varepsilon_{r,water}$=79.2 as reported in [2]. Other materials included in the simulation model are the bottle plastic and the antenna platform material. Relative permittivities of $\varepsilon_{r,bottle}$=2.19 and $\varepsilon_{r,platform}$=3.18 were measured over the frequency range from 800 MHz to 1 GHz for these materials with Agilent VNA E8358A, using Agilent 85070E dielectric probe kit. In the simulations, both the plastic bottle and the antenna platform were modeled as low loss

Manuscript received August 17, 2011. This research work was funded by the Finnish Funding Agency for Technology and Innovation (TEKES), Academy of Finland, Centennial Foundation of Finnish Technology Industries, Tampere Doctoral Programme in Information Science and Engineering (TISE), HPY Research Foundation, Nokia Foundation, and Ulla Tuominen Foundation.

T. Björninen and L. Ukkonen are with the Department of Electronics, Tampere University of Technology, Rauma, Finland (toni.bjorninen@tut.fi).

Atef Z. Elsherbeni is with the Department of Electrical Engineering, University of Mississippi, University, USA (atef@olemiss.edu).

dielectrics with a loss tangent of 0.005.

An important initial observation that steered the design towards the prototype presented below was that by bending a center-fed dipole antenna onto a plastic cylinder ($\varepsilon_{r,bottle}$=2.19) filled with water, the nulls from the dipole E-plane radiation pattern can be removed by an appropriate choice of the dipole length. Another key-observation was that with a fixed dipole length, which provided the omnidirectional pattern, the best radiation efficiency (e_r) is achieved with a narrow dipole width. These two observations are exemplified in Fig. 1.

Based on these observations, modifications of the simple straight dipole were investigated in order to achieve the omnidirectional radiation pattern simultaneously with good conjugate impedance matching between the tag antenna and the IC. Here, the parameters of interest are the tag antenna gain pattern (G_{tag}) in xy-plane of Fig. 1, radiation efficiency, and power transmission coefficient (τ) given by

$$\tau = \frac{4\,\mathrm{Re}(Z_{tag})\mathrm{Re}(Z_{ic})}{\left|Z_{tag}+Z_{ic}\right|^2}, \qquad (1)$$

where Z_{tag} and Z_{ic}, are the tag antenna and IC impedance, respectively. The power transmission coefficient indicates how many percentage of the available power from the antenna is delivered to the tag IC [10]. The prototype tag is equipped with Higgs-3 EPC Generation 2 UHF RFID IC by Alien Technology [11]. The measured tag IC impedance at the wake-up power of the IC reported in [12] was used in the design.

In the present application, the achievable radiation efficiency of the antenna on the bottle is severely limited by the presence of the water. A folded dipole antenna, while in the vicinity of a bottle filled with water, can potentially have high input impedance compared to that of a straight dipole of the same length [4][13]. The antenna input impedance plays a major role in its radiation efficiency. Moreover, to be able to easily wrap the tag antenna onto the bottle, the antenna footprint size is limited to approximately that of an ordinary paper product label placed on the smooth cylindrical section of the bottle. Since the achievable radiation efficiency is proportional to the electrical size of the antenna, it is best to try to make use of the available space as much as possible. Taking into account that increasing the width of a straight dipole beyond 1 mm did not increase the radiation efficiency in the initial studies (see Fig. 1), the selection of the prototype antenna geometry converged to a three-wire antenna with up to 3 mm trace width, occupying the area of an ordinary product label. Further simulations showed that open-circuiting the two folded dipole arms in the middle and bending them inward is favorable for achieving higher radiation efficiency, with minor effects on the other antenna properties. Thus the impedance matching and final tuning of the antenna shape was based on the antenna geometry shown in Fig. 2.

As shown in the cross-sectional view in Fig. 2, the antenna prototype consists of copper trace on a plastic platform, which is then wrapped onto the outer surface of the bottle. However, to achieve potential material savings by eliminating the need

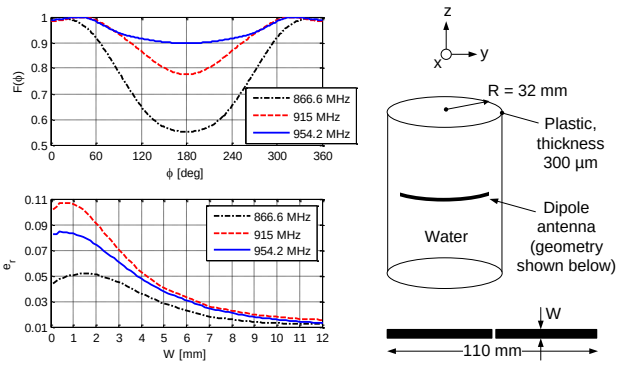

Fig. 1. Top left: simulated normalized (to the maximum value over all spatial directions) power pattern of a dipole with W=1 mm in the xy plane. Bottom left: simulated radiation efficiency of the dipole versus the dipole width.

for an additional antenna platform, pad printing technique [14] could be used to print the antenna directly onto the bottle surface using conductive thick film ink. Alternatively, as the narrow antenna trace was found favorable in this application, the antenna shape is well-suited for fabrication with inkjet printing [15] in the backside of an ordinary paper product label.

The impedance matching between the tag antenna and the tag IC was performed with the T-matching approach based on shorting the antenna terminals near the tag IC with a conducting loop. In this way, the input impedance of a short dipole can be made from capacitive to inductive and the input reactance of the fixed-length T-matched antenna is controlled by the shape of the shorting loop [10].

To preserve the symmetry of the antenna structure, the T-matching loop was placed on both sides of the tag IC. Finally, the built-in genetic optimizer of the HFSS version 12 was employed to optimize the antenna gain pattern and the power transmission coefficient in the global UHF RFID band. The simulation model and the associated parameters are shown in Fig. 2 and the numerical values of these parameters are listed in Table I. The optimization was done first for parameters *a*, *b* and *w* to achieve an omnidirectional pattern with maximal radiation efficiency and afterwards for parameters *u* and *v* to arrange for good conjugate impedance matching with the tag IC.

In empty space the read range of a passive UHF RFID tag is

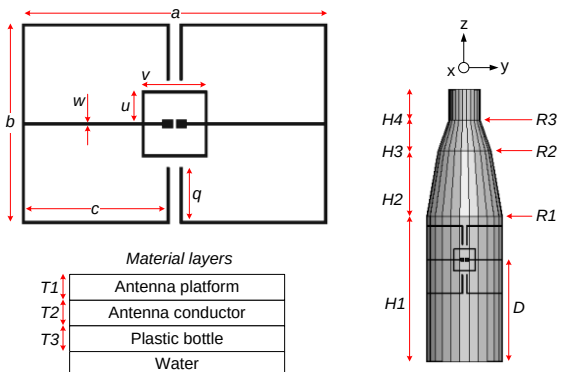

Fig. 2. The simulation model and the associated parameters.

TABLE I

VALUES OF THE MODEL PARAMETERS IN MILLIMETERS.

a	*b*	*c*	*u*	*v*	*w*	*D*
87.8	57.9	41.9	9.2	18.9	0.75	86.5
q	*H1*	*H2*	*H3*	*H4*	*R1*	*R2*
15.6	123	56	26	26	32	22.3
R3	*T1*	*T2*	*T3*			
13.3	0.125	0.025	0.3			

TABLE II

THE DESIGN FREQUENCIES AND THE CORRESPONDING EIRP VALUES.

Region	EU	US	Japan
f [MHz]	865.6-867.6	902-928	952-956.4
EIRP [W]	3.28	4	4

typically limited by the reader-to-tag link, since the power required for activating the tag IC is orders of magnitude larger than the weakest tag signal that can be detected at the reader. As the transmitted power is limited by the regulated EIRP (see Table II), the performance of this link is determined by the realized tag antenna gain, given by $G_{r,tag}=\tau G_{tag}$. The effective aperture of the tag antenna ($A_{e,tag}$) and thereby the delivered power to the tag IC (P_{ic}) are also determined by the realized tag antenna gain through

$$\tau A_{e,tag}=\frac{\lambda^2 G_{r,tag}}{4\pi},\quad P_{ic}=\tau\chi_{pol}A_{e,tag}S_{inc}, \tag{2}$$

where χ_{pol} is the polarization mismatch factor between the tag and reader antenna and S_{inc} is the incident power density at the tag's location. An estimate for the tag read range from (2) is:

$$d_{tag}=\frac{\lambda}{4\pi}\sqrt{\frac{\chi_{pol}G_{r,tag}\mathrm{EIRP}}{P_{ic,0}}}, \tag{3}$$

where $P_{ic,0}$ is the wake-up power of the tag IC.

To evaluate d_{tag} using the simulated tag antenna properties, τ given in equation (1), was first calculated using the IC impedance data from [12] and the simulated tag antenna impedance. The realized tag antenna gain was then calculated using the simulated tag antenna gains and power transmission coefficients listed in Table III. Finally, the tag read range is determined using the −18 dBm tag IC wake-up power reported by the manufacturer and assuming good polarization alignment (χ_{pol}=1).

Simulation results in Fig. 3 clarify the effect of bending and poximity of water on the tag antenna radiation pattern. The high dielectric constant of water helps to remove the deep nulls seen in the patterns without the water bottle. The co-design approach where the bottle is considered as a part of the antenna during the optimization process, provides further improvement. The corresponding read range patterns are shown in Fig 4. This figure includes also the uncertainty envelopes corresponding to one standard deviation uncertainty

TABLE III

SUMMARY OF THE ANTENNA DESIGN DATA. GAIN VALUE IS GIVEN IN THE DIRECTION OF THE POSITIVE X-AXIS IN FIG. 2.

f [MHz]	Z_{tag} [Ω]	Z_{ic} [Ω]	τ	e_r	G_{tag} [dBi]
866.6	14+*j*166	11−*j*164	0.98	0.065	−9.7
915	22+*j*205	11−*j*162	0.34	0.076	−10.8
954.2	42+*j*236	11−*j*146	0.17	0.079	−10.3

reported for the measured tag IC resistance and reactance [12], and maximum 5% variation in the simulated tag antenna resistance, reactance, and gain.

III. MEASUREMENTS AND DISCUSSION

A power ramping method was used to evaluate the tag read range experimentally. For this purpose, EPC Generation 2 *query* command (to which the tag replies with its identification code) was sent to the tag under test, while illuminating it with a decreasing carrier power density. The measured quantity was the threshold power (P_{th}), the minimum transmitted carrier power, which enables a valid response from the tag. During the measurement the reader and tag antennas were aligned to minimize the polarization loss (χ_{pol}=1). The measurement was conducted in a compact anechoic chamber with Voyantic Tagformance Lite measurement device [16], which is a measurement unit for RFID tag performance characterization. It allows power ramping at a defined frequency and thereby the threshold power analysis. The measurement environment was also characterized in terms of the measured pathloss (L_{fwd}) from the generator's output port to the input port of an equivalent isotropic antenna placed at the tag's location using the device calibration procedure. In this way, the effect of possible multipath propagation is further suppressed. Using these measured data, the tag read range is then calculated with

$$d_{tag}=\frac{\lambda}{4\pi}\sqrt{\frac{\mathrm{EIRP}}{L_{fwd}P_{th}}}. \tag{4}$$

In practical applications several tagged bottles are likely to be placed close to each other. Therefore, configurations with

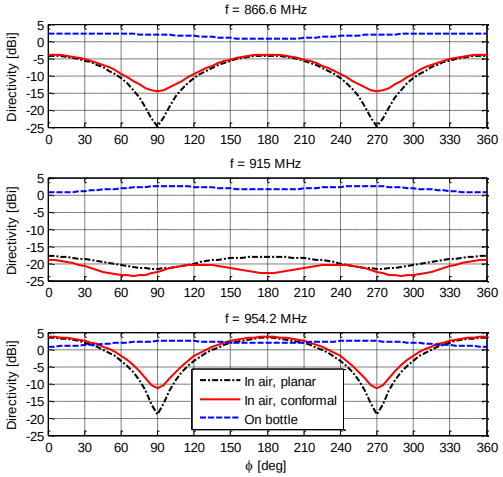

Fig. 3. Simulated tag antenna directivity the xy plane in Fig. 2.

four tagged bottles were studied as shown in Fig. 5. These configurations are symmetric w.r.t. individual tags and thus P_{th} was measured for only one tag.

The measured and simulated tag read ranges shown in Fig. 4 verify the simulation-based design within the expected limits of uncertainty at 915 MHz and for the majority of the measured directions at 954.2 MHz (the measured result is contained in the uncertainty envelope around the simulation result). At 866.6 MHz the simulation result is slightly too optimistic, but despite the level-shift between the measured and simulated curves, their angular responses agree fairly well. Overall, these results indicate that the simulation-based design was successful and the developed simulation model predicts correctly the desired uniform radiation around the bottle with the antenna occupying less than half of the bottle circumference. Most importantly, the measured results in Fig. 4 show that the tag read range around the bottle is more than two meters which is sufficient for the considered application.

The experimentation with the multi-bottle configurations shows that although the other near-by tagged bottles affect the tag antenna radiation pattern, dead zones did not emerge in either of the studied configurations, as seen from Fig. 6. In particular, the performance of configuration 2 of Fig. 5, where the measured tag is in physical contact with two other tag antennas and surrounded by the water from all sides, is still reasonable with above one meter minimum read range at all the measured frequencies.

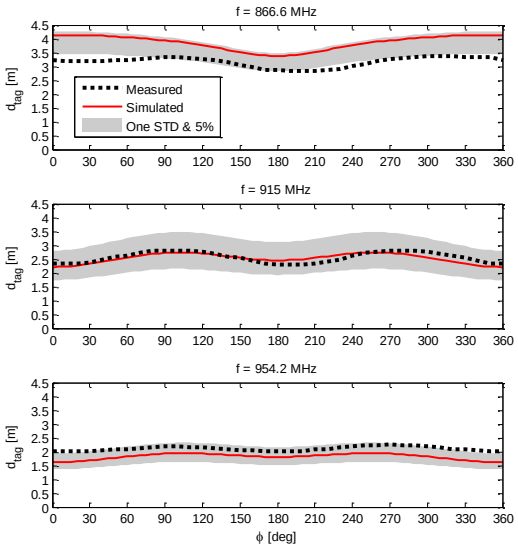

Fig. 4. Simulated and measured read range patterns of the tag in the xy plane in Fig. 2, and the associated uncertainty envelopes.

IV. Conclusions

The development and experimental verifications of a low-profile and conformal tag antenna for identification of water bottles with passive UHF RFID has been discussed. The developed tag antenna does not contain any material layer between the tag antenna conductor and the bottle and it could therefore be directly manufactured onto the bottle or printed in the backside of an ordinary paper product label for seamless integration with the bottle.

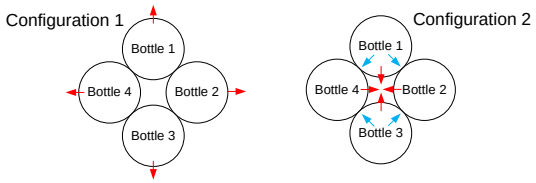

Fig. 5. Cross-section of the multi-bottle measurement configurations. Red arrows show where the tags are facing. Blue arrows indicate regions where the tags are in physical contact with each other.

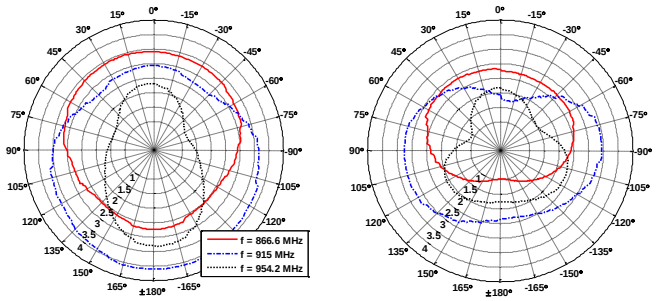

Fig. 6. Measured tag read range in the multi-bottle measurement configurations shown in Fig. 5. Left: Configuration 1, right: Configuration 2.

V. References

[1] K. Michael and J. McCathie, "The Pros and Cons of RFID in Supply Chain Management," *International Conference on Mobile Business*, pp. 623-629, July 11-13 2005, Sydney, Australia.

[2] W. J. Ellison, K. Lamkaouchi, and J.-M. Moreau, "Water: a dielectric reference," *Journal of Molecular Liquids*, vol. 68, no. 2-3, pp. 171-279, Apr. 1996.

[3] R. F. Harrington, *Time-Harmonic Electromagnetic Fields (An IEEE Press Classic Reissue)*, IEEE Press, 2001.

[4] P. R. Foster and R. A. Burberry, "Antenna Problems in RFID Systems," *IEE Colloquium on RFID Technology*, pp. 3/1-3/5, Oct. 25th 1999, London, UK.

[5] D. M. Dobkin and S. M. Weigand, "Environmental Effects on RFID Tag Antennas," *IEEE International Microwave Symposium*, pp. 135-138, June 12-17 2005, Long Beach, CA, USA.

[6] L. Josefsson and P. Persson, *Conformal Array Antenna Theory and Design*, IEEE Press, 2006.

[7] H. A. Malhat, S. H. Zaiud-Deen, and K. H. Awadalla, "Curved Dual-Band Dielectric Resonator Tag Antenna for RFID Applications," *International Journal of Radio Frequency Identification and Wireless Sensor Networks*, vol. 1., no. 1, pp. 9-21, June 2011.

[8] E H. Rajagopalan and Y. Rahmat-Samii, "Platform Tolerant and Conformal RFID Tag Antenna: Design, Construction and Measurements," *Journal of Applied Computational Electromagnetics Society (ACES)*, vol. 25, no. 6, pp. 486-497, June 2010.

[9] ANSYS Inc., Canonsburg, PA, USA: http://www.ansys.com/

[10] G. Marrocco, "The art of UHF RFID antenna design: impedance-matching and size-reduction techniques," IEEE Antennas Propag. Mag., vol. 50, no. 1, pp. 66-79, Feb. 2008.

[11] Alien Technology, Morgan Hill, CA, USA: http://www.alientechnology.com/

[12] T. Björninen, M. Lauri, L. Ukkonen, R. Ritala, A. Z. Elsherbeni, and L. Sydänheimo, "Wireless Measurement of RFID IC Impedance," *IEEE Trans. Instrum. Meas.*, vol. 60, no. 9, pp. 3194-3206, Sept. 2011.

[13] W. L. Stutzman and G. A. Thiele, *Antenna Theory and Design*, John Wiley & Sons, Inc., 1981.

[14] S. Merilampi, T. Björninen, L. Ukkonen, P. Ruuskanen, and L. Sydänheimo, "Characterization of UHF RFID tags fabricated directly on convex surfaces by pad printing," *Int. J. Adv. Manuf. Tech.*, vol. 53, no. 5, pp. 577-591, Mar. 2011.

[15] J. Virtanen, T. Björninen, L. Ukkonen, and L. Sydänheimo, "Passive UHF Inkjet-Printed Narrow-Line RFID Tags," *IEEE Antennas Wireless Propag. Lett.*, vol. 9, pp. 440-443, 2010.

[16] Voyantic Ltd., Espoo, Finland: http://www.voyantic.com/

Publication VI

T. Björninen, K. Espejo Delzo, L. Ukkonen, A. Z. Elsherbeni, L. Sydänheimo, “Long range metal mountable tag antenna for passive UHF RFID systems,” *Proc. IEEE RFID-TA Int. Conf.*, pp. 194-198, 15-16 Sept. 2011, Sitges, Spain.

Long Range Metal Mountable Tag Antenna for Passive UHF RFID Systems

Toni Björninen, *Member, IEEE*, Karina Espejo Delzo, Leena Ukkonen, *Member, IEEE*, Atef Z. Elsherbeni, *Fellow, IEEE*, and Lauri Sydänheimo, *Member, IEEE*

***Abstract*—Development of a long range platform tolerant metal mountable patch-type tag antenna for passive ultra high frequency (UHF) radio frequency identification (RFID) systems is discussed. Results from full-wave electromagnetic simulations are presented to explain the design procedure and to evaluate the performance of the prototype tag antenna. The design uncertainty is quantified based on the expected maximum variations in the tag antenna and tag chip impedance. Wireless RFID measurements based on the EPC Generation 2 protocol are used in experimental tag design verification. The prototype tag achieves 25-meter maximum theoretical line of sight read range on metallic objects at 915 MHz.**

I. Introduction

Passive radio frequency identification (RFID) technology based on electromagnetic interaction between reader and RFID tags has potential to overcome many of the limitations of the present automatic identification systems based on e.g., bar-code technology, machine-vision, biometric identification, or using active transmitters to track assets. Despite being relatively low-power devices with operation based on energy-scavenging, presently the detection range of the general purpose low-cost tags can extend beyond 10 m line of sight distance.

The fundamental limitations on the performance of RFID tags are set by the sensitivity of the on-tag RFID IC and performance of the tag antenna, which is responsible for the energy scavenging and establishing the wireless communication link with the reader. The operation of antennas is affected by the electromagnetic properties of materials in contact or in the vicinity of the antenna conductor. In particular, when a tag antenna is placed near a conducting surface, a strong image current is created in the conducting surface. This results in the degradation of the radiation efficiency of the antenna. In addition, the separation from a metal surface, even a one with a small size, can significantly affect the tag antenna radiation pattern and input impedance [1-2].

Objects with a conducting surface or metallic contents are however encountered continually in practical applications and it is therefore important to explore tag antenna design approaches further to guarantee reliable identification for these objects as well. One of the key-issues of the design is the trade-off between the antenna height and the on-metal performance. For example, a 3.4-meter line of sight on-metal read range is achieved with a meandered patch-type tag antenna with the height of 0.8 mm [3] and a 15-meter line of sight on-metal read range is achieved with a normal mode helical antenna with the total antenna height of 4 mm [4]. In addition, the overall footprint of the tag antenna design affects its performance [5]. The tag antenna design discussed in this article demonstrates a solution with the total height of 3.3 mm and a 25-meter theoretical line of sight read range on metal. The overall footprint of the presented antenna design with substrate and ground plane is 68 mm x 131 mm.

II. Tag Antenna Design

A. Concept and Requirements

Tag antennas with high performance when mounted on a metallic surface are needed in industrial asset management, for example in the identification of cargo containers and machinery. In addition, identification of moving vehicles for example in road tolls and parking garages and identification of railroad cars are also potential applications for metal mountable tags. In these applications, patch-type tag antennas have the advantage of having rugged structure. In addition, the ground plane included in the antenna provides platform tolerance. Patch-type tag antennas have high gain compared to omnidirectional tag antennas, such as dipoles and slots. This allows much longer read range for the tag. With the present passive RFID technology the line of sight read range of patch tags can extend beyond 20 meters.

The tag antenna design presented in this paper was inspired by the metal mountable patch-type tag antenna presented in [6]. Instead of using the inset feed with additional tuning stubs to match the tag antenna to a capacitive tag chip as in [6], the proposed design employs an inductive feed network composed of narrow grounding strips.

Manuscript received February 28, 2011. This research work was funded by the Finnish Funding Agency for Technology and Innovation (TEKES), Academy of Finland, Centennial Foundation of Finnish Technology Industries, Tampere Doctoral Programme in Information Science and Engineering (TISE), HPY Research Foundation, and Nokia Foundation.

Toni Björninen, Leena Ukkonen, and Lauri Sydänheimo are with the Rauma Research Unit of Department of Electronics at Tampere University of Technology, 26100 Rauma, Finland (phone: +358-44-534-1510; e-mail: toni.bjorninen@tut.fi). Karina Espejo Delzo was with the Rauma Research Unit of Department of Electronics at Tampere University of Technology, 26100 Rauma, Finland.

Atef Z. Elsherbeni is with the Department of Electrical Engineering at The University of Mississippi University, MS 38677, USA.

B. *Design Process and Simulation Results*

The design process outlined in this section is based on the finite element method (FEM) simulations with Ansoft's High Frequency Structure Simulator (HFSS). The simulated antenna structure is composed of a rectangular patch element placed on a 3.175 mm thick Rogers RT/Duroid 5880 dielectric substrate with the relative permittivity of 2.2 and loss tangent of 0.0009. The patch is connected directly to one of the chip terminals. The other terminal is connected to the ground plane via three narrow traces crossing over the substrate edges. The ground plane reduces the influence of the materials behind it on the antenna performance. To reduce the interaction of the fringing field at the patch edges with the metallic object behind the tag antenna, the substrate and ground plane are extended beyond the patch edges. Finally, to guarantee maximal tag antenna performance on a metallic object, all the simulations were done with a 20-by-20 cm copper sheet placed behind the tag antenna ground plane. The simulated antenna geometry and the associated parameter values are shown in Fig. 1. The parameter values to describe the geometry of the final tag antenna design are listed at Table I.

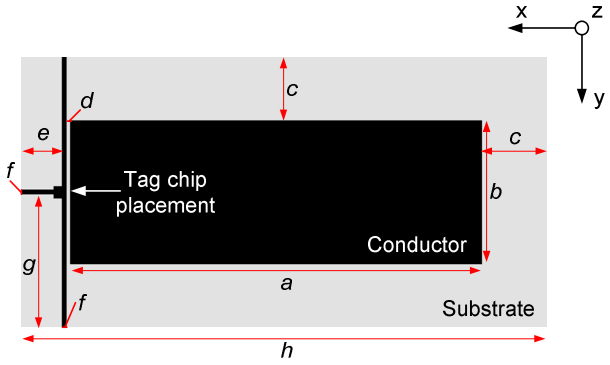

Fig. 1. Tag antenna geometry and the related model parameters

The directivity of the tag antenna is determined by the patch size (parameters a and b in Fig. 1). Sufficient separation between the patch and the substrate edges (parameter c in Fig.1) was found after initial simulations. The gap between the patch and the grounding strips (parameter d in Fig. 1) was set to 1 mm to facilitate the tag chip attachment. With these parameters fixed, the input impedance of the tag antenna is controlled by the width of the grounding strips (parameter f in Fig.1) and the length of the x-directed grounding strip (parameter e in Fig. 1), which both affect the inductance of the ground connection.

TABLE I
VALUES OF THE MODEL PARAMETERS IN MILLIMETERS

a	b	c	d	e	f	g	h
102.75	36	16	1	10.5	1	33.5	131.25

Following the steps outlined above, the shape of the patch and the grounding strips were tuned to maximize the tag antenna performance when it is placed on a 20-by-20 cm copper sheet. The built-in genetic algorithm in HFSS version 12 was employed in this process. The design metrics used was the theoretical maximum line of sight read range (d_{tag}) in the forward direction (the direction of the positive z-axis in Fig. 1) given by

$$d_{tag} = \frac{\lambda}{4\pi}\sqrt{\frac{\tau G_{tag}\,\mathrm{EIRP}}{P_{ic,0}}}, \quad \text{with} \quad \tau = \frac{4\,\mathrm{Re}(Z_{tag})\mathrm{Re}(Z_{ic})}{\left|Z_{tag}+Z_{ic}\right|^2}, \qquad (1)$$

where G_{tag} is the tag antenna gain in the forward direction, EIRP is the equivalent isotropically radiated power (limited by the radio regulations), and τ is the power transmission coefficient between the tag antenna and tag chip impedances Z_{tag} and Z_{ic}, respectively. The prototype tag is equipped with the Higgs-3 EPC Generation 2 UHF RFID IC by Alien Technology with read sensitivity $P_{ic,0}$=−18 dBm and impedance at the chip sensitivity level measured in [7]. The design frequency is 915 MHz, the center frequency of the US RFID band with EIRP=4 W [8].

The tag read range is a very descriptive design metrics, but since the EIRP in (1) is only defined at certain frequencies, the realized tag antenna gain, given by $G_{r,tag}=\tau G_{tag}$, is a preferred quantity for purposes of experimental tag design verification. It is a fundamental tag performance quantity, which combines the radiation properties of the tag antenna with the impedance matching. The effective aperture of the tag antenna ($A_{e,tag}$) and thereby the delivered power to the tag chip (P_{ic}) are also determined by the realized tag antenna gain through

$$\tau A_{e,tag} = \frac{\lambda^2 G_{r,tag}}{4\pi}, \quad P_{ic} = \tau A_{e,tag} S_{inc}, \qquad (2)$$

where S_{inc} is the incident power density at the tag's location.

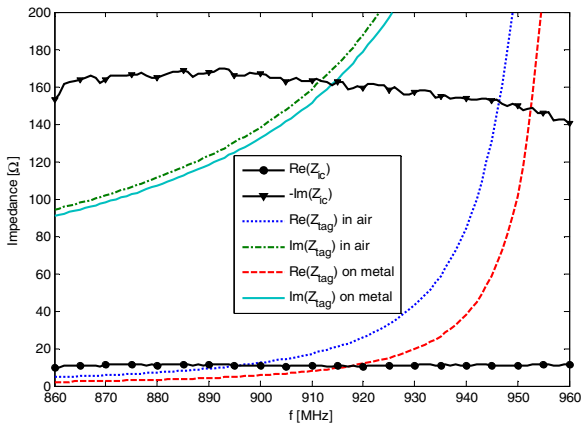

Fig. 2. Simulated antenna impedance and the conjugate of the tag chip impedance [7].

The simulated tag antenna impedance in air and on metal as well the conjugate of the tag chip impedance obtained in [7] are shown in Fig. 2. These quantities determine the power transmission coefficient (τ) in (1). The maximum radiation intensity of the tag antenna is in the forward direction and the values of the simulated radiation properties in this direction are summarized in Table II. In addition, the

TABLE II
SIMULATED PERFROMANCE OF THE TAG ANTENNA IN THE FORWARD DIRECTION AT 915 MHZ.

	D [dBi]	e_r	G_{tag} [dBi]	τ	$G_{r,tag}$ [dBi]
In the air	5.5	0.95	5.3	0.82	4.5
On metal	7.2	0.89	6.7	0.99	6.7

tag antenna is linearly polarized with predominantly *x*-directed current in the patch element.

For comparison between the simulated and measured frequency response of the tag, the simulated realized tag antenna gain for 860 MHz to 960 MHz frequency range is presented in Fig. 3. Figure 4 shows the simulated maximum line of sight tag read range patterns in two orthogonal plane cuts, both in air and on metal. The results in Figs. 3-4 include also an uncertainty envelope corresponding to one standard deviation (STD) uncertainty in tag chip resistance and reactance obtained in [7], combined with a maximum 5% error in the simulated tag antenna resistance and

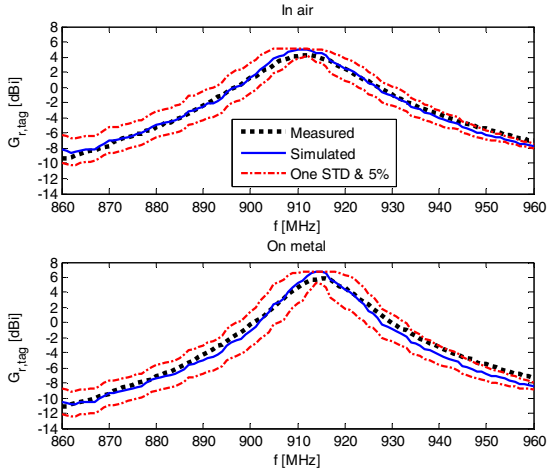

Fig. 3. Simulated and measured realized tag antenna gain in the forward direction and the associated uncertainty envelope.

reactance. The uncertainty envelope helps to quantify the design uncertainty.

III. TAG MEASUREMENTS AND DISCUSSION

The direct measurement of the tag read range by taking the tag farther away from the reader antenna until its response stops is sensitive to the contributions of multipath propagation. By conducting this measurement in an anechoic chamber the multipath can be suppressed, but since the anechoic chambers are often limited in size, an alternative method based on ramping of the transmitted power is advantageous. This method provides higher repeatability and accuracy, since neither the tag nor the reader antenna needs to be moved during the measurement. However, this measurement describes the theoretical maximum read range of the tag. Read range in the real application environment is dependent on many factors, such as reader equipment and multipath propagation. Theoretical maximum read range, however, helps to compare the performance of different tags and gives reliable guidelines on the performance of the measured tag.

To obtain the theoretical maximum read range and the realized gain of the tag antenna using the power ramping method, the EPC Generation 2 *query* command (to which the tag replies with its identification code) was sent to the tag under test with gradually decreasing carrier power density with defined power steps. With this method, the measured quantity was threshold power (P_{th}), defined as the minimum transmitted power which enables a valid response from the tag.

The measurement was conducted in a compact anechoic chamber with Tagformance© measurement device, which is a measurement unit for RFID tag performance characterization. It allows power ramping at a defined frequency and thereby threshold power analysis. The core operations of the device are performed with a vector signal analyzer. Using a calibration tag provided by the device manufacturer, the measurement environment was also characterized in terms of the measured pathloss (L_{fwd}) from the generator's output port to the input port of a hypothetic isotropic antenna placed at the tag's location. With this procedure, any possible multipath propagation in the measurement environment is further suppressed. Using these measured data, the realized tag antenna gain ($G_{r,tag}$) and the maximum line of sight read range (d_{tag}) are calculated with

$$G_{r,tag} = \frac{P_{ic,0}}{L_{fwd} P_{th}} \quad \text{and} \quad d_{tag} = \frac{\lambda}{4\pi}\sqrt{\frac{EIRP}{L_{fwd} P_{th}}}. \qquad (3)$$

These quantities are presented in Figs. 3 and 4, respectively, together with the corresponding simulation results and the uncertainty envelopes associated with the simulations.

As seen from Fig. 3, the simulated and measured realized tag antenna gain in the forward direction agree well within the studied frequency range and for the majority of the frequency points, the measured value remains within the uncertainty envelope based on the maximum expected tag chip and tag antenna impedance variations. This verifies the simulated frequency response of the tag and adds further assurance to the analysis and comparison of obtained results.

In air, the measured realized tag antenna gain peaks at 912 MHz with maximum value of 5 dBi. When the tag is placed on a metal surface, the peak value 6.7 dBi is achieved at the design frequency, 915 MHz. This shows that the simulation based design with the copper sheet behind the tag antenna was successful and that the tag is platform tolerant. At 915 MHz, the measured realized gain value is around 1 dB lower than the simulated value, both in the air and on metal. As the power transmission coefficient is sensitive towards impedance variations in the neighborhood of conjugate impedance matching, this is likely to be caused by a slight impedance mismatching.

The simulated values in Table I suggest that the improvement of the tag performance when it is placed on a metal sheet is explained by the improved directivity and impedance matching. The former is achieved, since the metal sheet reduces the back lobe of the tag antenna and boosts the directivity in the forward direction. The latter one is achieved by designing the impedance matching with the metal sheet included in the simulations. However, the radiation efficiency of the tag antenna is expectedly lower on metal than in the air, but in the presented design the efficiency drop is only 6%-points, from 95% to 89%, so that improvement in the overall performance is still achieved.

The measured and simulated maximum line of sight read range patterns at 915 MHz, both in the air and on metal, are presented in Fig. 4 in two orthogonal plane cuts. The peak value occurs in the forward direction with the measured values of 20.3 m and 25.4 m, in the air and on metal, respectively. Although the tag antenna pattern is directive, the measured 10 m read range is still achieved within a 65-degree beam. Moreover, in the *xy*-plane of Fig. 1, the measured read range in the directions of positive and negative *x*- and *y*-axes is more than 4 m. Thus, the tag has good coverage also away from the main beam direction and it remains is readable in the lateral directions of the metal surface.

The presented read ranges are sufficient for a number of identification applications requiring longer read range than is achievable with for example dipole-type tag antennas. These applications include identification of cargo containers, machinery, railroad cars and other vehicles. However, the results in this paper present the theoretical maximum read range and therefore the exact application specific read range has to be tested in the application environment.

In addition, the proposed antenna design is suitable for applications where tag antenna size is not the most critical parameter. In addition to the height of the antenna, its overall footprint affects the on-metal performance: decreasing footprint results in lower gain and shorter read range. Therefore, the presented patch-type tag antenna design can be proposed to applications where long and reliable read range is emphasized.

IV. Conclusions

A high performance platform tolerant metal mountable patch tag antenna for UHF RFID systems was developed. An inductive ground connection composed of thin conductor strips is used to achieve good conjugate impedance matching with a capacitive tag chip. The results from full wave electromagnetic simulations and measurements agree closely and the experimental results are within the uncertainty bounds based on the maximum expected tag chip and tag antenna impedance variations. The measured realized gain of the metal-mounted prototype tag antenna at 915 MHz is

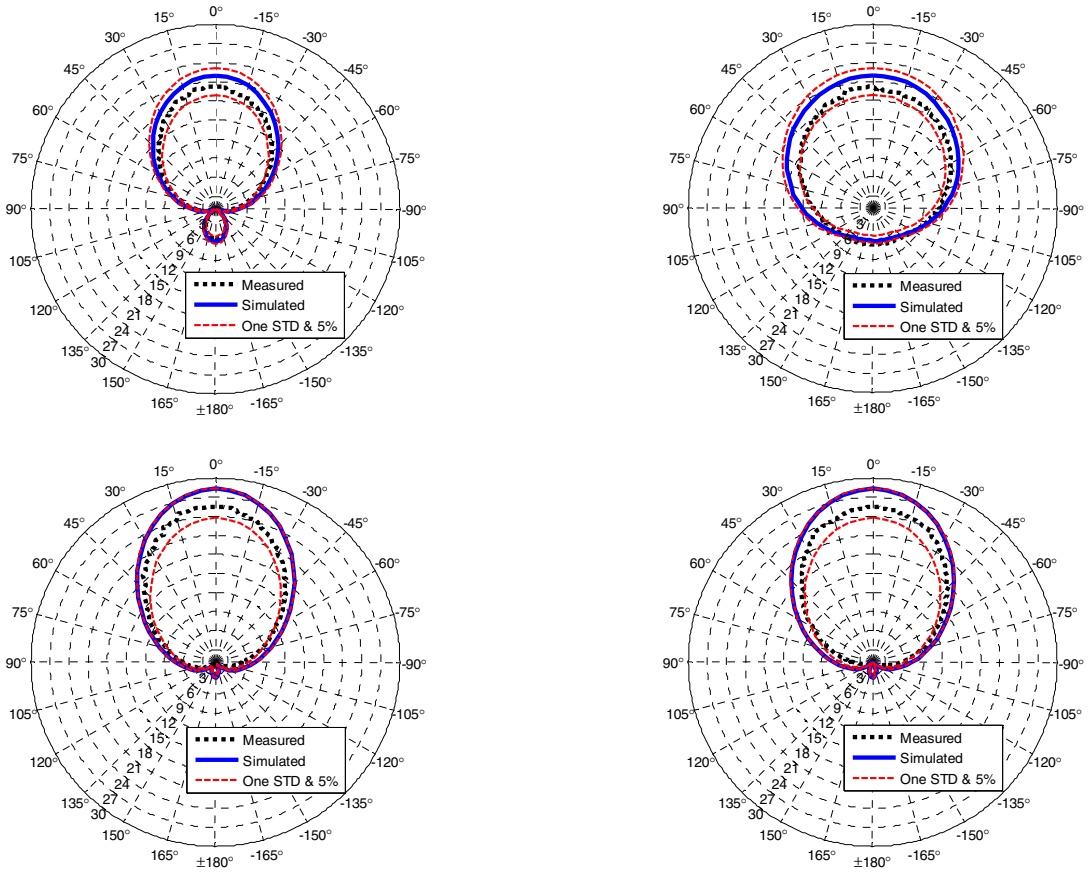

Fig. 4. Simulated and measured maximum line of sight read range patterns and the related uncertainty envelope in meters with the coordinate system of Fig. 1. Top left: *xz* plane in the air. Top right: *yz* plane in the air. Bottom left: *xz* plane on metal. Bottom right: *yz* plane on metal.

5.7 dBi with corresponding maximum theoretical line of sight read range of 25 meters.

REFERENCES

[1] R. S. Elliot, *Antenna Theory and Design*, Rev. Ed., An IEEE Classical Reissue, John Wiley & Sons, Inc., 2003.

[2] P. Raumonen, L. Sydänheimo, L. Ukkonen, M. Keskilammi, M. Kivikoski, "Folded dipole antenna near metal plate,"*Proc. of IEEE Antennas and Propagation Society International Symposium (APS)*, pp. 848- 851, June 22-27, 2003, Columbus, Ohio, USA.

[3] H.-D. Chen, Y.-H. Tsao, "Low-Profile Meandered Patch Antennas for RFID Tags Mountable on Metallic Objects," *IEEE Antennas Wireless Propag. Lett.*, vol. 9, pp. 118-121, 2010.

[4] W. Hong, N. Michishita, and Y. Yamada, "Low-Profile Normal-Mode Helical Antenna for Use in Proximity to Metal," *Journal of the Applied Computational Electromagnetics Society (ACES)*, vol. 25, no. 3, pp. 190-198, March 2010.

[5] T. Koskinen, H. Rajagopalan, and Y. Rahmat-Samii, "A Thin Multi-Slotted Dual Patch UHF-Band Metal-Mountable RFID Tag Antenna," *Microwave and Optical Technology Letters*, vol. 53, No. 1, pp. 40-47, January 2011.

[6] Y. M. Um, U. Kim, W. Seong, and J. Choi, "A Novel Antenna Design for UHF RFID Tag on Metallic Objects," *Proc. of Progress in Electromagnetic Research Symposium (PIERS)*, pp. 158-161, Aug. 27-30, 2007, Prague, Czech Republic.

[7] T. Björninen, M. Lauri, L. Ukkonen, L. Sydänheimo, A. Elsherbeni, and R. Ritala, "Wireless Measurement of UHF RFID Chip Impedance," *Proc. of the 32nd Annual Antenna Measurement Techniques Association (AMTA) Symposium*, pp. 35-40, Oct. 10-15, 2010, Atlanta, Georgia, USA.

[8] EPCglobal Frequency Regulations UHF: Online, last accessed February 15, 2011: http://www.epcglobalinc.org/tech/freq_reg/

Publication VII

T. Björninen, A. A. Babar. A. Z. Elsherbeni, L. Ukkonen, L. Sydänheimo, J. Kallioinen, “Compact metal mountable UHF RFID tag on a Barium Titanate based substrate,” *Prog. Electromagn. Res. C*, vol. 26, pp. 43-57, 2012.

Errata

The caption of Fig. 6 should read: ”Simulated tag antenna directivity [dBi] at 915 MHz in yz-plane (on the left) and xz-plane (on the right) in Fig. 4”.

Tampereen teknillinen yliopisto
PL 527
33101 Tampere

Tampere University of Technology
P.O.B. 527
FI-33101 Tampere, Finland

ISBN 978-952-15-2822-4
ISSN 1459-2045